EFFECTS OF ADHESION AND DEFORMATION ON STRETCHABLE ELECTRONIC STRUCTURES

OYEWOLE OLUWASEUN KEHINDE

(70074)

A THESIS PRESENTED TO FACULTY OF THE AFRICAN UNIVERSITY OF SCIENCE AND TECHNOLOGY, ABUJA, IN CANDIDACY FOR THE DEGREE OF DOCTOR OF PHILOSOPHY

RECOMMENDED FOR ACCEPTANCE BY THE DEPARTMENT OF THEORETICAL AND APPLIED PHYSICS

ADVISOR: PROFESSOR WOLE SOBOYEJO

2015

© Copyright 2015 by Oluwaseun Kehinde Oyewole.

All right reserved

ABSTRACT

This work presents the results of a combined experimental, computational and analytical study of the effects of adhesion and deformation on stretchable electronic structures. First, atomic force microscopy is used to measure adhesion in bi-material pairs that are relevant to organic, inorganic and hybrid organic/inorganic solar cells and light emitting devices. The measured adhesion forces are then incorporated into existing models to calculate the interfacial energies. The interfacial energies are then ranked in the electronic structures. Subsequently, the guidelines for lamination of low-cost organic electronic structures are developed. The effects of applied force on contacts between laminated layers are studied before estimating the crack driving forces associated with interfacial cracks along the bi-materials interfaces. The conditions for successful lamination of the organic electronic structures are then predicted using experiments and models. The failure mechanisms of inorganic stretchable electronic structures are studied. Wrinkled and buckled nano-scale gold films are formed on polymeric PDMS substrates before they are characterized using scanning electron microscopy. The interfacial crack growths between the films and substrates are studied using finite element simulations. The critical stresses needed for wrinkling and buckling are then analyzed using analytical models before explaining the potential implications of the results. Finally, the effects of stretching on deformation and failure mechanisms of stretchable organic solar cells are studied. Wrinkling and micro-buckling strategies are used to enhance the stretchability of thin films that are relevant to layers of organic solar cells. Wrinkling and buckling of the films are simulated by pre-stretching prior to deposition and release of the films. The subsequent effects of wrinkling and micro-buckling are then studied using a combination of computational models and simulations of the tensile

deformation of pre-wrinkled and pre-buckled organic solar cells. The predicted deformation characteristics are compared with the results of experiments presented in the literature. The predicted failure mechanisms are also compared with those obtained from experiments on stretchable substrates (with or without brittle indium tin oxide anodic layers). The observed failure mechanisms are used to explain the degradation of the optical transmittance and current-voltage (I-V) characteristics of stretchable organic solar cells.

LIST OF PUBLICATIONS

1. Textbook Chapters

- **O. K. Oyewole**, J. Asare and W. O. Soboyejo, "Effects on Adhesion and Stretching on Failure Mechanisms and Optical Properties of Organic Solar Cells" Advanced Materials for Energy, Biomedical and Multifunctional Structures, Trans Tech Publication (TTP) Ltd, Switzerland (2015); (In press).
- **O. K. Oyewole**, J. Asare and W. O. Soboyejo, "Failure Mechanisms in Layers Relevant to Organic Solar Cells" Advanced Materials for Energy, Biomedical and Multifunctional Structures , Trans Tech Publication (TTP), Switzerland (2015); (In press).

2. Peer-Review Journal Articles

a. Articles from the PhD Research Work:

i. D. Yu, **O. K. Oyewole**, D. Kwabi, T. Tong, V. C. Anye, J. Asare, E. Rwenyagila, A. Fashina, O. Akogwu, J. Du, and W. O. Soboyejo, "Adhesion in flexible organic and hybrid organic/inorganic light emitting device and solar cells" *Journal of Applied Physics* 116, 074506 (2014).

ii. **O. K. Oyewole**, D. Yu, J. Du, J. Asare, D. O. Oyewole, V. C. Anye, A. Fashina, M. G. Zebaze Kana and W. O. Soboyejo, "Micro-Wrinkling and Delamination-Induced Buckling of Stretchable Electronic Structures" *Journal of Applied Physics* 117, 235501 (2015).

iii. **O. K. Oyewole**, D. Yu , J. Du , J. Asare , V. C. Anye , A. Fashina , M. G. Zebaze Kana , W. O. Soboyejo, "Lamination of Organic Solar Cells and Organic Light Emitting Devices: Models and Experiments" *Journal of Applied Physics* (2015); (In press).

In Preparation:

iv. **O. K. Oyewole**, J. Du, J. Asare, D. O. Oyewole, B. Agyei-Tuffour, M. G. Zebaze Kana, O. Akin-Ojo and W. O. Soboyejo, "Deformation and Failure of Wrinkled and Micro-Buckled Stretchable Organic Solar Cells", prepared for *Journal of Applied Physics.*

b. Other Peer-Review Article Published:

i. T. M. Tong, J. Asare, E. R. Rwenyagila, V. Anye, O. K. Oyewole, A. A. Fashina and W. O. Soboyejo, "A study of Factors that Influence the Adoption of Solar Power Lanterns in a Rural Village in Kenya" *Journal of Perspectives on Global Development* 14, 448-491 (2015).

3. Peer-Review Conference Papers

i. **O. K. Oyewole**, D. O. Oyewole, J. Asare, B. Agyei-Tuffor, A. A. Oberafo, M. G. Zebaze Kana and W. O. Soboyejo, "Failure Mechanisms in Layers Relevant to Stretchable Organic Solar Cells" *Proceedings of Nigerian Materials Congress*, 53-59 (2014).

ii. J. Asare, M. G. Zebaze Kana, B. Agyei-Tuffor, **O. K. Oyewole** O. Oladipupo, K. O. Onogu, A. A. Oberafo and W. O. Soboyejo, "Optical Measurement and flexural Characteristics of bendable Organic photovoltaics" *Proceeding of Nigerian Materials Congress*, 65-69 (2014).

iii. **O. K. Oyewole**, Asare J., M.G. Zebaze Kana, A. A. Oberafo, W. O. Soboyejo: Effects of Stretching on Flexible Organic Electronic Structures, *Proceedings of the Materials Society of Nigeria Congress*, 509-512 (2011).

LIST OF CONFERENCE PRESENTATIONS

AUST PhD Colloquium, Abuja, Nigeria (2015)

"Effect of Adhesion and Deformation on Stretchable Electronic Structures"

Presentation, January, 2015

Materials Society of Nigeria Congress, Abuja, Nigeria (2013)

"Lamination of Layers of Organic Electronic Structures"

Presentation, November, 2013

African Materials Research Society (AMRS) Conference, Addis Ababa, Ethiopia (2013)

"Stretchable Organic Solar Cells: Effects of Adhesion and Cyclic Stretching"

Presentation, November, 2013.

Materials Society of Nigeria Congress, Ile-Ife, Nigeria (2012)

"Failure Mechanisms in Layers Relevant to Stretchable Organic Solar Cells"

Presentation, November, 2012

Materials Society of Nigeria Congress, Akure, Nigeria (2011)

"Effects of Stretching on Flexible Organic Electronic Structures"

Presentation, November, 2011

DEDICATION

This Thesis is dedicated to my family:

my parents, Late Mr. Samuel O. Oyewole and Mrs. Mary A. Oyewole,

and

my dearest wife, Deborah Olubunmi Oyewole.

ACKNOWLEDGEMENTS

All glory and adoration be unto God, the creator of the universe. My acknowledgement goes to God for He has shown His faithfulness to me throughout this journey of my PhD program at African University of Science and Technology (AUST), Abuja. He is the Alpha and the Omega, the beginning and the ending of my life. He is the God who has showered me with wisdom that beyond human imagination. Who am I not to appreciate Him for the unmerited blessings He has endowed me. His name shall be praised forever and ever.

It is obvious and now I can see that God has sent me a mentor. Professor Winston Oluwole Soboyejo is truly a supervisor, a mentor and a father. I have never seen a Professor like him since I have started university education. Your selfless attitude towards my success is beyond what I can explain. Please accept the appreciation that comes from the deepest of my heart. I will be indebted if I failed to appreciate your loving family, your wife, Mrs. Morenike Soboyejo and children: Timmy, Deji, Junior and Kanyinsola. You guys have been so wonderful.

I am indebted to Dr. M. G. Zebaze Kana of Kwara State University, Malete for his mentor and advice. I am also grateful to the entire staff of Advanced Physics Laboratory, Sheda Science and Technology Complex, Abuja, for giving me an opportunity to work with them in their laboratories. I am also grateful to Dr. Omololu Akin-ojo for his care, advice and guidance. I would also like to say a million thanks to Dr. Shola Odusanya of Advanced Biotechnology Laboratory, Sheda Science and Technology Complex, Abuja for his advice and guidance.

I cannot but say “a big thank you” to Dr. Jing Du of Department of Mechanical and Nuclear Engineering, The Pennsylvania State University for her technical contributions to my work. I am

also grateful to Ms. Deying Yu and Dr. Tiffany Tong for technical discussions. May God richly bless all of you.

My unending gratitude goes to my parents: Late Mr. Samuel Oluwole Oyewole and my sweet mother, Mrs. Mary Adedewe Oyewole, for their care, advice, and prayers. It would have been difficult without my siblings: Dele, Tope, Gbemi, Kemi, Taiwo-my twin sister, Idowu, and Alaba. You have all blessed me in care, support and prayers. May Almighty God be with all of you.

This journey wouldn't have been successful without the financial supports of African University of Science and Technology; Nelson Mandela Institute; African Development Bank; the World Bank STEP B-Program, and the African Capacity Building Foundation (ABCF) under the Support to Capacity Initiative of AUST in Science and Technology Project. You have all been wonderful in cash and kind.

I want to show my deep appreciation to those that we "journey" together for about 6 years now. I am indebted to AUST-Soboyejo energy research group: Joseph Asare, Fashina Adebayo, Vitalis Anye, Egidius Rwenyagila, Momodu Damilola and Benjamin Agyei-Tuffour. It would have been a bored journey without you guys. My profound gratitude goes to all the members of AUST-Soboyejo Bio research group: Ani Chukwuemeka, Stella Dozie-Nwachukwu, Danyuo Yiporo, Dr. Kwabena Kan-Dapaah and Dr. John David Obayemi. I am also grateful to AUST-Soboyejo Multifunctional research group: Bruno Dandogbessi, Arthur Emmanuel Kwesi, Ebenezer Anan, Azeko Tahiru, Shola Kolawole and Edward Ampaw. Thank you all for being part of the journey. You guys have made the journey shorter than I thought.

I will be ungrateful if I failed to appreciate those who have made AUST campus a beautiful place for me. I really appreciate all AUST staff and AUST professors. You guys have blessed me throughout of my stay. Almighty God will bless all of you in return.

Finally, my deepest, special and unique appreciation goes to my dearest wife, Deborah Olubunmi Oyewole. You are the best of all women, truly sent to me by God. Thank you for your patience and endurance throughout the period of my program.

I know that I am still missing some names. My sincere appreciation goes to those whose name I cannot remember now. Thank you all for being there for me.

O. K. Oyewole

Theoretical and Applied Physics

AUST

TABLE OF CONTENTS

ABSTRACT ..... **ii**

LIST OF PUBLICATIONS ..... **iv**

LIST OF CONFERENCE PRESENTATIONS ..... **vi**

DEDICATION ..... **viii**

ACKNOWLEDGEMENTS ..... **viii**

TABLE OF CONTENTS ..... **xi**

LIST OF TABLES ..... **xix**

LIST OF FIGURES ..... **xx**

CHAPTER 1 ..... **1**

BACKGROUND AND INTRODUCTION **1**

1.1 Introduction 1

1.2 Unresolved Issues 3

1.3 Scope of the Thesis 3

1.4 References 6

CHAPTER 2 ..... **9**

LITERATURE REVIEW **9**

2.1 Stretchable Inorganic Electronic Structures 9

2.2 Stretchable Organic Electronic Structures 10

2.3 Adhesion Theory 13

2.3.1 Adhesion Force Measurement 13

2.3.2 Adhesion Energy 15

2.3.3 Adhesion Models 16

2.3.3.1 Hertzian Model 16

2.3.3.2 Johnson-Kendall-Roberts (JKR) Model 20

2.3.3.3 Derjaguin-Muller-Toporov (DMT) Model 22

2.3.3.4 Maugis-Dugdale (MD) Model 23

2.4 Micro-buckling and Wrinkling of Thin Films 24

2.5 Review of Thin Film Fracture Mechanics 26

2.6 Lamination Mechanics 29

2.6.1 Interfacial Contact and Adhesion 31

2.7 References 35

CHAPTER 3 55

ADHESION IN STRETCHABLE/FLEXIBLE ORGANIC AND HYBRID ORGANIC/INORGANIC LIGHT EMITTING DEVICES AND SOLAR CELLS 55

3.1 Introduction 55

3.2 Theory 56

3.2.1 Atomic Force Microscopy (AFM) Force Measurement 56

3.2.2 Adhesion Energy 57

3.3 Experimental Procedures 57

3.3.1 Material Processing 57

3.3.1.1 Processing of the Flexible Organic and Hybrid Organic/Inorganic Light Emitting Devices 58

3.3.1.2 Processing of flexible organic and hybrid organic/inorganic solar cells 59
3.3.2 AFM Adhesion Experiments 60

3.4 Results and Discussion 62

3.4.1 Surface Characterization 62

3.4.1.1 Surface Morphologies and Roughness Measurements 62
3.4.2 Adhesion of Flexible Organic and Hybrid Organic/Inorganic Light Emitting Devices 63

3.4.2.1 Adhesion Forces 63
3.4.2.2 Adhesion Energies 64
3.4.3 Adhesion of Flexible Organic and Hybrid Organic/Inorganic Solar Cells 65

3.4.3.1 Adhesion Forces 65
3.4.3.2 Adhesion Energies 66
3.5 Summary and Concluding Remarks 67

3.6 References 71

CHAPTER 4 82

LAMINATION OF ORGANIC SOLAR CELLS AND ORGANIC LIGHT EMITTING DEVICES 82

4.1 Introduction 82

4.2 Modeling 83

4.2.1 Adhesive Surface Contacts 84

4.2.2 Fracture Mechanics Modeling 85

4.2.3 Computational Modeling 87

4.3 Experimental Methods 89

4.3.1 Pre-lamination of Layers of OPV Cells and OLEDs 89

4.3.2 Pull-off of the Laminated and Spin-coated Active Layers 91

4.4 Results and Discussion 92

4.4.1 Modeling of Contact during Pre-lamination 92

4.4.2 Pre-lamination of Active Layers 92

4.4.3 Pull-off Experiments 93

4.4.4 Interfacial Fracture During Lift-off 94

4.4.5 Implication 98

4.5 Conclusions 99

4.5 References 103

CHAPTER 5 117

MICRO-WRINKLING AND DELAMINATION-INDUCED BUCKLING OF STRETCHABLE ELECTRONIC STRUCTURES 117

5.1 Introduction 117

5.2 Theory 118

5.2.1 Residual and Applied Stresses 118

5.2.2 Wrinkling and Buckling Models for Stretchable Electronics 119

5.2.3 Interfacial Fracture Mechanics 120

5.2.3.1 Analytical Modeling 120

5.3 Materials and Methods 123

5.3.1 Experimental Methods 123

5.3.1.1 Formation of Wrinkled and Micro-Buckled Au on PDMS Substrates 123

5.3.1.2 Atomic Force Microscopy (AFM) Adhesion Measurements 123

5.3.2 Computational Methods 125

5.4. Results and Discussion 126

5.4.1 Wrinkling Profile as a Function of Pre-Strain and Substrate Elastic Modulus 126

5.4.2 Stress Analysis 127

5.4.2.1 Residual Stress 127

5.4.2.2 Critical Stresses 128

5.4.3 Surface Roughness/Profile 128

5.4.4 Interfacial Adhesion and Fracture Energies 129

5.4.4.1 Measured Adhesion Forces and Energies 129

5.4.4.2 Interfacial Fracture Energies 130

5.4.4.3 Comparison of Adhesion Energies and Energy Release Rates 131

5.4.4.4 Dependence of Interfacial Energy on Pre-Strain and Film Thickness 131

5.4.5 Implications 132

5.5. Summary and Concluding Remarks 133

5.6 References 137

CHAPTER 6 150

DEFORMATION AND FAILURE OF WRINKLED AND MICRO-BUCKLED STRETCHABLE ORGANIC SOLAR CELLS 150

6.1 Introduction 150

6.2 Theory 151

6.2.1 Wrinkling and Buckling Models for Stretchable Organic Solar Cells 151

6.2.2 Delamination-Induced Buckling and Cracking of Thin Films 152

6.3. Materials and Methods 154

6.3.1 Experimental Procedures 154

6.3.1.1 Processing of Stretchable Organic Solar Cells 154

6.3.1.2 Optical Transmittance Measurements 155

6.3.2 Computational Modeling 156

6.4 Results and Discussion 157

6.4.1 Effects of Stretching on Profiles of Layers 157

6.4.2 Failure Mechanics 158

6.4.3 Effects of Stretching on Optical Properties PEDOT:PSS Anodic Layer..... 159

6.4.4 Failure Mechanisms of Stretchable Organic Solar Cells 160

6.4.5 Implications..... 161

6.5 Summary and Concluding Remarks 163

6.6 References 166

CHAPTER 7 179

CONCLUSIONS AND SUGGESTIONS FOR FUTURE WORK 179

7.1 Conclusions 179

7.2 Suggestions for Future Work 181

7.2.1 Adhesion in Stretchable/Flexible Organic and Hybrid Organic/Inorganic Light Emitting Devices and Solar Cells 181

7.2.2 Micro-Wrinkling and Delamination-Induced Buckling of Stretchable Electronic Structures 182

7.2.3 Lamination of Organic Solar Cells and Organic Light Emitting Devices 182

7.2.4 Effects of Stretching on Failure Mechanisms of Stretchable Organic Solar Cells 182

APPENDIX 184

A Interfacial Energy Release Rate Due to Lamination of Thin Films 184

B Energy Release Rates Due to Delamination of Thin Films 187

LIST OF TABLES

Table 2.1: Summary of Hertz, JKR, DMT, and MD models 34

Table 3.1: Average rms roughness values for layers in the flexible light emitting device 69

Table 3.2: Average rms roughness values for layers in the flexible solar cells 70

Table 4.1: Properties of the materials used in the modeling 100

Table 4.2: Interfacial Adhesion and Fracture Energies in OLEDs and OPV Cells 101

Table 4.3: Summary of the guidelines for successful lamination of thin film structures of OLEDs and OPV cells 102

Table 5.1: Residual stresses due to effects of thermal expansion coefficient mismatch and pre-strained PDMS substrate. 134

Table 5.2: Average surface roughness values 135

Table 5.3: Interfacial energy release rates obtained from analytical expressions for different pre-strains for cracks between Au films and PDMS substrates 136

Table 6.1: Properties of the materials used in the modeling 165

LIST OF FIGURES

Figure 2.1: SEM images inorganic electronics of (a) gallium arsenide nanoribbons in buckled shapes where bonding to the PDMS substrate occurs only at the positions of the troughs and (b) SEM image of a silicon nanomembrane in a buckled, mesh layout on PDMS (Ref. 5)..... 44

Figure 2.2: Schematic of a typical structure of stretchable organic solar cell 45

Figure 2.3: Failure mode strategy for stretchable solar cells 46

Figure 2.4: Organic light emitting devices 47

Figure 2.5: AFM adhesion measurement configuration 48

Figure 2.6: Schematic force-displacement curve depicting the various stages [(A)-(E)] of cantilever-surface engagement (Ref. 32) 49

Figure 2.7: The Contact between two elastic surfaces, both in the presence (contact radius, a_1) and absence (Contact Radius, a_o) of the surface forces. (a) contact between AFM tip and substrate, (b) distribution of stress in contacting surfaces, and (c) force-displacement relation for contacting surfaces (Ref. 35) 50

Figure 2.8: Force (per unit area)-distance relation for Dugdale model (Ref. 40)..... 51

Figure 2.9: Optical images of stretching tests in the x- and y- directions. The labels for the legend give the strain magnitude in percent (Ref. 5)..... 52

Figure 2.10: (a) Light and (b) scanning electron microscope images of wrinkles with a checkerboard pattern (Ref. 44) 53

Figure 2.11: Schematic of macro/micro scale contact of a laminated thin film: (a) the thin-film coated stamp approaches substrate, (b) the thin film is in contact with the substrate but no force is applied to improve contact, (c) the micro scale of (b) with a an idealized dust particle (d) compressive force is applied to improve contact (e) the stamp is lifted off the laminated thin film. 54

Figure 3.1: Layered structures for flexible organic and hybrid light emitting device and solar cells (a) flexible organic light emitting device (b) flexible hybrid light emitting device (c) flexible organic solar cell (d and e) flexible hybrid organic/inorganic solar cell. 73

Figure 3.2: Schematic of interaction between material 1 and the tip of AFM (material 2)..... 74

Figure 3.3: SEM image of a typical AFM tip profile. 75

Figure 3.4: AFM surface morphologies for different layers in the flexible light emitting device: (a) PDMS (b) Cr (c) Baytron P VP AL-4083 PEDOT:PSS (d) MEH:PPV (e) Al. 76

Figure 3.5: AFM surface morphologies for different layers in the flexible solar cells: (a) PDMS on glass (b) Cr (c) PEDOT:PSS (d) P3HT:PCBM. 77

Figure 3.6: Interfacial adhesion forces in flexible organic and hybrid organic/inorganic light emitting devices. 78

Figure 3.7: Interfacial adhesion energies in flexible organic and hybrid organic/inorganic light emitting devices. 79

Figure 3.8: Interfacial adhesion forces in flexible organic and hybrid organic/inorganic solar cell. 80

Figure 3.9: Interfacial adhesion energies in flexible organic and hybrid organic/inorganic solar cell. 81

Figure 4.1: Schematics of micro scale models of interfacial fracture during the lift-off process of the lamination (a) model of the lift-off process after the press down of the layer on the substrate, (b) axisymmetric model of successful lift-off, (c) axisymmetric model of unsuccessful lift-off and (d) axisymmetric model of partial interfacial fracture. 106

Figure 4.2: Geometry and mesh of finite element model of surface contact during pre-lamination of active layers of organic solar cells and light emitting devices 107

Figure 4.3: FEM of surface contact model after applying a range of forces (0 N – 500 N)..... 108

Figure 4.4: Schematic of experimental pull-off of spin-coated and laminated layer, showing the (a) press down process and (b) pull-off process 109

Figure 4.5: Effects of force on contact profiles of (a) P3HT:PCBM on PEDOT:PSS-coated substrate and (b) MEH-PPV on PEDOT:PSS-coated substrate..... 110

Figure 4.6: Force-displacement curve of pre-lamination of (a) P3HT:PCBM and (b) MEH-PPV on PEDOT:PPS-coated glass. The peaks represent the interfacial adhesion force during lift-off of the stamp from P3HT:PCBM and MEH-PPV 111

Figure 4.7: Force-displacement curves of pull-off of: (a) spin-coated MEH-PPV (b) spin-coated P3HT:PCBM (c) laminated MEH-PPV and (d) laminated P3HT:PCBM..... 112

Figure 4.8: Samples of the AFM images of substrates after pull-off of active layers, MEH-PPV and P3HT:PCBM, for: (a and b) successful pull-off, (c and d) pull-off with remnants left on the substrates..... 113

Figure 4.9: (Color online) The normalized top/bottom energy release rate as a function of the normalized top/bottom crack length, respectively. The energy release rates of the edge cracks at the top interfaces (P3HT:PCBM/Stamp and MEH:PPV/Stamp) were calculated with no edge crack at bottom interfaces (P3HT:PCBM/PEDOT:PSS-coated glass and MEH:PPV/PEDOT:PSS-coated glass). The energy release rates of the edge cracks at the bottom interfaces were also calculated with no edge crack at the top interfaces..... 114

Figure 4.10: Interfacial fracture during lift-up of stamp from laminated of P3HT:PCBM and MEH:PPV on PEDOT:PSS-coated substrates for different particle diameters. (a)2 μm , (b) 6 μm, (c) 9 μm and (d) 12 μm. The concomitant energy release rates of the tips of the edge

cracks at the top and bottom interfaces as functions of bottom crack length. Here, the length of the top edge crack is $6\ \mu m$, while the thickness of the active layers is maintained at $200\ nm$. 115

Figure 4.11: The ratio of the interfacial energy release rates $(GtGb)$ as a function of the normalized bottom crack length $(dbtf)$ for: (a) lamination of P3HT:PCBM and (b) lamination of MEH:PPV, showing the influence of the particle size. Here, the thickness of the active layers is $200\ nm$. 116

Figure 5.1: Finite element model of buckling of thin gold film on PDMS substrate 140

Figure 5.2: Micro-wrinkle profiles for different pre-strain value of: (a) 18%, (b) 36%, and (c) 70%. 141

Figure 5.3: The wavelength of the profile versus pre-strain value of the PDMS substrate. 142

Figure 5.4: (Color online) Von Mises showing the dependence of elastic modulus of the substrate on wrinkle profile of Au film on PDMS substrate at 36 % pre-strain 143

Figure 5.5: Dependence of (a) profile wavelength on critical stress (b) substrate modulus on critical stress.144

Figure 5.6: SEM image of AFM tip profile. 145

Figure 5.7: Interfacial adhesion in Au-coated PDMS structure (a) schematic of Au-coated PDMS structure with Cr interlayer (b) average of the measured AFM adhesion forces (c) measured AFM adhesion energies. 146

Figure 5.8: Plot of G/G_c versus σ_R/σ_c 147

Figure 5.9: Interfacial energy release rate (G_{comp}) versus interfacial crack length. (a) 100 nm thick Au films on PDMS substrates; (b) 75 nm thick Au films on PDMS substrates; (c) 50 nesm thick films on PDMS substrates, and (d) 50 nm thick film with 36 % pre-strain and delamination ... 148

Figure 5.10: (Color online) Von Mises of delamination-induced buckled Au film. (a-e) the amplitude increases with increasing interfacial crack length. 149

Figure 5.11: Comparison of measured AFM adhesion energies and calculated interfacial energy release rates 150

Figure 5.12: (Color online) Interfacial energy release rate (G_{comp}) versus pre-strain 151

Figure 6.1: Schematics of buckling and wrinkling in stretchable organic solar cells 170

Figure 6.2: Schematic model of buckled thin films 171

Figure 6.3: Schematic of failure mechanisms in wrinkled thin films: (a) unstretched wrinkled film (b) nucleation of interfacial cracking of thin films when stretched beyond pre-strain level (c)

crack-induced delamination of the film from substrate when stretched far beyond pre-strain level. 172

Figure 6.4: SEM images of failures mechanisms in PEDOT:PSS/PDMS structure (a) unstretched (b) stretched up to 25 % strain (c) stretched up to 70 % strain 173

Figure 6.5: SEM images of failures mechanisms in P3HT:PCBM on PEDOT:PSS-coated PDMS (a) unstretched (b) stretched up to 25 % strain (c) stretched up to 70 % strain 174

Figure 6.6: SEM images of failures mechanisms in ITO/PDMS structure (a) unstretched (b) stretched up to 10 % strain (c) stretched up to 30 % strain 175

Figure 6.7: Amplitude of wrinkled films versus pre-strain for solar cell (a) without ITO layer (b) with ITO layer 176

Figure 6.8: Interfacial energy rate versus interfacial crack length along (a) PDMS and PEDOT:PSS interface (b) PDMS and ITO interface (c) PEDOT:PSS and P3HT:PCBM interface. The dash lines indicate the steady-state energy levels for calculating interfacial fracture energies. 177

Figure 6.9: Energy release rate versus applied strain for interface between (a) PDMS and PEDOT:PSS; (b) PDMS and ITO, and PEDOT:PSS and P3HT:PCBM. The dash lines are the critical compute interfacial fracture energies 178

Figure 6.10: Degradation of optical transmittance spectra of anodic PEDOT:PSS on PDMS substrate 179

Figure 6.11: Illustration of effects of failure mechanisms on typical I-V curves of a stretchable organic solar cell for different applied strain level. 180

CHAPTER 1

BACKGROUND AND INTRODUCTION

1.1 Introduction

In the recent years, there has been increasing interest in the use of stretchable electronics in several applications where stretchability is very important [1-8]. In most cases, stretchable electronics are either organic [1], inorganic [2-6] or hybrid organic-inorganic [7] structures that have found applications in electrical inter-connects [2, 4-6, 8], optical sensors [9,10], diffraction gratings [9,10], solar cells [1, 3], light emitting devices [7], surfaces for cell contact guidance [11,12] and biomedical devices [12]. There is also a vision of integrating stretchable electronics into multipurpose electronic systems that can serve as roofing tiles, energy harvesting systems and light of the future.

Stretchable inorganic electronics are made up of inorganic materials deposited (attached) onto stretchable substrates [2, 3, 6]. They include: stretchable inorganic light emitting devices; stretchable transistors, and stretchable inter-connects. The devices may be fabricated on rigid substrates before they are transferred to stretchable substrates. The devices are often bonded [4, 6] to the stretchable substrates, while the connectors between the devices are free to buckle [4, 6]. In some cases, the devices are deposited onto the substrates using physical and chemical

processes such as thermal evaporation, Chemical Vapour Deposition (CVD) and spin-coating techniques.

Stretchable organic electronics are organic materials that are fabricated on stretchable substrates. However, hybrid stretchable organic-inorganic electronics are produced from mixtures of both organic and inorganic materials on stretchable substrates. In most cases, organic and hybrid organic-inorganic electronics are solution-processed using spin-coating methods.

In the case of stretchable organic and hybrid organic-inorganic electronics, the metallic films may also be introduced by lamination techniques [13] that enable the direct transfer of soft or hard layers onto adhesive surface. The rigidity of the inorganic constituents can also be managed using pre-buckled thin film structures that are produced by pre-stretching of the substrates prior to deposition of metallic films [2-6, 8].

The stretching of electronic systems can result in wrinkling [6] and buckling [1] deformations. These result in out-of-plane structures that can accommodate strain. Hence, in a number of scenarios [1, 4-6], substrates are pre-strained prior to the deposition of the layered structures of flexible/stretchable devices. The amplitude of the resulting buckled and wrinkled structures depends on the pre-strain level [14]. It is, therefore, important to know the level of the applied pre-strain that can form wavy structures without failure of the deposited devices and at the layered interfaces.

The structures of stretchable electronics range from bi-layered inorganic metallic (silicon)-coated substrates, to multilayered organic and organic-inorganic structures that are coated on pre-strained substrates. In the case of bi-layered, stretchable, electronic structures, the interfacial

contact and adhesion between the two different materials may enhance the formation of wavy structures that can further enhance stretchability. Hence, the interfacial adhesion becomes significant in the case of multilayered, stretchable electronics. Furthermore, the layered electronic structures are susceptible to interfacial cracking during cyclic loading. There is therefore a need for detailed studies of interfacial adhesion and failure to provide the insights and models that are needed for the design and fabrication of stretchable/flexible electronic structures.

1.2 Unresolved Issues

Although the reliability of stretchable electronic structures depends strongly on interfacial adhesion and processing/fabrication techniques, there have been only a few studies of the effects of adhesion and processing on the reliability of stretchable electronic structures. There have also been only limited efforts to model the effects of pre-stretching on the stretchable electronic structures that can be formed from metallic thin film or hybrid organic-inorganic structures that are relevant to solar cells and hybrid organic-inorganic solar cells light emitting devices.

1.3 Scope of the Thesis

In this thesis, a combined analytical, computational and experimental method is used to study the effects of adhesion and stretching on failure mechanisms and electronic properties of structures that are relevant to stretchable electronics, organic, inorganic and hybrid organic-inorganic solar cells and light emitting devices. First, the role of adhesion is explored in the stretchable/flexible organic, inorganic and hybrid organic-inorganic solar cells and light emitting devices. This is done using experiments and existing models. The failure mechanisms in the stretchable metallic electronic structures are then studied using both experiments and

analytical/computational models. The measured adhesion energies are used for the prediction of limit stresses/strains associated with interfacial failure. Finite element models of the effects of pressure on the lamination of stretchable organic electronic structures are then presented before exploring the effects of stretching on the failure mechanisms and optoelectronic properties of stretchable organic solar cells.

Chapter 1 presents the background and introduction, as well as the objectives and scope of the thesis

Chapter 2 reviews prior work on stretchable electronics and the underlying literature on thin film and failure mechanics. These include: stretchable inorganic electronic structures; stretchable organic solar cells; adhesion theory; wrinkling of thin films; micro-buckling of thin films; fundamentals of fracture mechanics; thin film fracture mechanics and lamination mechanics.

Chapter 3 presents the results of an experimental study of the adhesion between bi-material pairs that are relevant to organic light emitting devices, hybrid organic/inorganic light emitting devices, organic bulk heterojunction solar cells and hybrid organic/inorganic solar cells on flexible substrates. The adhesion between the possible bi-material pairs is measured using force microscopy (AFM) techniques. The results of AFM measurements are incorporated into the models for the determination of adhesion energies. The results are then discussed for the design of robust organic and hybrid organic/inorganic electronic devices.

In Chapter 4, the lamination of organic solar cells and light emitting devices is presented. A combined experimental, computational and analytical approach is used to provide new insights into the lamination processes at the macro- and micro-scales. First, the effects of applied

lamination force (on contact between the laminated layers) are studied. The crack driving forces associated with the interfacial cracks (at the bi-material interfaces) are estimated along with the critical interfacial crack driving force associated with the separation of thin films after layer transfer. The conditions for lamination are predicted using a combination of experimental results and computational models. Guidelines are then developed for the lamination of low-cost stretchable electronic structures.

Chapter 5 explores the failure mechanisms in stretchable inorganic electronics. The evidence of wrinkles and micro-buckles on the surfaces of stretchable poly-dimethylsiloxane (PDMS) coated with nano-scale gold (Au) layer is studied. The wrinkles and micro-buckles are formed by the unloading of pre-strain PDMS substrate after evaporating nano-scale Au layers. Atomic force microscopy and scanning electron microscopy are then used to characterize the surface. The critical stresses required for wrinkle and buckle formation are analyzed using existing theories and finite element simulation. The energy release rates associated with the delamination of the buckles are elucidated using fracture mechanics concepts. The results are discussed for potential applications of wrinkles and micro-buckles in stretchable electronic structures and biomedical devices.

Chapter 6 examines the deformation and failure of wrinkled and micro-buckled stretchable organic solar cells. Wrinkling and micro-buckling strategies are used to enhance the stretchability of organic films. The failure mechanisms are observed using scanning electron microscopy before the interfacial fracture energies in the multilayered devices are computed using finite element simulations. The pre-strain limit for subsequent stretching (on wrinkled or micro-buckled surfaces) of stretchable organic solar cells is then predicted using the computed

interfacial fracture energies. The optical transmittance spectra of anodic layer of the devices are measured. The failure mechanisms are then used to explain the degradation of the optical transmittance and current-voltage (I-V) characteristics of stretchable organic solar cells.

Finally, salient conclusions arising from this work are summarized in Chapter 7. Suggestions for future work are also presented.

1.4 References

[1] D. J. Lipomi, B. C. Tee, M. Vosgueritchian and Z. Bao, "Stretchable Organic Solar Cells," *Adv. Mater.* 23, 1771-1775 (2011).

[2] T. Li, Z. Suo, S. P. Lacour and S. Wagner, "Compliant Thin Film Patterns of Stiff Materials as Platforms for Stretchable Electronics," *J. Meter. Res.* 20(12), 3274-3277 (2005).

[3] J. Lee, M. Shi, J. Yoon, S-I. Park, M. Li, Z. Liu and Y. Rogers, "Stretchable GaAs Photovoltaic with Design that Enable High Areal Coverage," *Adv. Mater.* 23, 986-991, (2011)

[4] D-H. Kim, and J. A. Rogers, "Stretchable Electronics: Materials Strategies and Devices," *Adv. Mater.* 20, 4887-4892 (2008).

[5] S. P. Lacour, J. Jones, Z, Suo and S. Wagner, "Design and Performance of Thin Metal Film Interconnects for Skin-Like Electronic Circuits," *IEEE Electron Device Lett.* 25, 179-181 (2004).

[6] D-H. Kim, J. Xiao, J. Song, Y. Huang and John A. Rogers, "Stretchable Curvilinear Electronics Based on Inorganic Materials," *Adv. Mater.* 22, 2108-2124 (2010).

[7] D. B. Mitzi, K. Chondroudis and C. R. Kagan, "Organic-inorganic Electronics," *Organic Electronics* 45 (1), 29-45 (2001).

[8] S. P. Lacour, J. Jones, S. Wagner, T. Li and Z. Suo, "Stretchable Interconnects for Elastic Electronic Surfaces," *Proc. IEEE* 93, 1459-1467 (2005).

[9] C. Yu, K. O'Brien, Y.-H. Zhang, H. Yu and H. Jiang, "Tunable Optical Grating Based on Buckled Nano-Scale Thin Films on Transparent Elastomeric Substrates," *Appl. Phys. Lett.* 96, 041111 (2010).

[10] N. Bowden, W. T. S. Huck, K. E. Paul and G. M. Whitesides, "The Controlled Formation of Ordered, Sinusoidal Structures by Plasma Oxidation of an Elastomeric Polymer," *Appl. Phys. Lett.* 75, 2557 (1999).

[11] M. T. Lam, W. C. Clem and S. Takayama, "Reversible on-demand cell alignment using reconfigurable microtopography," *Biomaterials* 29, 1705-1712 (2008).

[12] X. Jiang, S. Takayama, X. Qian, E. Ostuni, H. Wu, N. Bowden, P. LeDuc, D. E. Ingber, G. W. Whitesides, "Controlling mammalian cell spreading and cytoskeletal arrangement with conveniently fabricated continuous wavy featureson poly(dimethylsiloxane)," *Langmuir* 18, 3273-3280 (2002).

[13] W.O. Akande, Y. Cao, N. Yao and W. Soboyejo, "Adhesion and the cold-welding of gold-silver thin films," *J. Appl. Phys*. 107, 043519 (2010).

[14] Yi Wang, R. Yang, Z. Shi, L. Zhang, D. Shi, E. Wang and G. Zhang, "Super-Elastic Graphene Ripples for Flexible Strain Sensors," *ACNNano* 5(5), 3645-3550 (2011).

CHAPTER 2

LITERATURE REVIEW

2.1 Stretchable Inorganic Electronic Structures

Stretchable inorganic electronic structures are made up of inorganic materials deposited onto stretchable substrates. These are bi- or multi-layered structures that have emerged as interesting technologies for several applications in which stretchability is considered important [1-15]. These applications include: stretchable electrical inter-connects [1-5], optical sensors and diffraction gratings [6, 7], metrology for the measurement of elastic moduli [8, 9], templates for device fabrication [10], stretchable electronics [1, 3, 11, 12], micro-contact printing stamps [13, 14], cell culture substrates [15] and surfaces for cell contact guidance [16] in implantable biomedical devices .

Generally speaking, inorganic materials are intrinsically not stretchable upon deformation by stretching and, therefore, need to be made stretchable to accommodate strain. In this regards, different techniques have been used for fabrication. The electronic devices may be deposited onto a plane surface (like silicon wafer) before they are bonded to pre-stretched substrates [17,

18]. The bonded devices can then buckle to form stretchable devices, creating activated and inactivated regions (Figure 2.1). On the other hand, the device can be deposited directly onto the pre-stretched substrates, creating either wrinkle or buckle profile on the substrates after the substrates have been unloaded.

Rogers and co-workers [3, 4, 17, 18] have identified the importance of buckling as a strategy for achieving stretchable inorganic electronic devices, stretchable optoelectronic devices, stretchable integrated systems, stretchable metallic inter-connect and emerging stretchable curvilinear systems for biomedical applications.

2.2 Stretchable Organic Electronic Structures

In an effort to expand the scope of electronics, stretchable organic electronic structures become very important. Some surfaces and moving parts can be covered with stretchable electronics, which is impossible with conventional electronics [19]. The electronics go organic for easy fabrication, large surface area coverage and cost reduction. Generally speaking, organic electronic structures consist of organic materials that are sandwiched between two electrodes (an anode and a cathode). The types of the organic materials depend on the specific types of electronics.

In the case of organic solar cells, the sandwiched organic materials in the bulk heterojunction solar cells consist typically of active materials that are able to absorb light and photogenerate hole-electron pairs, which are separated and collected at the electrodes before recombination.

The major active material that has dominated organic solar cells for about a decade [20] is a blend of poly(3-hexylthiophene) (P3HT) as the electron donor and fullerene derivative (6,6)-phenyl C_{61}-butyric acid methyl ester) (PCMB) as the electron acceptor. This bulk heterojunction system, P3HT:PCMB, is one of the most successful electron donor/acceptor combinations in terms of efficiency and long term stability [21]. The organic solar cells become stretchable when they are deposited on stretchable substrates. The schematic of a typical structure of stretchable organic solar cell is shown in Figure 2.2.

The first organic solar cells were actually based on an active layer that is made of a single material sandwiched between two electrodes of different work functions [22]. The introduction of a double-layer structure of two organic semiconductor materials with different electron affinity by Tang (in 1986) is regarded as a breakthrough in the history of organic solar cells [23]. The second layer was a quantum leap (atomic electron transition) in terms of power conversion efficiency. These organic bilayer solar cells introduced by Tang [23] were made of conjugated small molecules, and achieved a low power conversion efficiency of about 1% [23]. The major limiting factor in this concept is that the thickness of the absorbing materials is much more than the diffusion length of the excitons (bound electron-hole pairs) [24]. In the real sense, for achieving high power conversion efficiency, the layer thickness of the absorbing materials has to be of the same order of the absorbing length [24].

The subsequent introduction of bulk heterojunction solar cells by Yu et al. [24] has tremendously improved the manufacturing of organic solar cells. The interface between donor and acceptor materials is spatially distributed as both components inter-penetrate one another. The concept of bulk heterojunction solar cells is implemented by spin coating a polymer

fullerene blend [25]. Presently, by using novel materials as well as additives optimizing the phase separation, solution processed bulk heterojunction solar cells can achieve a better power conversion efficiency [26].

The thin films of stretchable organic solar cells, which are intrinsically not stretchable, can be made stretchable by pre-stretching the substrate prior to deposition of the layers. Prior work of Bao and co-workers [12, 27] have reported results of stretchable organic solar cells that can be strained to 27 %. They deposited organic solar cells on pre-stretched substrates, which buckled up upon release to form structures (as shown in Figure 2.3) that can be stretched severally within the limit of the pre-strain. However, the failure due to delamination and buckling of the films can be very significant when the devices undergo several cyclic deformations, especially above the pre-strain.

In the case of stretchable organic light emitting devices, the active materials are capable of emitting light in response to electric current. The active materials are also sandwiched between two electrodes (Figure 2.4). They become stretchable when the layered structures are deposited on stretchable substrates. Yu et al. [28] have presented intrinsically stretchable polymer light emitting devices using carbon nanotube polymer composite electrodes. They showed metal-free devices that can be linearly stretched up to 45%. Sekitani et al. [29] have also presented the stretchable active-matrix organic light emitting diode display using printable elastic conductors. For flexibility of the anodic electrode, Song et al. [30] have provided an emerging anodic transparent conducting electrode for organic light emitting devices that can accommodate deformations.

2.3 Adhesion Theory

Adhesion between layered structures of electronic devices is crucial for good performance. A solid fundamental understanding of adhesion theories is helpful as a precursor to study the role of adhesion in bi- and multi-layered stretchable electronics. This will be presented here along with a review of the atomic force microscopy (AFM) technique that can be used to measure interfacial adhesion between two materials.

2.3.1 Adhesion Force Measurement

The adhesion force is of significant interest in layered stretchable electronics. Since the contacts between layers can affect the degradation and electronic performance of the devices, there is a need to measure the adhesion between layers that are relevant to stretchable inorganic, organic and hybrid electronic structures. The electronic structures are made up of bi- and multi-layers with a configuration of many interfaces. The interfacial adhesion of any interface can be measured by considering each of the two surfaces that constitute the interface. The contact mode of atomic force microscopy (AFM) is generally used to measure the adhesion force between the two surfaces.

To measure the adhesion force between two dissimilar materials, the tip of the AFM is coated with one of the material (Material 1) (Figure 2.5), while the substrate is coated with the other material (Material 2) (Figure 2.5). The tip is displaced towards the substrate until the tip jumps to

contact with the substrate when adhesive interactions are experienced. The tip is bent under elastic deformation as both surfaces remain in contact. The tip displacement is reversed but residual adhesion interactions still keep the tip in contact with the substrate even at zero loads until a negative force (pull-off force), which eventually overcome the adhesion, is experienced. This pull-off force quantifies the critical interfacial adhesion force between the two surfaces. The various steps for AFM adhesion force measurements have been explained in literature [31, 32]. These steps are illustrated schematically below in Figure 2.6.

According to Hooke's law, the applied force is directly proportional to the displacement, provided that the elastic limit is not exceeded. Hence, the adhesion force is related to the displacement as:

$$F_{adhesion} = -kx, \tag{2.1}$$

where k is the spring constant and x is the displacement. The negative sign accounts for the negative force experienced.

In contact mode, the accurate measurement of interfacial adhesion forces between the layers of the electronic devices depends on the spring constant of the AFM cantilever tip [31]. The spring constant can be calculated from the cantilever geometrical and material properties [32, 33]. The mathematical model for the most commonly used V-shaped cantilevers is the two-beam approximation, in which the cantilever is described by two rectangular beams in parallel. The expression for the spring constant, k, is given by [34].

$$k = \left(\frac{t}{L}\right)^3 \frac{Ew}{4}, \tag{2.2}$$

where w, t, L and E are the width, thickness, length and elastic property of the cantilever beams, respectively. However, the values for the spring constant are provided by most manufacturers of the AFM tip. The spring constant can also be calculated using thermal tune method [34].

We can thus estimate the adhesion force from equation (2.1) knowing fully well the value of the spring constant. The adhesion force is needful in determining the energy required to separate layers of the stretchable electronic structures like organic solar cells.

2.3.2 Adhesion Energy

Adhesion energy is the work required to build a unit interface between two dissimilar materials. The interface is built as a result of the interactions between the atoms on the surfaces of the two materials, which form secondary bonds. The adhesion energy can also be regarded as the energy required to adhesively break the interfacial secondary bonds between the two dissimilar materials. The true work of adhesion between the two materials is given by [32, 33, 35]:

$$G_{adhesion} \approx G_{elastic} = \gamma_1 + \gamma_2 - \gamma_{1-2} \tag{2.3}$$

where γ_1 and γ_2 are the surface energies of the materials 1 and 2 separately, while γ_{1-2} is the surface energy between the two materials in contact.

2.3.3 Adhesion Models

In an effort to calculate the interfacial adhesion energy between two dissimilar materials using the measured AFM adhesion force, several models have been developed [36-40] for different materials and geometry properties of the interacting layers. Among these are: the Hertzian model [36, 37]; the Johnson-Kendall-Roberts (JKR) model [38]; the Darjaguin-Muller-Toporov (DMT) model [39], and the Maugis-Dugdale (MD) models [40].

2.3.3.1 Hertzian Model

Hertz was the first to present contact mechanics, in which he studied the geometrical effects on local elastic deformation properties [36]. The Hertzian theory of elastic deformation relates the circular contact area of a sphere with a plane (or in more general cases, between two spheres) to the elastic deformation properties of the materials. It is assumed that when the separation between the surfaces is zero, the repulsion resembles a hard sphere model and adhesive forces are negligible. The model is illustrated below in Figure 2.7. When there is no surface force between the two surfaces, the contact radius, a_o, is related to the applied normal force, F_o, by the following Hertz equation [36]:

$$a_o^3 = \frac{RF_o}{K}, \tag{2.4}$$

where the effective radius, R and elastic constant, K of the two surfaces 1 and 2 is given respectively by:

$$R = \left(\frac{1}{R_1} + \frac{1}{R_2} \right)^{-1} \text{ and} \tag{2.5}$$

$$K = \frac{3}{4} \left(\frac{1-\nu_1^2}{E_1} + \frac{1-\nu_2^2}{E_2} \right)^{-1} \tag{2.6}$$

where R_1 is the radius of surface 1 (tip of the AFM) and R_2 is the root-mean squared roughness of the surface 2 (the substrate), E_1 and E_2 are the Young's moduli of material 1 and material 2, while ν_1 and ν_2 are Poisson's ratios of materials 1 and 2, respectively.

When there is attractive force between two surfaces, the radius, a_1 corresponds to an apparent Hertz force, F_1, in equilibrium even though the applied force is still maintained at F_o.

Hertz equation is thus:

$$a_1^3 = \frac{RF_1}{K} \tag{2.7}$$

The displacement (movement), δ, of the applied normal force, F_o is given by:

$$\delta = \frac{a^2}{R}. \tag{2.8}$$

Considering the force-displacement curve (Figure 2.7c), the elastic energy, U_E, of the system can be calculated using the following equation:

$$U_E = U_1 - U_2 \tag{2.9}$$

where U_1 is the energy required to give a contact radius, a_1, when normal force, F_1, is applied to the system taking surface forces to be zero and U_2 is the energy released in reducing the applied force to F_o , giving the final state (B) of the system. Using the fact that the infinitesimal work done is the product of the infinitesimal displacement and the applied force,

$$dU_1 = \delta dF \,. \tag{2.10}$$

Combining equations (2.7) and (2.8), gives:

$$\delta = \frac{F^{2/3}}{K^{2/3}R^{1/3}} \tag{2.11}$$

Equation (2.10) becomes:

$$U_1 = \int_0^{F_1} \frac{F^{2/3}}{K^{2/3}R^{1/3}} dF$$

$$U_1 = \frac{2}{3}\frac{F_1^{5/3}}{K^{2/3}R^{1/3}} \tag{2.12}$$

For U_2, we use the force-displacement relation which is given by [37]:

$$\delta_1 = \frac{2}{3}\frac{F}{Ka_1} \tag{2.13}$$

Similarly, $dU_2 = \delta_1 dF$, such that:

$$U_2 = \frac{2}{3Ka_1}\int_{F_o}^{F_1} FdF = \frac{F_1^2 - F_o^2}{3Ka_1}$$

$$U_2 = \frac{1}{3K^{2/3}R^{1/3}}\left[\frac{F_1^2 - F_o^2}{F_1^{2/3}}\right] \tag{2.14}$$

Substituting Equations (2.12) and (2.14) into (2.9) gives:

$$U_E = \frac{1}{K^{2/3}R^{1/3}}\left[\frac{F_1^{5/3}}{3} + \frac{F_o^2 F_1^{1/3}}{3}\right] \tag{2.15}$$

The mechanical energy, U_M due to the applied normal force, F_o is given by [37]:

$$U_M = -F_o\delta_2 \tag{2.16}$$

where $\delta_2 = \delta - \frac{2dF}{3Ka_1}$. Such that:

$$\delta_2 = \frac{F_1^{2/3}}{K^{2/3}R^{1/3}} - \frac{2}{3Ka_1}\int_{F_o}^{F_1} dF$$

$$\delta_2 = \frac{F_1^{2/3}}{K^{2/3}R^{1/3}} - \frac{2(F_1 - F_o)}{3Ka_1} \tag{2.17}$$

Substituting Equation (2.7) into (2.17) gives:

$$\delta_2 = \frac{1}{K^{2/3}R^{1/3}}\left[\frac{F_1^{2/3}}{3} + \frac{2F_oF_1^{-1/3}}{3}\right] \tag{2.18}$$

Finally, by substituting equation (2.18) into (2.16) gives the mechanical energy, U_M. This is given by:

$$U_M = -\frac{1}{K^{2/3}R^{1/3}}\left[\frac{F_0 F_1^{2/3}}{3} + \frac{2F_o^2 F_1^{-1/3}}{3}\right] \tag{2.19}$$

2.3.3.2 Johnson-Kendall-Roberts (JKR) Model

The first model to account for adhesion forces between surfaces is the Johnson-Kendall-Roberts (JKR) model [38]. The model assumes that adhesion forces deform the surface inside the region of contact and that no external attractive forces are present outside this region. It is applicable to tips (two materials in contact) with large radii and small stiffness. Such systems are called strongly adhesive systems. The model also accounts for the influence of van der Waals forces within the contact region.

Since the Johnson-Kendall-Roberts (JKR) model assumes that adhesive forces deform the surfaces, the surface energy, U_S, due to the adhesion force is given by [38]:

$$U_S = -\pi a_1^2 \gamma \tag{2.20}$$

Substituting the radius, a_1, in equation (2.7) into (2.20) gives:

$$U_S = -\pi\gamma\left(\frac{RF_1}{K}\right)^{2/3} = -\frac{\pi\gamma R^{2/3}F_1^{2/3}}{K^{2/3}} \tag{2.21}$$

where γ is the adhesion energy between the surfaces of materials 1 and 2.

Having calculated the stored elastic energy, the mechanical energy and the surface energy, the total energy, U_{total} , can be written as:

$$U_{total} = U_E + U_M + U_S \,. \tag{2.22}$$

Substituting equations (2.15), (2.19) and (2.21) into equation (2.22) gives:

$$U_{total} = \frac{1}{K^{2/3}R^{1/3}}\left[\frac{F_1^{5/3}}{3} + \frac{F_o^2 F_1^{-1/3}}{3}\right] - \frac{1}{K^{2/3}R^{1/3}}\left[\frac{F_o F_1^{2/3}}{3} + \frac{2F_o^2 F_1^{-1/3}}{3}\right] - \pi\gamma\frac{R^{2/3}F_1^{2/3}}{K^{2/3}} \,. \tag{2.23a}$$

We can also determine the derivative, $\frac{dU_{total}}{dF_1}$:

$$\frac{dU_{total}}{dF_1} = \frac{1}{K^{2/3}R^{1/3}}\left[\frac{5F_1^{2/3}}{9} - \frac{2F_o^2 F_1^{-4/3}}{9}\right] - \frac{1}{K^{2/3}R^{1/3}}\left[\frac{2F_o F_1^{-1/3}}{9} - \frac{2F_o^2 F_1^{-4/3}}{9}\right] - \frac{2\pi\gamma R^{2/3}F_1^{-1/3}}{3K^{2/3}}$$

$$\frac{dU_{total}}{dF_1} = \frac{1}{K^{2/3}R^{1/3}}\left[\frac{5F_1^{2/3}}{9} - \frac{2F_o^2 F_1^{-4/3}}{9} - \frac{2F_o F_1^{-1/3}}{9} + \frac{2F_o^2 F_1^{-4/3}}{9}\right] - \frac{2\pi\gamma R^{2/3}F_1^{-1/3}}{3K^{2/3}}$$

$$\frac{dU_{total}}{dF_1} = \frac{1}{K^{2/3}R^{1/3}}\left[\frac{5F_1^{2/3}}{9} - \frac{2F_o F_1^{-1/3}}{9}\right] - \frac{2\pi\gamma R^{2/3}F_1^{-1/3}}{3K^{2/3}} \tag{2.23b}$$

At equilibrium, $\frac{dU_{total}}{dF_1} = 0$. Therefore, Equation (2.23b) becomes:

$$\frac{1}{K^{2/3}R^{1/3}}\left[\frac{5F_1^{2/3}}{9} - \frac{2F_o F_1^{-1/3}}{9}\right] - \frac{2\pi\gamma R^{2/3}F_1^{-1/3}}{3K^{2/3}} = 0$$

$$5F_1 - 2F_o - 6\pi\gamma R = 0 \tag{2.24}$$

JKR predicts that, at $a_1 = 0$ $(F_1 = 0)$, using the fact that equation 2.24 holds, the composite force, F_o , is given by:

$$F_o = -3\pi\gamma_{JKR}R$$

The pull-off force (adhesion force) needed for separation of the AFM tip and the substrate is given by:

$$F_{adhesion} = \frac{F_o}{2} = -\frac{3\pi\gamma_{JKR}R}{2}$$

Hence,

$$\gamma_{JKR} = -\frac{2F_{adhesion}}{3\pi R} \tag{2.25}$$

2.3.3.3 Derjaguin-Muller-Toporov (DMT) Model

Derjaguin-Muller-Toporov (DMT) presented another theory that considered the adhesive forces to have the nature of van der Waals forces [39]. This model is used to examine the weak interactions between stiff materials with small radii. DMT considered the contact radius, a, as a function of applied force as follows.

$$a = \left[\frac{R}{K}\left(F_o + 4\pi\gamma_{DMT}R\right)\right]^{1/3} \tag{2.26}$$

where γ_{DMT} is the adhesion energy of the DMT model.

Similarly, the composite force, $F_o = 2F_{adhesion}$, at $a = 0$. Hence, the adhesion energy for DMT model can be related to adhesion force as:

$$\gamma_{DMT} = -\frac{F_{adhesion}}{2\pi R} \tag{2.27}$$

2.3.3.4 Maugis-Dugdale (MD) Model

Maugis-Dugdale (MD) model examined the theory of contact on the basis of fracture mechanics [40] and was able to give the analytical solution that matched the JKR or DMT solutions. The model is an intermediate between JKR and DMT models. Maugis considered a 'Dugdale' (square-well) potential to describe adhesive forces between two contacting surfaces. Figure 2.8 below is force per unit area-distance relation for Dugdale model. He determined a dimensionless parameter, λ, which is given by [36, 40]:

$$\lambda = 2\sigma_o \left(\frac{R}{\pi K^2 \gamma} \right)^{1/3} = -0.913 \ln\left(1 - 1.018\alpha\right) \tag{2.28}$$

In this model, the adhesion energy, $\gamma = \sigma_o \delta_t$

where σ_o is a constant (maximum) adhesion stress (force per area), δ_t is the separation height (range), α is the transition parameter. The adhesion energy can also be written as [40]:

$$\gamma = \frac{F_{adhesion}}{\pi R f_{adhesion}} \tag{2.29}$$

Where $f_{adhesion} = 0.267\alpha^2 - 0.757\alpha + 2$ (2.30)

The dimensionless parameter, λ , can be used to characterize the entire range of adhesion models. According to Carpick et al. [41], if $\lambda > 5$, the JKR model applies and if $\lambda < 0.1$, the DMT model is applies. The interval $0.1 < \lambda \leq 5$ corresponds to MD model, which is a regime between JKR and DMT models. The Hertz, JKR, DMT, and MD models are summarized below in table 2.1.

2.4 Micro-buckling and Wrinkling of Thin Films

Mechanical flexibility is a prerequisite to achieve organic [12] and inorganic [2-5, 17] stretchable electronics, where wrinkling and buckling deformations are used to create wavy, out of plane structures that can accommodate strain. This is done by pre-stretching the substrates [3, 4, 9] before the deposition of the devices. The wrinkled and buckled structures of the devices are formed due to thermal compressive residual [11, 39, 43, 44] and pre-stretch [3, 5, 9] stresses. The formation and deformation of wrinkling of thin films can initiate failure, which can lead to delamination [45] in layered structures of the thin films.

Prior work by Rogers and co-workers [3, 4, 17] has identified the importance of buckling as a strategy for achieving stretchable thin films for stretchable electronics, stretchable optoelectronic devices, stretchable integrated systems, stretchable metallic inter-connect (Figure 2.9) and emerging stretchable curvilinear systems for biomedical applications. The formation of wrinkles

of thin film-coated polymeric structures has also been observed by Watanabe [44] for checkerboard patterning (Figure 2.10).

In the case of wrinkling, the films adhere to substrate, upon release of pre-strain. During service conditions, by stretching the wrinkled film below the critical pre-strain levels, the wavy structures will become plane, while the interfacial contact remains intact. However, the nucleation and growth of cracks along the interface can cause interfacial failure to occur under static or cyclic loading conditions above threshold conditions. This can lead ultimately to adhesive or cohesive failure. Mei et al. [43] and Ebata et al. [45] have shown that the wrinkled surfaces are formed due to compression-induced buckling instability of thin films, which can lead to interfacial cohesive failure and delamination.

On the other hand, a buckled morphology of the layered film can occur in the presence of interfacial voids, before and after the release of the pre-stretch. This failure mode can also occur due to merging of the possible micro voids that can lead to delamination [43, 45]. Interfacial cracks can also form from sandwiched dust particles [46] and bubbles [47] between the deposited films and substrates. Residual stress can also drive the delamination of the layered structures from substrate. The interfacial cracks then grow under static or cyclic loading conditions until critical conditions are reached. It is, therefore, important to study the possible interfacial adhesion and contact of micro-wrinkled and buckled structures.

The delamination-induced buckling of thin films (on the surfaces of elastomers) can be precisely controlled [18] with periodic, inactivated and activated regions. Ordered buckled structures can also occur on thin metal films, due to the thermal contraction of elastomeric

polymer substrates [18]. Furthermore, the controlled formation of ordered, sinusoidal wrinkles has also been associated with the effects of plasma oxidation of a compliant polymer [48]. Periodic sinusoidal structures have also been developed for buckled ribbons of piezoelectric ceramic (PZT) [49] and tunable diffraction gratings [10].

Hobbie et al. [50] have also reported that the dominant wavelength of the wrinkled structures of single-wall carbon nanotube films deposited on pre-strain poly(dimethylsiloxane) (PDMS) decreases with pre-strain, while Wang et al. [51] have shown that the amplitude and periodicity of buckled graphene films on flexible substrates reduces with the increasing pre-strain.

2.5 Review of Thin Film Fracture Mechanics

Fracture occurs in layered materials when the stress that is applied is greater than the critical stress. In layered thin films on stretchable substrates, residual stress can cause crack to grow in the film and along the interface between the films and the substrates. Crack can also grow in the substrate if the substrate is not compliant enough. The separation between the films and the substrate can be cohesive or adhesive. In the case of interfacial crack growth between the films and substrates, fracture can be referred to as breaking of bonds that cause interfacial adhesion between the two layers.

In the case of stretchable thin films, the stress on the films is due to thermal mismatch between the film and the substrate. When the film is deposited onto pre-stretched substrate, the film is deposited at a temperature that is different from the substrate, making the stress on the

film is two components: the residual stress due temperature mismatch and mechanical stress due to the pre-stretched substrate [33]. Hence, stretchable thin films are generally wrinkled or buckled. The buckling can also induced delamination of the films on elastomeric substrates.

In an effort to further understand the mechanics of thin films on elastomeric substrates, Hutchinson and Suo [52] have shown that when compressive stresses in the films exceed the critical buckling stress, the film can buckle away from the substrate, for a given interfacial crack length. Angstrom-scale periodic buckling patterns have been observed in free-standing graphene bi-layered thin films generated by liquid-phase processing, [53] while non-sinusoidal surface profiles of buckled gold thin films have been observed on elastomeric substrates [54]. Furthermore, finite width effects have been elucidated using experiments and models [55], while the deformation of a stretchable single crystal silicon has been studied on elastomeric substrates [56].

Theoretical and numerical schemes have been used by Domokos et al. [57] to study the elastic buckling of an inextensible beam with fixed end displacements, restricted to the plane, and in the presence of rigid, frictionless side-walls. Holmes [58] has also studied the buckling of an inextensible rod, restricted to the plane, with free ends, and in the presence of distributed body forces derived from a potential. The effects of plasticity on buckling patterns in thin films on elastomeric substrates have also been studied using finite element simulation to reveal different patterns of buckling [59].

In an effort to develop layered thin films in stretchable electronics, the level of strain-to-wrinkling had been modeled in literature. A well-known analytical solution [18, 60] has been

used to predict critical strain for the onset of wrinkling of thin films on pre-strained polymeric substrates with small and large pre-strains [5, 18, 39, 44, 60]. Jiang et al. [60] have obtained the analytical solution for the bucking geometry and maximum strain in buckled thin film using nonlinear buckling model. Sun et al. [18] have also analyzed the incompressible substrate deformation of a folding wrinkled structures using neo-Hookean non-linear elasticity, while Huang [61] has presented nonlinear analyses of wrinkle formation in films bonded to compliant substrates. The wrinkling was due to compressive stresses [62], which buckled the films on the polymeric substrates after deposition.

Significant efforts have been reported on nanotubes thin films on stretchable substrates. Harris et al. [63] have reported the electronic and optical properties of thin films of single-walled carbon nanotubes on polymeric substrates. They had studied the underlying failure mechanisms, for significant differences in the electronic manifestations of the thin films using wrinkling.

In the case of self-assembled materials, Ramanathan et al. [64] have described the role of confinements on wrinkling structures using compressive strains. Wang et al. [65] have presented the experimental investigation of fracture in the self-assembled gold nanoparticle layers on polymeric substrates. They showed that the fracture strength of the gold nanoparticles increases as the size of the particles increases, but decreases as the layer thickness increases. Fei et al. [54] have analyzed the profile of gold-PDMS structure using experiments and finite element models. They showed that the profile of the structure depends on film thickness, the level of pre-strain and the rate at which the strain is being released. Therefore, the different profiles of thin-film coated PDMS substrates can be attributed to the effects of strain localization, when the pre-strain

exceeds the critical strain. Ebata et al. [45] have also shown that the amplitude of the wrinkled, folded and delaminated profile of such structures depends on the applied strain.

2.6 Lamination Mechanics

In an effort to achieve electronics at low cost, several deposition techniques have been used for the fabrication of organic solar cells and organic light emitting devices [66-70]. These include: cold welding [46]; transfer printing [71] and lamination [66-69] techniques. In the case of lamination, deposition parameters, such as applied force for pre-lamination, pull-off force and surface roughness must be controlled for successful lamination [71, 72]. In most cases, the presence of particles in clean room environment (e.g. silicon, dust and organic materials) cannot be ignored. Such particles are trapped at the interfaces between layers during the fabrication of organic light emitting devices (OLEDs) and organic solar cells (OPVs) [72]. This results in the fabrication of microvoids and partial contacts at the interfaces of layered electronics [71-73].

Furthermore, during lift-off (separation of stamp from the transferred layer) in the process of lamination, stress concentrations occur at the edges of the entrapped voids/cracks. Since these can lead to interfacial plasticity or cracking, it is important to understand the stresses and crack driving forces associated with contacts and pull-off stages of pre-lamination and pull-off forces. It is also important to identify the processing windows for contact and pull-off without indicating damage to organic electronic devices.

Since OPVs and OLEDs require charge transport across interfaces in layered, the process of charge transport across interfaces can be hindered by entrapped voids/cracks that are formed during contact and lamination processes [72]. Conversely, the contact between adjacent layers can be enhanced by increased pressure and interfacial adhesion. This can improve charge transport across layer structures that are relevant to organic solar cells and light emitting devices. However, excessive pressure can also lead to sink-in of the interfacial impurities and damage to the devices [74]. There is, therefore, a need for models that can guide the design of impurities.

Prior works [66, 68, 75] has been carried out on the lamination of solar cells, light emitting devices and flexible batteries. Lee et al. [66] have demonstrated the lamination of top electrode in semitransparent organic photovoltaic cells. They showed that the top electrode can be laminated for enhanced electrode performance without necessarily inducing damage in the underlying device. Guo et al. [68] have also shown that high performance Polymer Light Emitting Diodes (PLEDs) can be fabricated by a low temperature lamination process. The interfacial properties of the laminated layered devices were enhanced using template activated surface (TAS). Huang et al. [67] have also described a one-step process for the fabrication of semitransparent polymer solar cells. These were fabricated using a glue-based lamination process that was combined with interfacial modification. Furthermore, Wu et al. [75] have used a lamination process to integrate Li-ion battery materials onto a single sheet of paper. Hence, lamination technique can be improved for fabricating high performing low-cost electronics.

In an effort to improve the interfacial adhesion and contacts in laminated bi- and multi-layered structures for organic and inorganic electronic applications, Cao et al. [72] and Akande et al. [46] have reported a cold welding technique for gold-gold and gold-silver thin films. Their

study showed that improved interfacial adhesion (of gold-silver films) can be engineered in the presence of dust particles along the cold-welded interface. A computational approach has also been used by Tucker et al. [71] to improve the quality of film transferred during the lamination of electronic devices.

2.6.1 Interfacial Contact and Adhesion

There are three major steps in lamination of thin films: bringing the films to contact with substrate (Figures 2.11a, 2.11b and 2.11c), applying pressure/force to ensure contact between the thin film and the substrate (Figure 2.11d) and lifting off of the stamp from the laminated thin film (Figure 2.11e). It is very important to understand the interfacial surface contact of laminated thin films on substrates, especially when the film is deposited onto a substrate with idealized dust particles. The thin film bends around the dust particle as the compressive force is applied to improve contact.

The thin film can be considered as a cantilever beam with a bending energy, U_b. This is given by [76]:

$$U_b = \frac{6E_f I h^2}{S^3} \tag{2.31}$$

where E_f is the film Young's modulus, I is the second moment of inertial, h is the height of the particle and S is the length of the void created by the particle.

For a rectangular geometry, the contact surface area is given by:

$$A_c = L_c \times w \tag{2.32}$$

where L_c is the contact length and w is the width of the film. The uniform pressure, P, which is applied to a cross-section area, $A_f = L \times w$, of the film can be related to the corresponding compressive force, F. This is given by:

$$P = \frac{F}{Lw} \tag{2.33}$$

where L is the length of the structure.

Hence, the surface energy between the film and the substrate can be written as the product of the pressure, the contact area and the height of the particle. This is given by:

$$U_s = -\frac{F}{Lw} \times (L_c \times w) \times h = -\frac{FL_c h}{L} \tag{2.34}$$

By substituting $L_c = L - S$ into Equation (2.34), the surface energy becomes:

$$U_s = -Fh\left(1 - \frac{S}{L}\right) \tag{2.35}$$

The total energy, U_T, is the addition of Equations (2.31 and 2.35). This is given by:

$$U_T = \frac{6E_f I h^2}{S^3} - Fh\left(1 - \frac{S}{L}\right) \tag{2.36}$$

The length of the void can be calculated from Equation (2.36) at equilibrium, $dU_T/dS = 0$. This is given by:

$$S = \left(\frac{18 E_f I h L}{F} \right)^{\frac{1}{4}} \tag{2.37}$$

By substituting the second moment of inertial, $I = w t_f^3 / 12$, into Equation (2.37), the length of the void becomes:

$$S = L - L_c = \left(\frac{3 E_f t_f^3 h L w}{2F} \right)^{\frac{1}{4}} \tag{2.38}$$

From Equation (2.38), we write the contact length as a function of the compressive force. This given by:

$$\frac{L_c}{L} = 1 - \left(\frac{3 E_f t_f^3 h w}{2 F L^3} \right)^{\frac{1}{4}} \tag{2.39}$$

Table 2.1: Summary of Hertz, JKR, DMT, and MD models

Model	**Assumptions**	**Restrictions**
Hertz	No surface forces	It is not applied to small loads in the presence of surface forces
JKR	The surface forces act within the contact region	It is applied only to large value of dimensionless parameter, λ of about 5.0
DMT	The surface forces act only outside the contact region	The dimensionless parameter, λ =0.1
MD	The tip-sample interface is modeled as a ring	It is applied to all values of λ between 0.1 and 5

2.7 References

[1] S. P. Lacour, J. Jones, S. Wagner, T. Li and Z. Suo, "Electronic skin: architecture and component," *Proc. IEEE* 93, 1459-1467 (2005).

[2] T. Li, Z. G. Suo, S. P. Lacour and S. Wagner, " Compliant thin film patterns of stiff materials as platforms for stretchable electronics," *J. Mater. Res.* 20, 3274-3277 (2005).

[3] D-H. Kim, and J. A. Rogers, "Stretchable electronics: Materials strategies and devices," *Adv. Mater*. 20, 4887-4892 (2008).

[4] S. P. Lacour, J. Jones, Z. Suo and S. Wagner, "Design and performance of thin metal film interconnects for skin-like electronic circuits," *IEEE Electron Device Lett.* 25, 179-181 (2004).

[5] D-H. Kim, J. Xiao, J. Song, Y. Huang and J. A. Rogers, "Stretchable, Curvilinear Electronics Based on Inorganic Materials," *Adv. Mater.* 22, 2108-2124 (2010).

[6] C. Yu, K. O'Brien, Y-H. Zhang, H. Yu and H. Jiang, "Tunable optical gratings based on buckled nanoscale thin films on transparent elastomeric substrates," *Appl. Phys. Lett*. 96, 041111 (2010).

[7] N. Bowden, W. T. S. Huck, K. E. Paul and G. M. Whitesides, **"**The Controlled formation of ordered, sinusoidal structures by plasma oxidation of an elastomeric polymer," *Appl. Phys. Lett.* 75, 2557-2559 (1999).

[8] C. M. Stafford, C. Harrison, K. L. Beers, A. Karim, E. J. Amis, M. R. VanLandingham, H.-C. Kim, W. Volksen, R. D. Miller, E. E. Simonyi, "A buckling-based metrology for measuring the elastic moduli of polymeric thin films," *Nat. Mater*. **3**, 545-550 (2004).

[9] C. M. Stafford, B. D. Vogt, C. Harrison, D. Julthongpiput and R. Huang, "Elastic moduli of ultrathin amorphous polymer films," *Macromolecules*, 39, 5095-5099 (2006).

[10] P. J. Yoo, K. Y. Suh, S. Y. Park and H. H. Lee, "Physical self- assembly of microstructures by anisotropic buckling," *Adv. Mater.* 14, 1383-1387 (2002).

[11] M. Watanabe, H. Shirai and T. Hirai, "Wrinkled polypyrrole electrode for electroactive polymer actuators," *J. Appl. Phys.* 92, 4631-4637 (2002).

[12] D. J. Lipomi, B. C. Tee, M. Vosgueritchian and Z. Bao, "Stretchable Organic Solar Cells," *Adv. Mater*. 23, 1771-1775 (2011).

[13] M. Pretzl, A. Schweikart, C. Hanske, A. Chiche, U. Zettl, A. Horn, A. Boker and A. Fery, "A lithography-free pathway for chemical microstructuring of macromolecules from aqueous solution based on wrinkling," *Langmuir* 24, 12748-12753 (2008).

[14] F. Wang, M. Xue and T. Cao, "Thermochemical patterning of polymer thin films with tunable size-reduction effects using metal-coated poly(dimethylsiloxane) stamps," *Adv. Mater*. 21, 2211-2215 (2009).

[15] M. T. Lam, W. C. Clem and S. Takayama, " Reversible on-demand cell alignment using reconfigurable microtopography," *Biomaterials* 29, 1705-1712 (2008).

[16] X. Jiang, S. Takayama, X. Qian, E. Ostuni, H. Wu, N. Bowden, P. LeDuc, D. E. Ingber, and G. M. Whitesides, "Controlling mammalian cell spreading and cytoskeletal arrangement with conveniently fabricated continuous wavy features on Poly(dimethylsiloxane)," *Langmuir* 18, 3273-3280 (2002).

[17] J. Lee, M. Shi, J. Yoon, S-I. Park, M. Li, Z. Liu and Y. Rogers, "Stretchable GaAs Photovoltaics with Designs that Enable High Areal Coverage," *Adv. Mater*. 23, 986-991 (2011).

[18] Y. Sun, W. M. Choi, H. Jiang, Y. Y. Huang and J. A. Rogers, "Controlled buckling of semiconductor nanoribbons for stretchable electronics," *Nature Nanotechnology 1*, 201-207 (2006).

[19] T. Sekitani and T. Someya, "stretchable, large-area organic electronics," *Adv. mater*. 22(20), 2228-2246 (2010).

[20] G. Dennler, M. C. Scharber, and C. J. Brabec "Polymer-Fullerene Bulk, Heterojunction Solar Cells," *Adv. Mater*. 21, 1323-1338 (2009).

[21] N. S. Sariciftci, L. Smilowitz, A. J. Heeger and F. Wudl, "Photoinduced electron transfer from a conducting polymer to buckminsterfullerene," *Science* 258 (5087), 1474-1476. (1992).

[22] V. I. Arkhipov and H. Bässler, "Exciton dissociation and charge photogeneration in pristine and doped conjugated polymers," *Phys. Status Solidi A*. 201, 1152-1187 (2004).

[23] K. Uduma and T. Arciszewski, "Sustainable Energy Development," *Sustainable* 2, 1558-1570 (2010).

[24] J. M. Nunzi, "Organic photovoltaic materials and devices," *C. R. Physique*. 3, 523-542 (2002).

[25] Y. G. Gao, J. Hummelen, J. C. Wudl, F. Heeger, "J. Polymer Photovoltaic Cells: Enhanced Efficiencies via a Network of Internal Donor-Acceptor Heterojunctions," *Science*, 270, 1789-1791 (1995).

[26] H. Qin, L. Li, F. Guo, S. Su, J. Peng, Y. Guo and X. Peng, "Solution-processed bulk heterojunction solar cells based on aporphyrin small molecule with 7% power conversion efficiency," *Energy Environ. Sci.* 7, 1397-1401 (2014).

[27] D. J. Lipomi, J. A. Lee, M. Vosgueritchian, B. C.-K. Tee, J. A. Bolander, and Z. Bao, "Electronic properties of transparent conductive films of PEDOT: PSS on stretchable substrates," *Chem. Mater*. 24, 373-382 (2012).

[28] Z. Yu, X. Niu, Z. Liu, Q. Pei, "Intrinsically stretchable polymer light-emitting devices using carbon nanotube-polymer composite electrodes," *Adv. Mater*. 23 (34), 3989-3994 (2011).

[29] T. Sekitani, H. Nakajima, H. Maeda, T. Fukushima, T. Aida, K. Hata and T. Someya, "Stretchable active-matrix organic light-emitting diode display using printable elastic conductors," *Nature materials 8*, 494-499 (2009).

[30] T.-B. Song and N. Li, “Emerging transparent conducting electrodes for organic light emitting devices,” *Electronics* 3, 190-204 (2014).

[31] D. R. Hodges, V. Palekis, S. Bhandaru, K. Singh, D. Morel, E. K. Stefenakos, and C. S. Ferekides: Mater. Res. Soc. Symp. Proc. Vol. 1165(2009).

[32] T. Tong, B Babatope, S. Admassie, J. Meng, O. Akwogu, W. Akande and W. O. Soboyejo, “Adhesion in Organic Structures,” *J. Appl. Phys.* 106, 083708 (2009).

[33] O. Akogwu, D. Kwabi, A. Munhutu, T. Tong, and W. O. Soboyejo, “Adhesion and cyclic stretching of Au thin film on poly(dimethyl-siloxane) for stretchable electronics,” *J. Appl. Phys.* 108, 123509 (2010).

[34] Veeco Instruments Inc.: Improving the Accuracy of AFM Measurements, the Thermal Tune Solution, Bruker Corporation, Billerica, MA (2005).

[35] W. W. Gerberich and M. J. Cordill, “Physics of adhesion,” Rep. Prog. Phys. **69**, 2157-2203 (2006).

[36] J. A. Greenwood, "Adhesion of Elastic Spheres." *Proc. R. Soc. Lond. A* 453, 1277-1297 (1997).

[37] V. H. H. Hertz, “Ueber die Berührung fester elastischer Körper,” *Journal für die reine und angewandte Mathematik (Crelle’s Journal)* 92, 156-171 (1882).

[38] K. L. Johnson and K. Kendall and A. D. Roberts, “Surface energy and the contact of elastic solids,” *Proc. R. Soc. Lond.,* A 324, 301–313 (1971).

[39] B. V. Derjaguin and V. M. Muller and Y. P. Toporov, “Effect of contact deformations on the adhesion of particles,” *J. Colloid Interface Sci.* 53, 314–325 (1975).

[40] D. Maugis and M. Barquins and R. Courtel, M´taux, "Corrosion," *Industrie* 605, 1 (1976).

[41] R. Carpick, D. Ogletree, and M. Salmeron, "A general equation for fitting contact area and friction vs load measurements," *J. Colloid Interface Sci.* 211, 395–400 (1999).

[42] J. W. Hutchinson, "The role of nonlinear substrate elasticity in the wrinkling of thin films," *Phil. Trans. R. Soc. A* 371, 20120422 (2013).

[43] H. Mei and R. Huang, 13th International Conference on Fracture, Beijing, China, 1-9 (2013).

[44] M. Watanabe, "Wrinkles with a well-ordered checkerboard pattern, created using dip-coating," *Soft Matter* 8, 1563-1569 (2012).

[45] Y. Ebata, A. B. Croll and A. J. Crosby, "Wrinkles and Strain Localizations in Polymer Thin Films," *Soft Matter* 8, 9086-9091 (2012).

[46] W. O. Akande, Y. Cao, N. Yao and W. Soboyejo, "Adhesion and the Cold Welding of Gold-Silver Thin Films", *J. Appl. Phys.* 107, 043519 (2010).

[47] D. Y. Momodu, T. Tong, M. G. Zebaze Kana, A. V. Chioh and W. O. Soboyejo, "Adhesion and degradation of organic and hybrid organic-inorganic light-emitting devices," *J. Appl. Phys.* **115**, 084504 (2014).

[48] N. Bowden, S. Brittain, A. G. Evans, J. W. Hutchinson and G. M. Whitesides, "Spontaneous Formation of Ordered Structures in Thin Films of Metals Supported on an Elastomeric Polymer," *Nature* 393, 146-149 (1998).

[49] Y. Qi, K. P. Prashant and M. C. McAlpine, "Enhanced piezoelectricity and stretchability in energy harvesting devices fabricated from buckled PZT ribbons," Proc. of SPIE **8031**, 8031R-1(2011).

[50] E. K. Hobbie, D. O. Simien, A. Fagan, J. Y. Huh, J. Y. Chung, S. D. Hudson, J. Obrzut, J. F. Douglas and C. M. Stafford, "Wrinkling and strain softening in single-wall carbon nanotube membranes," *J. Phys. Rev. Lett.* 104, 125505 (2010).

[51] Y. Wang, R. Yang, Z. Shi, L. Zhang, D. Shi, E. Wang, and G. Zhang, "Super-elastic graphene ripples for flexible strain sensors," *ACS Nano* **5**, 3645-3650 (2011).

[52] J. Hutchinson and Z. Suo, "Mixed-mode cracking in layered materials," *Adv. Appl. Mech.* 29, 63-191 (1991).

[53] Y. Mao, W. L. Wang, D. Wei, E. Kaxiras and J. G. Sodroski, "Graphene structures at an extreme degree of buckling," *ACS Nano.* 5, 1395-1400 (2011).

[54] H. Fei, H. Jiang and D-Y. Khang, "Nonsinusoidal buckling of thin gold films on elastomeric substrates," *J. Vac. Sci. Technol*. A **27**, L9-L12 (2009).

[55] H. Jiang, D-Y. Khang, H. Fei, H. Kim, Y. Huang, J. Xiao and John A. Rogers, "Finite width effect of thin-films buckling on compliant substrate: experimental and theoretical studies," J. Mech. Phys. Solids 56, 2585-2598 (2008).

[56] D-Y. Khang, H. Jiang, Y. Huang and J. A. Rogers, "A stretchable form of single-crystal silicon for high-performance electronics on rubber substrates," Science 13, 208-212 (2006).

[57] G. Domokos, P. Holmes and B. Royce, "Constrained euler buckling," J. Nonlinear Sci. **7**, 281-314 (1997).

[58] P. Holmes, G. Domokos and G. Hek, "Euler buckling in a potential field," J. Nonlinear Sci. 10, 477-505 (2000).

[59] J. Yin and X. Chen, "Effects of plasticity in buckling patterns of thin films on soft substrates," J. Phys. D: Appl. Phys. 44, 045401 (2011).

[60] H. Jiang, D-Y. Khang, H. Fei, H. Kim, Y. Huang, J. Xiao and John A. Rogers, "Finite width effect of thin-films buckling on compliant substrate: experimental and theoretical studies," *J. Mech. Phys. Solids* 56, 2585-2598 (2008).

[61] Z. Y. Huang, W. Hong, Z. Suo, "Nonlinear analyses of wrinkles in a film bonded to a compliant substrate," *J. Mech. Phys. Solids* 53, 2101-2118 (2005).

[62] A. Concha, J. W. McIver III, P. Mellado, D. Clarke, O. Tchernyshyov, and R. L. Leheny, "Wrinkling of a bilayer membrane," Phys. Rev. E 75, 016609 (2007).

[63] J. M. Harris, G. R. S. lyer, A. K. Bernhardt, J. Y. Huh, S. D. Hudson, J. A. Fagan and E. K. Hobbie, "Electronic Durability of Flexible Transparent Films from Type-Specific Single-Wall Carbon Nanotubes," *ACS Nano* 6, 881-887 (2012).

[64] M. Ramanathan, S. M. Kilbey II, Q. Ji, J. P. Hill and K. Ariga," Materials Self-assembly and Fabrication in Confined Spaces," *J. Mater. Chem. 22*, 10389-10405 (2012).

[65] Y. Wang, P. Kanjanaboos, E. Barry, S. Mcbride, X-M. Lin and H. M. Jaeger, "Fracture and failure of nanoparticle monolayers and multilayers," *Nano Lett.* 14, 826-830 (2014).

[66] J-Y Lee, S. T. Connor, Y. Cui and P. Peumans, "Semitransparent organic photovoltaic cells with laminated top electrode," *Nano Letter* 10, 1276-1279 (2010).

[67] J. Huang, G. Li and Y. Yang, "A semi-transparent plastic solar cell fabricated by a lamination process," *Adv. Mater.* 10, 415-419 (2008).

[68] T-F. Guo, S. Pyo, S-C Chang and Y. Yang, "High performance polymer light-emitting diode fabricated by a low temperature lamination process," *Adv. Funct. Mater.* 11(5), 339-343 (2001).

[69] T. Zyung, S. H. Kim, S-C. Lim, J. H. Lee, H. Y. Chu, J-K. Oh, "Novel method for combining flexible organic light-emitting diodes with organic thin-film transistors", *Journal of the Korean Physical Society* 48, S111-S114 (2005).

[70] R. F. M. Lange, Y. Luo, R. Polo and J. Zahnd, "The lamination of (multi) crystalline and thin film based photovoltaic modules, *Prog. Photovolt: Res. Appl.* (201), DOI:1-:1002/pip.993.

[71] M. B. Tucker, D. R. Hines and T. Li, "A quality map of transfer printing," *J. Appl. Phys.* 106, 103504 (2009).

[72] Y. Cao, C. Kim, S-R. Forrest and W. Soboyejo, "Effects of dust particles and layers properties on organic electronic devices fabricated by stamping," *J Appl. Phys.* 98, 033713 (2005).

[73] Y.-R. Jeng, M.-L. Guo, H.-C. Li and T.-F. Guo, "Interfacial morphology in polymer light-emitting diodes," *Electrochem. Solid-State Lett.* 10, D139-D141 (2007).

[74] J. Du, T. Tong, W. Akande, A. Tsakiridou, and W. Soboyejo, "Pressure Effects on the Lamination of Organic Light Emitting Devices," *J. Disp. Technol.* 9, 601–606 (2013).

[75] H. Wu, F. Lamantia, Y. Yang and Y. Cui, "Thin flexible secondary li-ion paper batteries," *ACSNano* 4, 5843-5848 (2010).

[76] Y. Zhang and Y.-P. Zhao, "A precise model for shape of an adhered microcantilever," *Sensors and Actuators A* 171, 381-390 (2011).

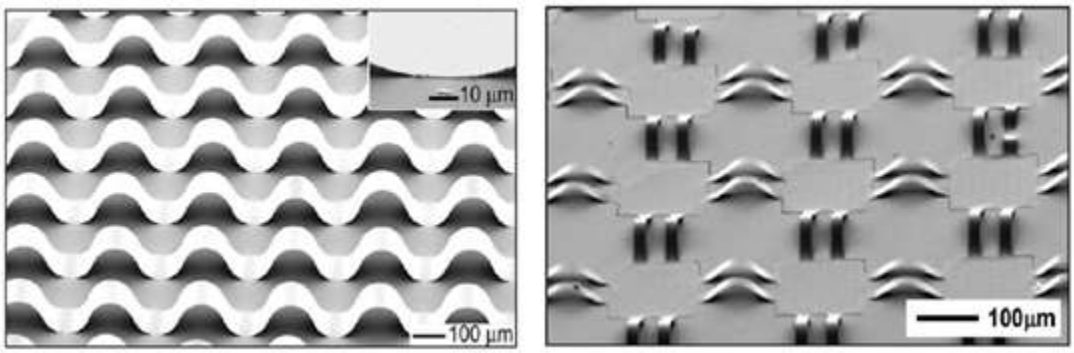

Figure 2.1: SEM images inorganic electronics of (a) gallium arsenide nanoribbons in buckled shapes where bonding to the PDMS substrate occurs only at the positions of the troughs and (b) SEM image of a silicon nanomembrane in a buckled, mesh layout on PDMS (Ref. 5)

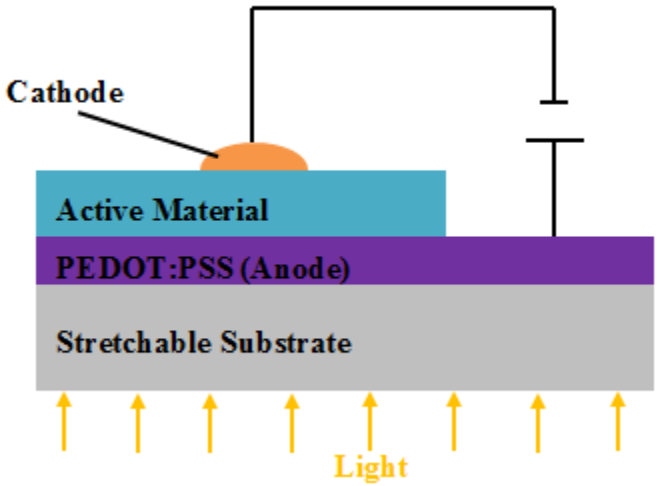

Figure 2.2: Schematic of a typical structure of stretchable organic solar cell

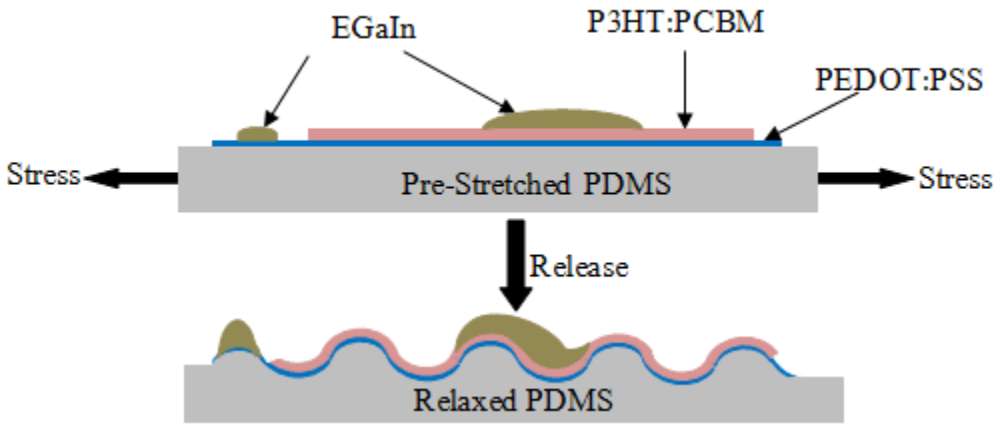

Figure 2.3: Failure mode strategy for stretchable solar cells

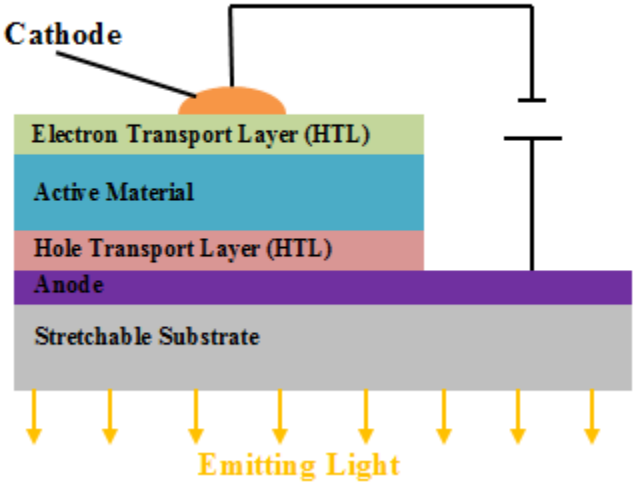

Figure 2.4: Organic light emitting devices

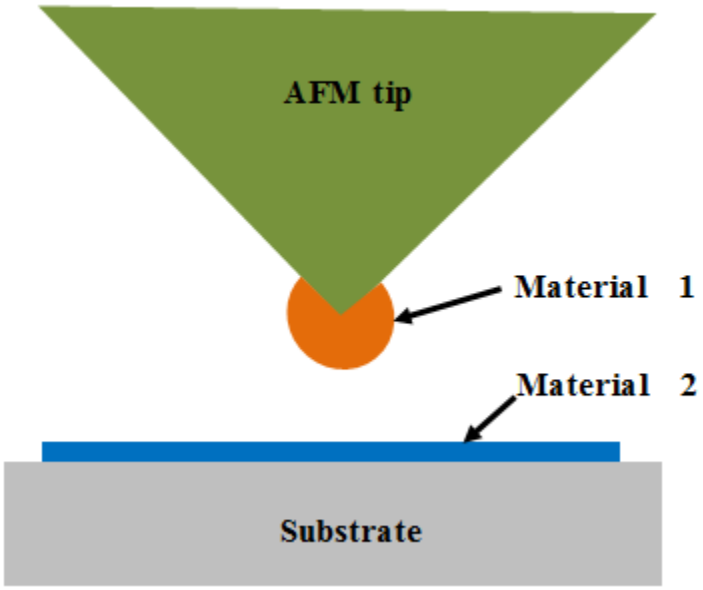

Figure 2.5: AFM adhesion measurement configuration

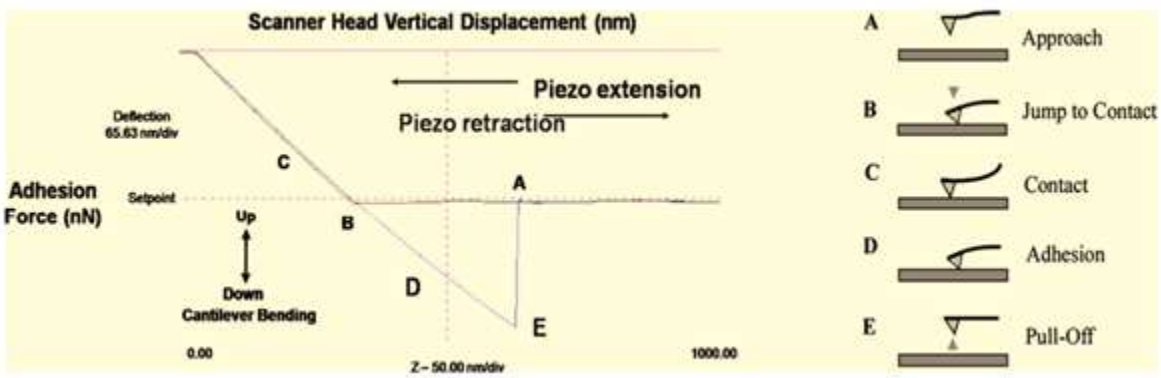

Figure 2.6: Schematic force-displacement curve depicting the various stages [(A)-(E)] of cantilever-surface engagement (Ref. 32)

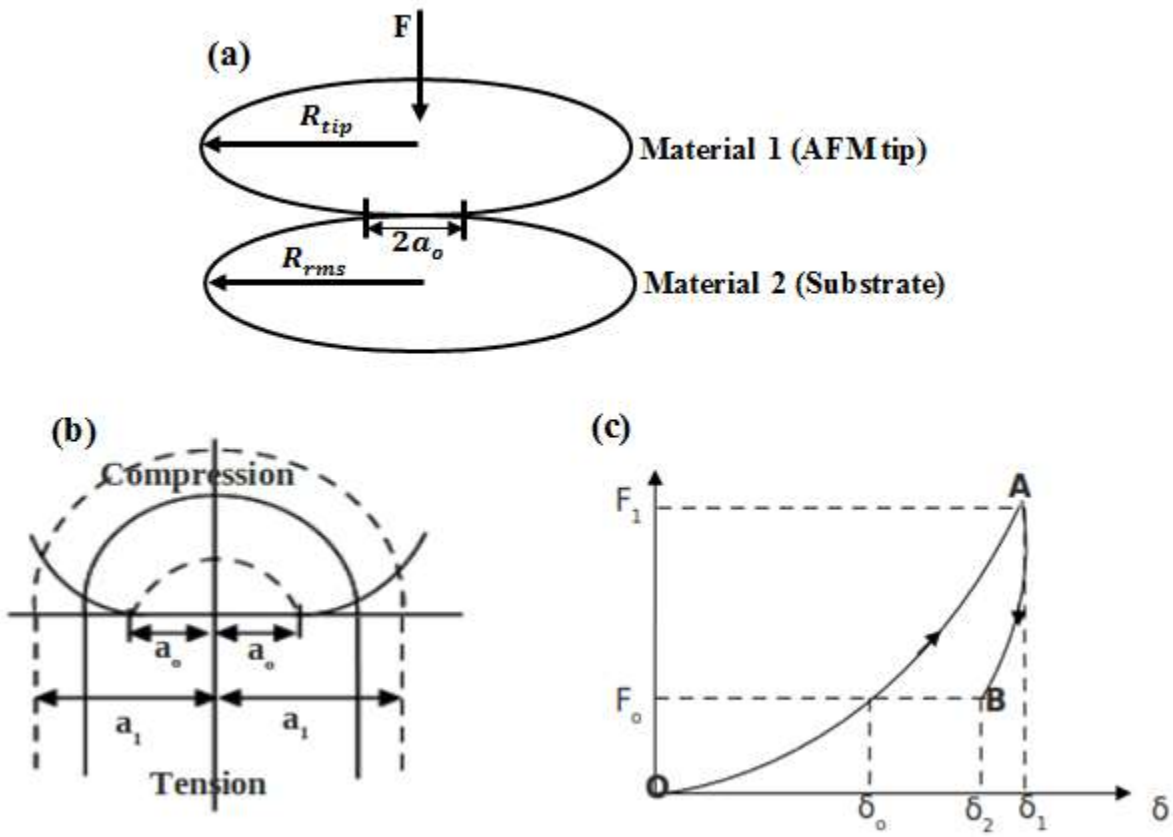

Figure 2.7: The Contact between two elastic surfaces, both in the presence (contact radius, a_1) and absence (Contact Radius, a_o) of the surface forces. (a) contact between AFM tip and substrate, (b) distribution of stress in contacting surfaces, and (c) force-displacement relation for contacting surfaces (Ref. 35)

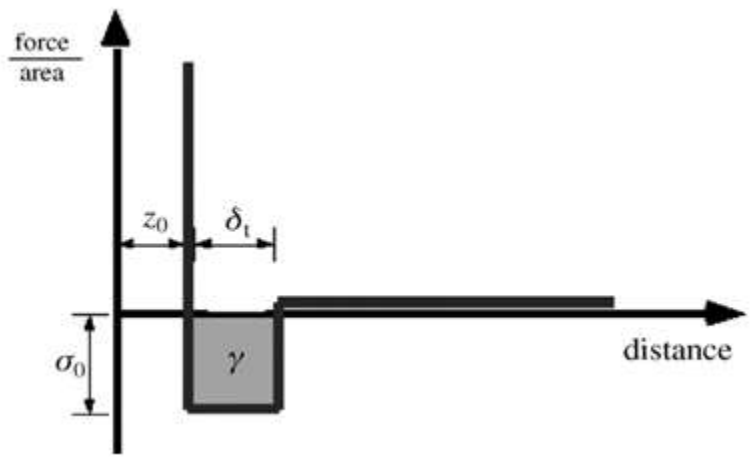

Figure 2.8: Force (per unit area)-distance relation for Dugdale model (Ref. 40)

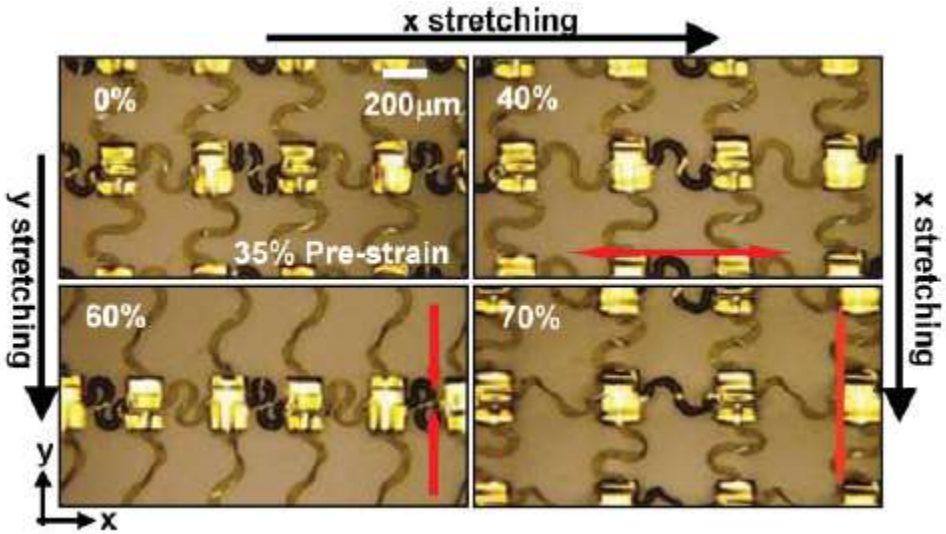

Figure 2.9: Optical images of stretching tests in the x- and y- directions. The labels for the legend give the strain magnitude in percent (Ref. 5)

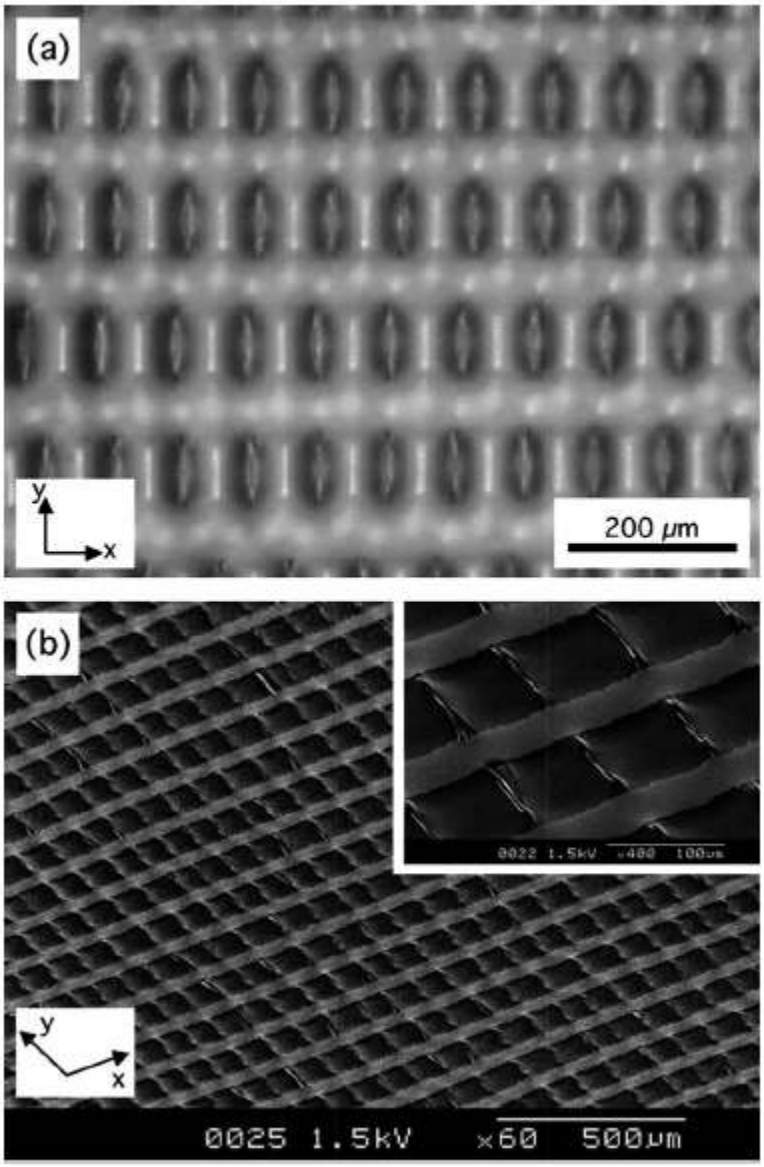

Figure 2.10: (a) Light and (b) scanning electron microscope images of wrinkles with a checkerboard pattern (Ref. 44)

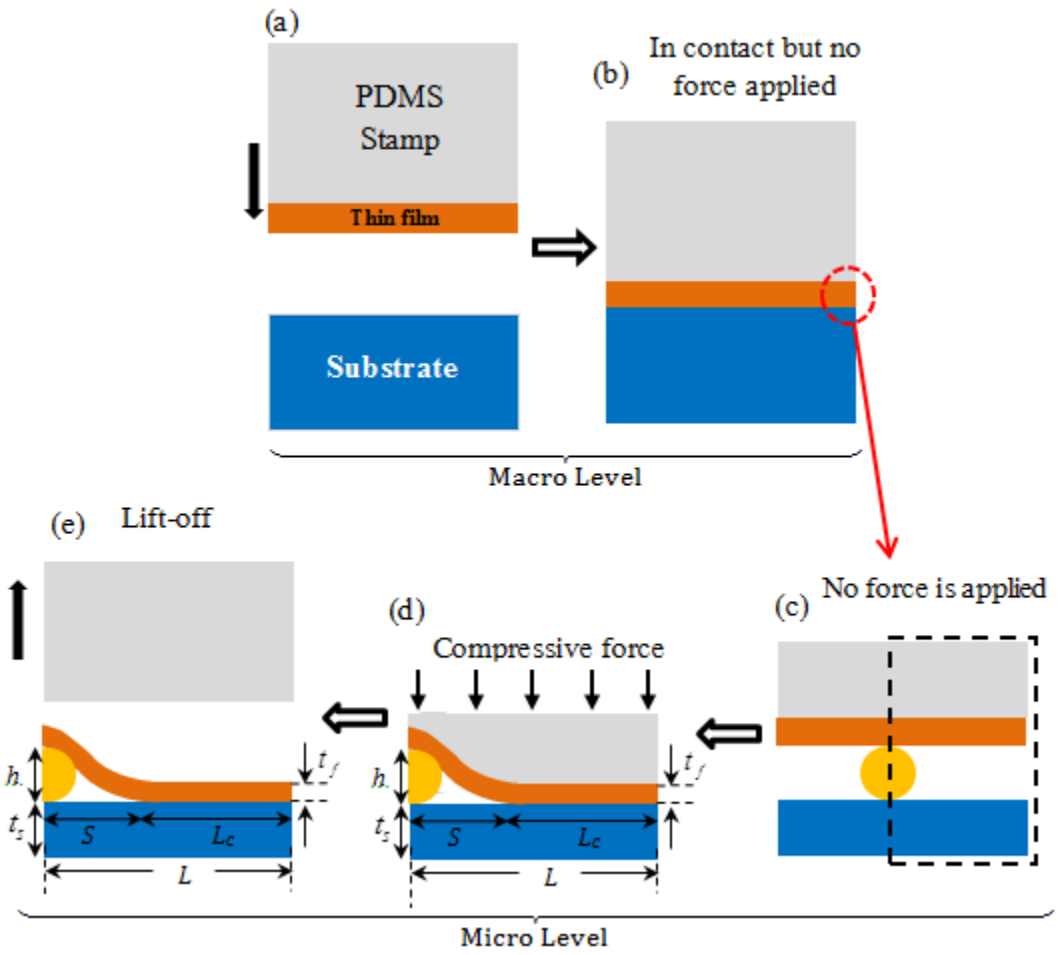

Figure 2.11: Schematic of macro/micro scale contact of a laminated thin film: (a) the thin-film coated stamp approaches substrate, (b) the thin film is in contact with the substrate but no force is applied to improve contact, (c) the micro scale of (b) with a an idealized dust particle (d) compressive force is applied to improve contact (e) the stamp is lifted off the laminated thin film.

CHAPTER 3

ADHESION IN STRETCHABLE/FLEXIBLE ORGANIC AND HYBRID ORGANIC/INORGANIC LIGHT EMITTING DEVICES AND SOLAR CELLS

3.1 Introduction

In this chapter, the results of an experimental study of adhesion between bi-material pairs that are relevant to stretchable/flexible organic and hybrid organic/inorganic light emitting devices and solar cells are presented. Atomic force microscopy (AFM) is used to measure the adhesion between the possible bi-material pairs that are relevant to organic and hybrid organic/inorganic light emitting devices and solar cells. The origins of the adhesion are then explored before discussing the implications of the results for the design of robust organic and hybrid organic/inorganic light emitting devices and solar cells.

The increasing interest in the development of organic light emitting devices with lower power consumption and higher resolution than traditional displays [1] demands engineering new ways of improving charge mobility and adhesion/contact within/between the layers of the electronic structures. There is also a potential for improving charge transport via incorporation of

nanoscale titanium dioxide (TiO_2) particles into the active layers of stretchable organic solar cells and light emitting devices [2] In the case of deformable electronic devices, the interfacial adhesion becomes very important.

This chapter is divided into 5 sections. Introduction is presented in section 1, while the theory of adhesion is presented in section 2. Section 3 presents the experimental procedures prior to results and discussion in section 4. The salient conclusion is then presented in section 5.

3.2 Theory

3.2.1 Atomic Force Microscopy (AFM) Force Measurement

The adhesion force between two materials can be measured by contact mode AFM [3, 4]. First, the AFM tip is coated with one material. The substrate is then coated with the second material in the bi-material pair. The steps for measuring the adhesion force are illustrated in Figure 2.6, along with a force-displacement curve associated with the tip deflection (A-E). The displacement of the AFM cantilever tip begins (at point A) above the substrate. As the tip is lowered towards the substrate, it will jump to contact (point B). Subsequent deflection of the tip is associated with elastic bending, as the tip is deflected (point C) to a maximum force/displacement. The tip deflection is then reversed until the tip is separated from the substrate. (point E). The adhesion force is determined from Hooke's law (Equation (2.1)).

3.2.2 Adhesion Energy

There are several possible theories that can be used to estimate the adhesion energy. These include the models described in Chapter 2, Section 2.3.2: the Derjaguin–Muller–Toporov (DMT) model [5]; the Johnson–Kendall–Robert (JKR) model [6]; and the Maugis-Dugdale (MD) model [7]. A non-dimensional parameter is determined to distinguish the use of these adhesion energy models [4-7]. If the parameter is smaller than 0.1, the DMT model applies. If it is greater than 5, the JKR model applies. The intermediate values correspond to the MD model. The DMT model applies to cases in which there are weak interactions between stiff materials with small radii. The application of the DMT model to similar scenarios was reported initially by Rahbar et al. [8]. This was extended by Meng et al. [9] to the study of adhesion in multilayered drug-eluting stents. The adhesion energy can be obtained from the adhesion force using Equation (2.27).

3.3 Experimental Procedures

3.3.1 Material Processing

The layered structures of the flexible organic and hybrid organic/inorganic light emitting devices are presented in Figures 3.1(a) and 3.1(b). The flexible organic light emitting device has the PDMS/Cr/PEDOT:PSS/MEH:PPV/Al structure, while the flexible hybrid organic/inorganic light emitting device has the PDMS/Cr/PEDOT:PSS/MEH:PPV:TiO_2/ Al structure. The layered structures of the flexible organic and hybrid organic/inorganic solar cells are presented in Figures

3.1(c)-3.1(e). The flexible organic solar cell has the PDMS/Cr/PEDOT:PSS/P3HT:PCBM/Al structure. However, in the flexible hybrid solar cell, the active layer of P3HT:PCBM blend was replaced with P3HT:TiO_2 or a mixture of P3HT:PCBM:TiO_2, with the other layers being the same as those in the flexible organic solar cell.

3.3.1.1 Processing of the Flexible Organic and Hybrid Organic/Inorganic Light Emitting Devices

In the case of the flexible organic light emitting devices (OLED), the PDMS substrate was prepared by first mixing a Sylgard 184 silicone elastomer curing agent with a Sylgard 184 silicone elastomer base (Dow Corning Corporation, Midland MI), with a 1:10 weight ratio. The mixture was then processed under a vacuum pressure of 6 kPa for 30 minutes. This was done to remove internal bubbles from the PDMS. This mixture was spin cast onto glass for 60 seconds. This was done at 400 revolutions per minute (rpm). The mixture was then cured for 2 hours at 80°C.

The chromium (Cr) adhesive layer of 5nm was deposited on top of the PDMS-coated glass using an electron-beam evaporator (Denton DV 502A, Denton Vacuum, Moorestown, NJ). Baytron P VP Al-4083 PEDOT:PSS (now Heraeus Clevios, Hanau, Germany) was filtered through a 0.2 μm filter to further improve uniformity and smoothness. The filtered mixture was spin-coated at 3000 rpm for 1 minute. It was then cured at 120°C for 5 minutes to remove moisture from the mixture.

The poly[2-methoxy-5-(2’-ethyl-hexyloxy)-1,4-phenylene vinylene] (MEH:PPV) (Sigma Aldrich, St. Louis, MO) was mixed with chloroform at a 5 g/L ratio. The mixture was stirred

continuously for 6 hours at room-temperature. It was then then passed through a 0.45 μm teflon filter, prior to spin-coating at 1000 rpm for 1 minute. Finally, a 100 nm thick aluminum (Al) cathode layer was thermally evaporated onto the MEH:PPV active layer using an Edwards E306A deposition system (Edwards, Sussex, UK).

However, in the case of the flexible hybrid light emitting devices, the active layer was prepared differently, with other layers being the same as the ones in the flexible organic light emitting device. The TiO_2 nanoparticles were added into the MEH:PPV single polymer blend to form MEH:PPV:TiO_2 mixtures/composites. Subsequently, 15 mg of MEH:PPV (in 2 mL of chloroform) was mixed at room-temperature for 6 hours. Consequently, 5 mg of TiO_2 was sonicated in 2 mL of chloroform for 45 minutes. The resulting two mixtures were then mixed and sonicated for 30 minutes.

3.3.1.2 Processing of flexible organic and hybrid organic/inorganic solar cells

In the case of the flexible organic solar cells, the PDMS substrate and Cr layer were prepared using procedures described previously in section 3.1.1. Baytron P PEDOT:PSS obtained from H. C. Starck (now Heraeus Clevios, Hanau, Germany) was used for the electron-hole pair separation. It served as the hole extraction layer. The PEDOT:PSS solution was filtered through a 0.2 μm filter. It was then spin-coated onto the PEDOT:PSS layer for 1 minute at 3000 rpm. It was cured for 5 minutes at 120°C. The bulk heterojunction active layer consisted of a mixture of poly(3-hexylthiophene) (P3HT, Sigma Aldrich, St. Louis, MO) and phenyl-C61-butyric acid

methyl ester (PCBM, Sigma Aldrich, St. Louis, MO). It was mixed with chloroform in the ratio of 1:0.8. This mixture was spin cast onto the PEDOT:PSS at 1500 rpm for 1 minute. It was then cured for 10 minutes at 150°C. Finally, the aluminum (Al) cathode layer was thermally evaporated onto the P3HT:PCBM active layer using an Edwards E306A deposition system (Edwards, Sussex, UK).

In the case of the flexible hybrid solar cells, the active layer was prepared differently, with other layers being prepared with the same protocols as the flexible organic solar cell. The active layer of the P3HT:TiO_2 or the P3HT:PCBM:TiO_2 blend was prepared as follows: For the P3HT:TiO_2 blend, the PCBM was replaced entirely with TiO_2 (Sigma Aldrich, St. Louis, MO). The best weight ratio of P3HT:TiO_2 blend was found to be 1:2.3 [10]. In the case of P3HT:PCBM:TiO_2 blend, the weight ratio was chosen to be 1:0.4:0.4. This ratio replaced half the PCBM with TiO_2. The TiO_2 nanoparticles were dissolved in chlorobenzene and sonicated for at least 30 minutes to form a uniform solution. The TiO_2 solution was then mixed with P3HT or P3HT:PCBM solution and placed in an ultrasonic bath for an additional 30 minutes. The blend was then spin coated for 60 seconds at 150 rpm, before annealing for 10 minutes at 150°C.

3.3.2 AFM Adhesion Experiments

Etched silicon contact mode AFM tips were purchased from Veeco Instruments (now Bruker Instruments) Woodbury, NY. The PDMS substrates were coated with Cr, while the AFM tips were coated separately with Cr and Al, using an Edwards E306A evaporation system (Edwards, Sussex, UK). The PDMS substrates were coated with Cr to improve their adhesion to PDMS

substrates. PEDOT:PSS solution was then spin-coated onto Cr-coated PDMS substrates. AFM tips were dip-coated with organic (P3HT:PCBM, MEH:PPV and P3HT) and organic/inorganic (P3HT:PCBM:TiO_2, MEH:PPV:TiO_2, P3HT:TiO_2 and TiO_2) active materials. To measure the adhesion forces between the active materials and Al, both organic and hybrid organic/inorganic active materials were spin-coated onto glass substrates. PCBM was also spin-coated onto glass in the order to measure the adhesion between P3HT (coated on the AFM tip) and PCBM (coated on glass).

The AFM measurements were performed in air of a temperature range of 22-25°C and a relative humidity range of 31-46%. A schematic of the interaction between the substrate (material 1) and the tip of AFM (material 2) is presented in Figure 3.2. About ten force-displacement curves were obtained for each interaction. The force-displacement measurements were obtained using a Digital Instruments Dimension 3000 AFM (Digital Instruments, Plainview, NY). The spring constant of each tip was measured using the thermal tune method [11]. The measurements were performed in a Digital Instruments Nanoscope IIIa atomic force microscope (Digital Instruments, Plainview, NY). The measurements of the tip deflections and the spring constants were then substituted into Equation (2.1) to determine the adhesion forces.

Due to the high sensitivity of AFM measurements to surface roughness, the substrate roughnesses and the tip radii were measured for each of the interaction pairs. The surface roughnesses were obtained using tapping mode AFM. About 10 height and phase images of each substrate were obtained. These were used to measure the root mean squared roughnesses in areas ranging from 1×1 to $10\times10\mu m^2$. The AFM tips were examined in a Scanning Electron Microscope (SEM) that was instrumented with an Energy Dispersive X-ray Spectroscopy (EDS)

system (Philips FEI XL30 FEG-SEM, Hillsboro, OR). This was done before and after the AFM adhesion measurements. The tip radii were calculated from tip images obtained from SEM (Figure 3.3). The measurements of the surface roughness and the tip radii were then used to estimate the effective tip radii and the adhesion energies from Equations (3.3) and (3.2), respectively. The SEM/EDS images of the AFM tips (before and after measurements) were also used to check for any changes in the morphology and atomic number contrast (composition differences) of the AFM tips after the AFM adhesion measurements. In this way, the SEM images of the AFM tips were used to check for possible occurrences of cohesive and adhesive failure.

3.4 Results and Discussion

3.4.1 Surface Characterization

3.4.1.1 Surface Morphologies and Roughness Measurements

The root mean squared (rms) surface roughnesses of the different layers in the organic light emitting device that were examined in this are presented in Figure 3.4. The average rms roughness values obtained for the different layers are presented in Table 3.1. The layers in the flexible light emitting device had low surface roughnesses that ranged from 0.6 nm to 2.4 nm, while the Cr layer had a higher roughness value of 9.9±2.2 nm. It is important to note that the surface roughness values obtained for PDMS spun on glass was very low (below 1 nm). This is expected from a conformal, elastomeric polymer surface. The average tip radius of the coated tip

was about 170 nm. Since the surface roughnesses were much smaller than the tip radii, it can be concluded from Equations (2.5) and (2.27) that the surface roughnesses dominated the adhesion energy calculations.

The different materials in the layers of the flexible solar cells exhibited different surface morphologies, as shown in Figure 3.5. The average rms roughness values obtained for the different layers are present in Table 2.1. The layers in the flexible solar cell had low rms surface roughness values, ranging from 0.6 nm to 2.4 nm, while the Cr layer had higher rms roughness values of ~ 9.9±2.2 nm. The average tip radius of the coated tip was about 180 nm. Since the surface roughnesses were much smaller than the tip radii, it can be concluded that the surface roughnesses dominated the adhesion energy calculations. In the SEM/EDS images of the tips, no significant changes were observed. Furthermore the highest magnification SEM images did not reveal any evidence of cohesive failure. Hence, we conclude that the measured AFM pull-off forces correspond to adhesive failures.

3.4.2 Adhesion of Flexible Organic and Hybrid Organic/Inorganic Light Emitting Devices

3.4.2.1 Adhesion Forces

The adhesion forces obtained for the bi-material pairs in the model flexible organic and hybrid light emitting device are summarized in Figure 3.6. These show that the adhesion force between PEDOT:PSS and MEH:PPV:TiO_2 had the highest value of 82 nN. The Cr layer also adhered well to the PDMS layer and also to the PEDOT:PSS layer. The adhesion force between

PEDOT:PSS and MEH:PPV was found to be 59 nN, while the adhesion force between the MEH:PPV and the Al layer was ~10 nN. The addition of TiO_2 nanoparticles to the MEH:PPV increased the adhesion force between PEDOT:PSS and MEH:PPV:TiO_2. Also, the adhesion force between the MEH:PPV:TiO_2 and Al layer was ~ 31 nN.

3.4.2.2 Adhesion Energies

The non-dimensional parameter for the calculation of the adhesion energy was found by performing the iterative calculations to be ~10^{-8}. Since this is << 0.1 [4, 12], the DMT model applies. By taking into account of the surface roughness and the AFM tip radius, the adhesion energy can be obtained from Equations (2.5) and (2.27). This DMT model had been used in this way for interfacial fracture toughness calculations [4, 8, 9, 12] in different multilayered structures. The adhesion energy results obtained for the bi-material pairs in flexible organic and hybrid light emitting devices are summarized in Figure 3.7. The results show that the Cr layer adhered strongly to the PDMS substrate, with a high adhesion energy of 18.9 J/m^2. The adhesion energy between PEDOT:PSS and MEH:PPV was 15 J/m^2. After adding TiO_2 nanoparticles to the MEH:PPV single polymer blend, the adhesion energy between PEDOT:PSS and MEH:PPV:TiO_2 had a higher value of 20.8 J/m^2.

It is important to note here that the increase in the adhesion energy of PEDOT:PSS-MEH:PPV:TiO_2 interface can be attributed to changes in surface morphology and phase separation of MEH:PPV:TiO_2, as well as electrochemical reactions between PEDOT:PSS and MEH:PPV:TiO_2. The latter occur due to the introduction of TiO_2. Similar phenomena have been

reported by Dauskardt and co-workers [13, 14] in research on P3HT:PCBM mixtures. Also, the adhesion energy between MEH:PPV and Al was 0.8 J/m^2. Furthermore, the addition of TiO_2 nanoparticles to the MEH:PPV single polymer blend resulting in an adhesion energy between MEH:PPV:TiO_2 and Al of 5.9 J/m^2. The hybrid light emitting device with the MEH:PPV:TiO_2 active layer, therefore, had higher adhesion energies at the two interfaces with its adjacent layers.

3.4.3 Adhesion of Flexible Organic and Hybrid Organic/Inorganic Solar Cells

3.4.3.1 Adhesion Forces

The adhesion forces obtained for the bi-material pairs in the model flexible organic and hybrid solar cell are summarized in Figure 3.8. The adhesive interactions in PEDOT:PSS-P3HT:TiO_2 and PEDOT:PSS-P3HT:PCBM:TiO_2 structures are compared with those of the PEDOT:PSS-P3HT:PCBM bi-material couples. The results show that the adhesive interactions between PEDOT:PSS and P3HT:PCBM result in the highest adhesion force of ~187 nN. The adhesive interactions between PEDOT:PSS and P3HT:TiO_2 had the second highest adhesion force values of 69 nN, while the adhesive interactions between PEDOT:PSS and P3HT:PCBM:TiO_2 resulted in the lowest adhesion forces of ~ 40 nN. The adhesion force between P3HT and TiO_2 was low, with a value of ~ 8 nN. The adhesive interactions between P3HT and PCBM resulted in an adhesion force of ~ 23 nN. The adhesive interactions of P3HT:TiO_2- Al and P3HT:PCBM:TiO_2- Al were compared with that of P3HT:PCBM-Al. The adhesion force between Al and P3HT:TiO_2 was the highest (306 nN), while that between Al and

P3HT:PCBM:TiO_2 had the second highest value of 140 nN. The lowest adhesion force of ~ 50 nN occurred between Al and P3HT:PCBM.

3.4.3.2 Adhesion Energies

The non-dimensional parameter for the calculation of the adhesion energy was found by performing the iterative calculations to be ~10^{-6}, which is << 0.1 [4, 12] Since the parameter is much smaller than 0.1, the DMT model applies. By taking into account of the surface roughness and the AFM tip radius, the adhesion energies were obtained from Equations (2.5) and (2.27). The adhesion energy results were presented in Figure 3.9 for the possible bi-material pairs in the flexible organic and hybrid solar cell.

The results presented in Figure 3.9 show that the Cr layer adhered strongly to the PDMS substrate, with the high adhesion energy of 18.9 J/m^2. The P3HT:PCBM layer adhered strongly to PEDOT:PSS layer, with the highest adhesion energy value of 40.3 J/m^2. The high adhesion energy of the PEDOT:PSS-P3HT:PCBM interface may be due to the physical intermixing of P3HT and PSS. These react electrochemically to form $P3HT^+$ and PSS^-, as reported by Brand et al. [13] and Huang et al. [15]. Also, the adhesion between PEDOT:PSS and P3HT:PCBM layer was much bigger than the adhesion energies of PEDOT:PSS-P3HT:TiO_2 and PEDOT:PSS-P3HT:PCBM:TiO_2. Furthermore, the adhesion energy between PEDOT:PSS and P3HT:TiO_2 was much greater than that between PEDOT:PSS and P3HT:PCBM:TiO_2.

It is also important to note here that the reduction in adhesion energy in PEDOT:PSS-P3HT:PCBM:TiO_2 can be attributed to possible effects of electrochemical reactions, due to

introduction of TiO_2 nanoparticles. This can be as a result of secondary bonds that are formed when hydrogen atoms in P3HT:PCBM are attracted to oxygen atoms in TiO_2 during the chemical reactions.

The adhesion energy between P3HT and TiO_2 had the lowest with a value of 0.1 J/m^2. The adhesion energy between P3HT and PCBM was also small (1.3 J/m^2). This is in the range of the values reported by Brand et al. [13]. Furthermore, considering the adhesion energies between Al and different active layers, the adhesion energy between Al and P3HT:TiO_2 was the highest (with a value of 25.8 J/m^2). This was greater than the adhesion energies of the Al-P3HT:PCBM:TiO_2 and the Al-P3HT:PCBM structure. Hence, from the robustness point of view, the active layer of P3HT:TiO_2 blend was more robust than the active layer consisting of P3HT:PCBM:TiO_2 blends.

3.5 Summary and Concluding Remarks

In this chapter, a force microscopy technique was used to measure the adhesion between possible bi-material pairs that are relevant to flexible organic and hybrid organic/inorganic light emitting devices and solar cells. A summary of the salient conclusions arising from this work is presented below.

1. The AFM technique provides a simple method for the ranking of the adhesion forces and energies between different layers in flexible organic and hybrid organic/inorganic light emitting devices and solar cells. This could facilitate the future design of robust flexible organic and hybrid organic/inorganic light emitting devices and solar cells.

2. In the case of the hybrid organic/inorganic light emitting device, in which the active layer of MEH:PPV blend is replaced by MEH:PPV:TiO_2 mixture, the MEH:PPV:TiO_2 active layer had higher adhesion energies with the adjacent layers (PEDOT:PSS and Al). Therefore, from the robustness point of view, the blended active layer of MEH:PPV:TiO_2 adheres better to the adjacent Al and PEDOT:PSS layers than the active layer consisting of MEH:PPV.
3. In the case of the hybrid organic/inorganic solar cell, in which the active layer of P3HT:PCBM blend is replaced with P3HT:TiO_2 or P3HT:PCBM:TiO_2 mixture, the P3HT:PCBM layer adhered better to the adjacent PEDOT:PSS and Al layers. However, although the incorporation of TiO_2 particles into the active layers has the potential of improving charge transport, the TiO_2 in the P3HT:TiO_2 layer reduces the adhesion to the adjacent PEDOT:PSS layer. Furthermore, the P3HT:PCBM:TiO_2 layer adheres poorly to the two adjacent layers (PEDOT:PSS and Al).
4. The incorportation of TiO_2 nanoparticles into the active layers of bulk heterojunction (P3HT:PCBM) organic solar cells reduces the adhesion to the adjacent hole transport and cathode layers. This is attributed to the potential effects of electrochemical reactions that are associated with the introduction of TiO_2. Hence, the improvements in charge transport facilitated by TiO_2 must, therefore, be balanced against potential reductions in the adhesion that might occur as a result of the incorporation of TiO_2 nanoparticles into the active layers of bulk heterojunction solar cells.

Table 3.1: Average rms roughness values for layers in the flexible light emitting device

Surface layer	Roughness (nm)
PDMS on glass	0.6±0.1
Cr	9.9±2.2
PEDOT:PSS	0.6 ± 0.1
MEH:PPV	2.2 ± 0.7
Al	2.4±0.4

Table 3.2: Average rms roughness values for layers in the flexible solar cells

Surface layer	Roughness (nm)
PDMS on glass	0.6±0.1
Cr	9.9±2.2
PEDOT:PSS	0.8±0.1
P3HT:PCBM	0.7±0.1
Al	2.4±0.4

3.6 References

[1] S. R. Forrest, "The road to high efficiency organic light emitting devices," Organic Electronics 4, 45-48 (2003).

[2] D.Y. Momodu, T. Tong, M. G. Zebaze Kana, A. V. Chioh and W. O. Soboyejo, "Adhesion and degradation of organic and hybrid organic-inorganic light-emitting devices," *J. Appl. Phys.* 115, 084504 (2014).

[3] T. Tong, B. Babatope, S. Admassie, J. Meng, O. Akwogu, W. Akande and W. O. Soboyejo, "Adhesion in Organic Structures," *J. Appl. Phys.* 106, 083708 (2009).

[4] O. Akogwu, D. Kwabi, A. Munhutu, T. Tong and W. O. Soboyejo, "Adhesion and cyclic stretching of Au thin film on poly(dimethyl-siloxane) for stretchable electronics," *J. Appl. Phys.* 108, 123509 (2010).

[5] B. V. Derjaguin and V. M. Muller and Y. P. Toporov, "Effect of contact deformations on the adhesion of particles," *J. Colloid Interface Sci.* 53, 314–325 (1975).

[6] K. L. Johnson and K. Kendall and A. D. Roberts, "Surface energy and the contact of elastic solids," *Proc. R. Soc. Lond.,* A 324, 301–313 (1971).

[7] D. Maugis, "Adhesion of spheres: The JKR-DMT transition using a Dugdale model*," J. Coll. Inter. Sci.* 150, 243-269 (1992).

[8] N. Rahbar, K. Wolf, A. Orana, R. Fennimore, Z. Zong, J. Meng, G. Papandreou, C. Maryanoff and W. Soboyejo, "Adhesion and interfacial fracture toughness between hard and soft materials," *J Appl. Phys.* 104, 103533 (2008).

[9] J. Meng, A. Orana, T. Tan, K. Wolf, N. Rahbar, H. Li, G. Papandreou, C. Maryanoff and W. Soboyejo, "Adhesion and interfacial fracture in drug-eluting stents," *J. Mater. Res.* 25, 641-647 (2010).

[10] C.Y. Kwong, A.B. Djuric, P.C. Chui, K.W. Cheng and W.K. Chan, "Influence of solvent on film morphology and device performance of poly(3-hexylthiophene):TiO_2 nanocomposite solar cells," *Chem. Phys. Lett.* 384, 372-375 (2004).

[11] Veeco Instruments Inc.: Improving the Accuracy of AFM Measurements, the Thermal Tune Solution, Bruker Corporation, Billerica, MA (2005).

[12] T. M. Tong, Adhesion and interfacial fracture: From organic light emitting devices and photovoltaic cells to solar lanterns for developing regions, PhD Thesis, Princeton University (2012).

[13] V. Brand, C. Bruner and R. H. Dauskardt, "Cohesion and device reliability in organic ... photovoltaic cells," *Solar Energy Materials and Solar Cells* 99, 182-189 (2012).

[14] C. Bruner and R. Dauskardt, "Role of molecular weight on the mechanical device properties of organic polymer solar cells," *Macromolecules* 47, 1117-1121 (2014).

[15] D. M. Huang, S. A. Mauger, S. Frieddrich, S. J. George, D. Dumitriu-LaGrange, S. Yoon, A. J. Moule, "The Consequences of interface mixing on organic photovoltaic device characteristics," *Adv. Funct. Mater*. 21, 1657-1665 (2011).

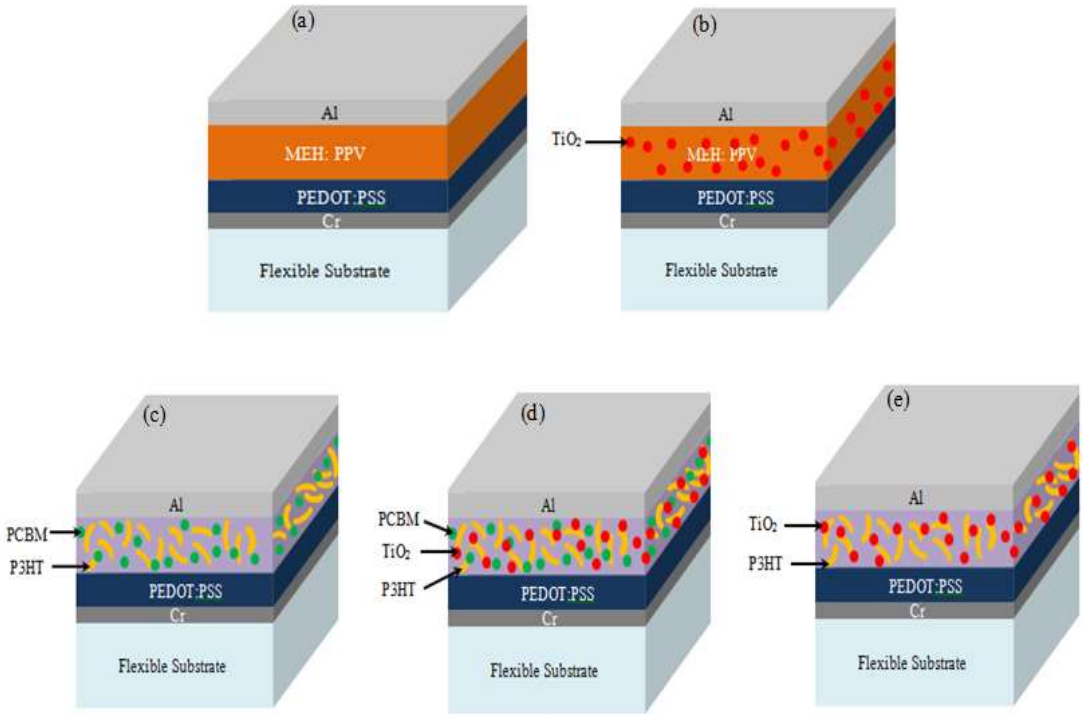

Figure 3.1: Layered structures for flexible organic and hybrid light emitting device and solar cells (a) flexible organic light emitting device (b) flexible hybrid light emitting device (c) flexible organic solar cell (d and e) flexible hybrid organic/inorganic solar cell.

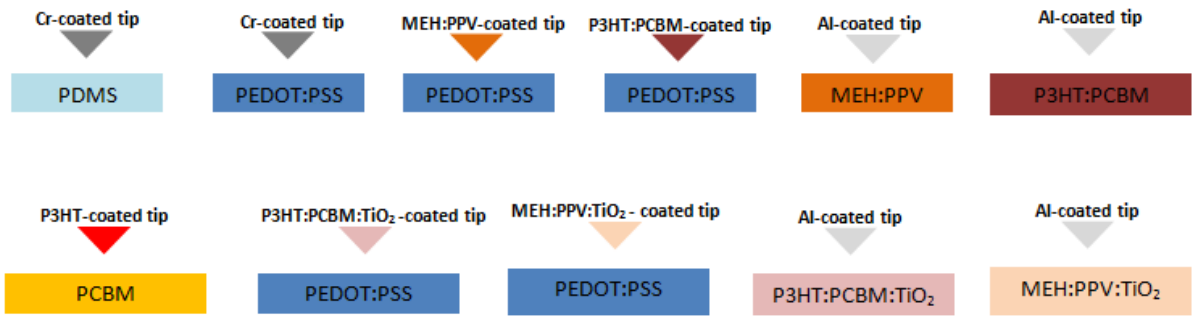

Figure 3.2: Schematic of interaction between material 1 and the tip of AFM (material 2)

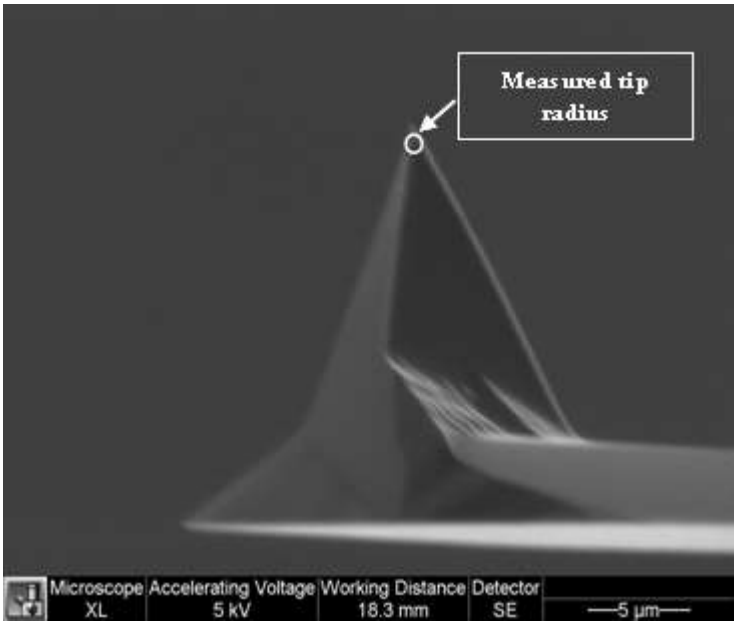

Figure 3.3: SEM image of a typical AFM tip profile.

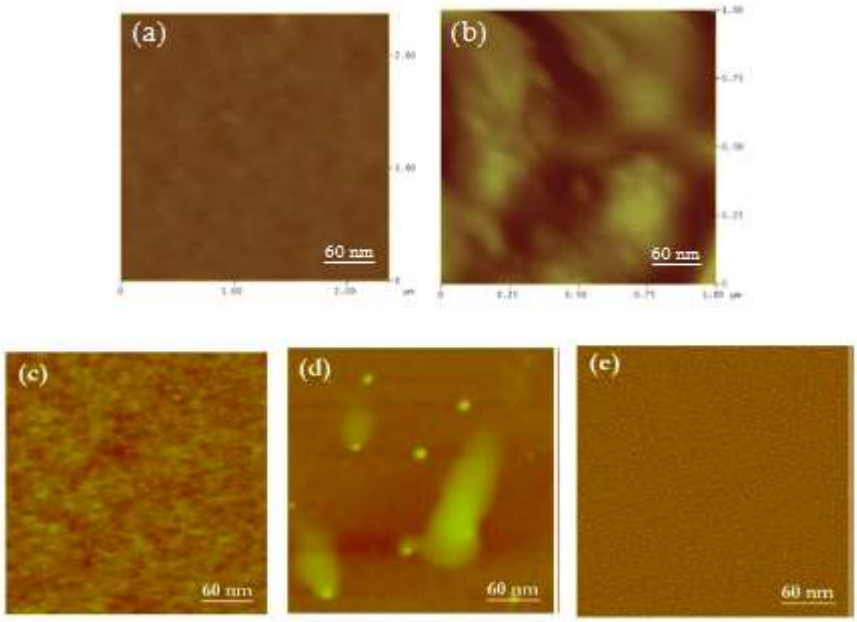

Figure 3.4: AFM surface morphologies for different layers in the flexible light emitting device: (a) PDMS (b) Cr (c) Baytron P VP AL-4083 PEDOT:PSS (d) MEH:PPV (e) Al.

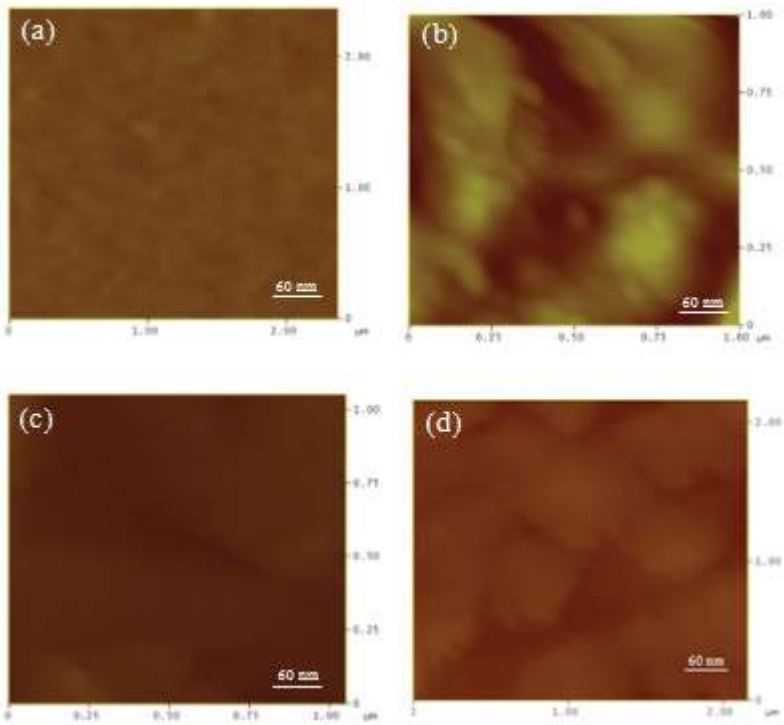

Figure 3.5: AFM surface morphologies for different layers in the flexible solar cells: (a) PDMS on glass (b) Cr (c) PEDOT:PSS (d) P3HT:PCBM.

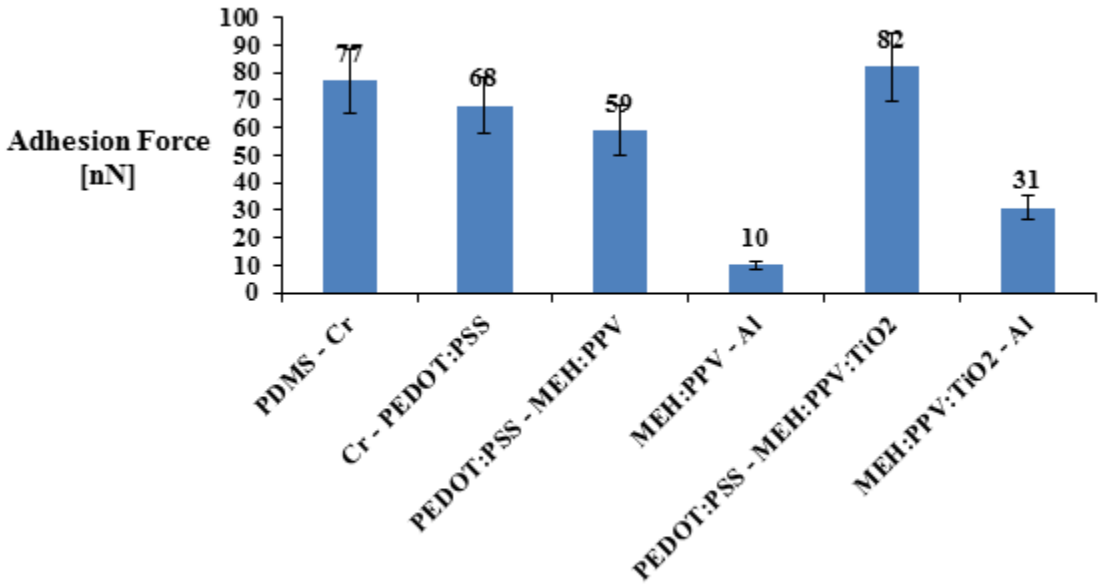

Figure 3.6: Interfacial adhesion forces in flexible organic and hybrid organic/inorganic light emitting devices.

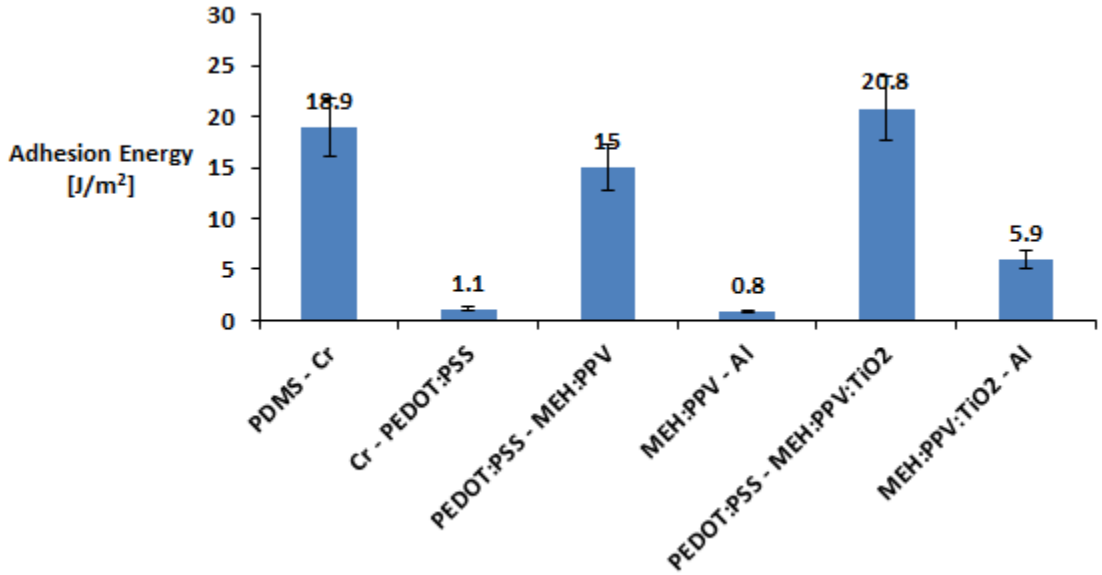

Figure 3.7: Interfacial adhesion energies in flexible organic and hybrid organic/inorganic light emitting devices.

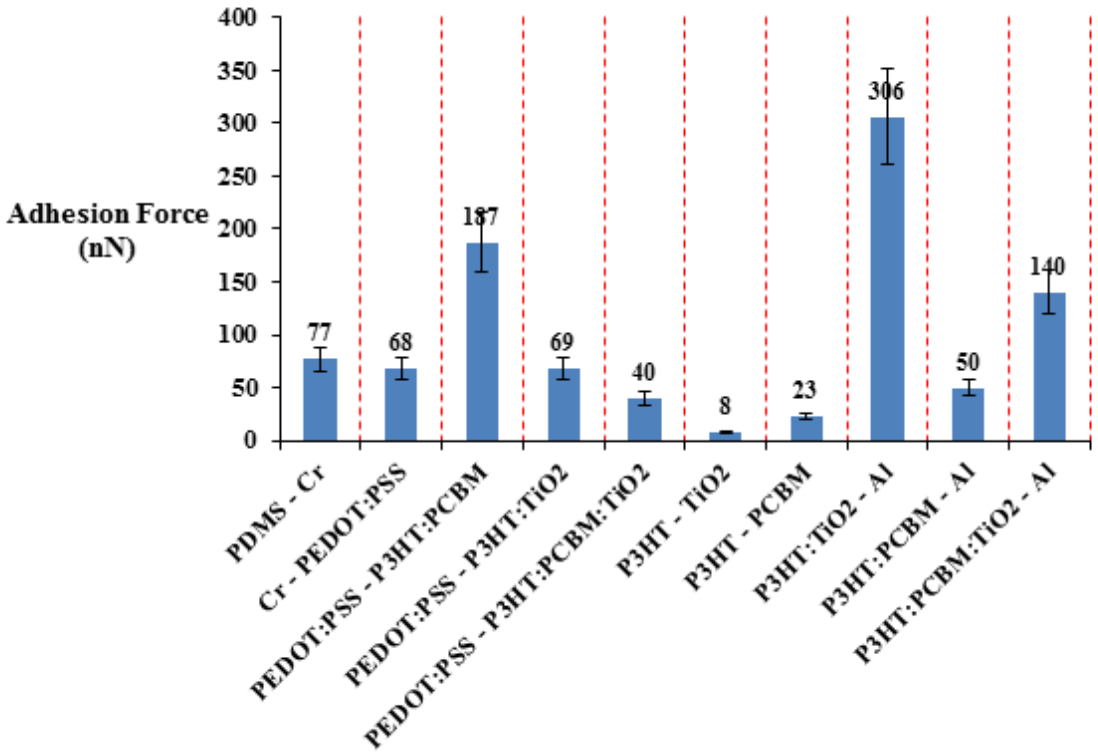

Figure 3.8: Interfacial adhesion forces in flexible organic and hybrid organic/inorganic solar cell.

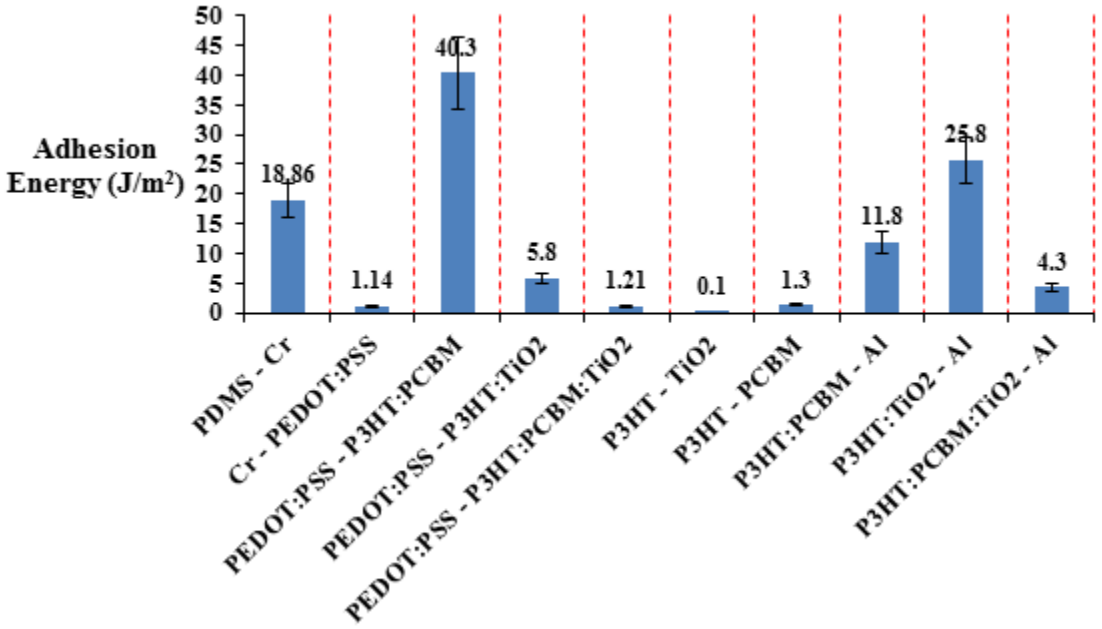

Figure 3.9: Interfacial adhesion energies in flexible organic and hybrid organic/inorganic solar cell.

CHAPTER 4

LAMINATION OF ORGANIC SOLAR CELLS AND ORGANIC LIGHT EMITTING DEVICES

4.1 Introduction

In electronic industry, there are needs for simple and cheap fabrication methods. In the case of organic solar cells and organic light emitting devices that involve solution process, lamination method has been seen as a simple and cheap technique that is probable for fabrication [1-8]. In most of the prior work on the lamination of organic solar cells and organic light emitting devices, more of experimental work, with limited modeling has been used. There is, therefore, a need for combined experimental, computational and analytical approaches that are designed to provide general insights for the design of lamination processes that are relevant to organic photovoltaic cells (OPVs) and organic light emitting devices (OLEDs). This will be explored in this chapter using a combination of experiments and models that are designed to provide insights for the design of lamination processes that are relevant to OLEDs and OPVs.

This chapter is divided into five sections. The introduction is presented in section 4.1, while the contact and pull-off models are presented in section 4.2. The experimental procedures are then described in section 4.3 before presenting the results and discussion in section 4.4. Salient conclusions arising from this work are summarized in section 4.5.

4.2 Modeling

In an effort to laminate low-cost organic solar cells, analytical modeling and computational modeling were used to study interfacial contacts that occur during pre-lamination, as well as the interfacial failure that occurs during the interfacial separation associated with the lamination process. The success of the lamination depends on which of the two interfaces involved in the process fails first (Figure 4.1) [9].

If the top interface (between the PDMS stamp and the transferred layer) fails before the critical condition for bottom interfacial failure is reached between the transferred layer and the substrate, the lamination is considered to be successful [9]. On the other hand, if the interface between the transferred layer and the substrate fails before the critical condition for interfacial failure between the poly-di-methyl-siloxane (PDMS) stamp and the transferred layer, the lamination is deemed unsuccessful. The various possible results of separation in the lamination process have been described by Tucker et al. [9].

4.2.1 Adhesive Surface Contacts

Structures of OPV and OLED cells are typically fabricated from multilayers in contact. Each of these layers should have the right work function alignment for increased charge transport to occur across the interfaces. However, improved contact at inorganic/organic and organic/organic material interfaces can also be enhanced by improved adhesion [10] and the application of pressure [11]. There is, therefore, a need to explore the effects of adhesion and pressure on the contacts between adjacent layers in organic electronic structures.

In the case of low cost lamination techniques that are used for the fabrication of OPVs and OLEDs, the layer to be laminated is often coated onto a poly-di-methyl-siloxane (PDMS) stamp before transferring it to a substrate. During this process, as the coated-PDMS stamp approaches the layered substrate (Figure 2.11a), the presence of distributed particles limits the contact with the underlying substrate. This results in the formation of voids as the layers wrap around the surface of impurities to create interfacial voids [8]. Such particles have been revealed in prior focused ion beam microscopy work by Akande [7]. These have shown that nano-scale and micro-scale voids can form at the interfaces, depending on the sizes of the interfacial impurities (Figures 2.11c and 2.11d). Hence, the application of pressure can increase the contact of stamps around interfaces that are relevant to OPVs and OLEDs.

The surface contact length that can be achieved can be estimated using an analytical model of contact around a dust particle. This is done by considering a scenario in which the particles of heights, h, are idealized between the transferred layer of thickness, t_f, and the substrate of thickness, t_s. The transferred layer of length, L, can be likened to a cantilever beam that bent to

an S-shape (Figure 2.11e) [6, 7] under uniform compressed force, F, on the stamp. The relationship between the contact length and applied force, F, is given by Equation (2.39). Using the material properties presented in Table 4.1, the normalized contact length can be calculated as a function of the applied compressive force.

4.2.2 Fracture Mechanics Modeling

The lamination of a thin film layer from a coated stamp to a substrate is basically in two stages: pre-lamination and lift-off. During pre-lamination, a compressive force is applied to the stamp to ensure that the layer makes good contact with the substrate. In the case of lift-off, a lift-off force is applied to separate the stamp from the laminated layer. This lift-off process will be considered as an interfacial fracture process in this study. During the pre-lamination process, the application of uniform compressive force (as described above in section 4.2.1) can induce stresses in layered organic electronics. The stress concentrations become more significant when the dust particles are sandwiched between the interfaces. This can lead ultimately to interfacial crack growth and fracture in the layered structure.

Prior work on the fracture mechanics modeling of pre-lamination and interfacial fracture of OLEDs and OPVs has been carried out by Li [9] for transfer printing. However, the sizes of the particle can affect the interfacial mechanics during the separation of stamps from the laminated structures, as described by Cao et al. [8]. During the separation process at the micro scale (Figures 4.1a, 4.1b and 4.1c), the following are possible:

(i) steady interfacial delamination between the transferred layer and substrate - unsuccessful lamination (Figure 4.1b);

(ii) steady interfacial delamination between PDMS stamp and transferred layer - successful lamination (Figure 4.1a);

(iii) possible simultaneous delamination in interfaces of the transferred layer/substrate, and the PDMS stamp/transferred layer – partial lamination (Figure 4.1c).

In an effort to model the fracture processes involved in lift-off process, Figure 4.1 shows an idealized nano particle between the layered interfaces produced after pre-lamination. Edge cracks are also idealized between the transferred layer and stamp and/or between transferred layer and substrate. The energy release rate at the tips of the edge cracks are measures of the crack driving force. In general, the energy release rate of the interfacial crack between the laminated film and the substrate is a function of plane strain elastic moduli of the film, $\overline{E}_f$, and substrate, $\overline{E}_s$, the length of top interfacial crack, d_t, the length of the bottom interfacial crack, d_b, the thickness of the film, t_f, thickness of the substrate, t_s and the lift-up stress, σ. This is given by:

$$G = f(\overline{E}_s, \overline{E}_f, t_t, t_s, d_b, d_t, \sigma) \tag{4.1}$$

where $\overline{E}_f = E_f/(1-\nu^2)$ and $\overline{E}_s = E_s/(1-\nu^2)$. The Using Buckingham pi-theorem method of dimensional analysis (Appendix A), Equation (4.1) can be expressed as:

$$G = f\left(\frac{\overline{E}_s}{\overline{E}_f}, \frac{t_s}{t_f}, \frac{d_b}{t_f}, \frac{d_t}{t_f}\right)\frac{\sigma^2 t_f}{\overline{E}_f} \tag{4.2}$$

Since $\sigma = F_{Lift-off} / wL$, where $F_{Lift-off}$ is the lift-up force, Equation (4.2) can be written as:

$$G = f\left(\frac{\overline{E}_s}{\overline{E}_f}, \frac{t_s}{t_f}, \frac{d_b}{t_f}, \frac{d_t}{t_f}\right)\frac{F_{Lift-off}^2 t_f}{w^2 L^2 \overline{E}_f} \tag{4.3}$$

where w and L are the width and length of the structure respectively.

4.2.3 Computational Modeling

The ABAQUS^{TM} software package (ABAQUS 6.12, Dassault Systèmes Incorporation, Rhoda Island) was used to simulate the changes of contact profiles between the transferred layer and the substrate during pre-lamination along with the possible interfacial failure during the separation of the stamp from the transferred (laminated) layer. First, the effects of applied forces (on the surface contact lengths of the active layers of OPV cells and OLEDs) were simulated on poly(3,4-ethylenedioxythiophene):polystyrene sulfonate (PEDOT:PSS)-coated substrates. It was also assumed that particles are sandwiched between the laminated layer and the substrate. The size ranges ($\sim 0.1-10\mu m$) are typical of particles that are present in clean room environments. These include: silicon, organics and other dust particles that are often found in the clean room environment [8].

By considering a unit width $(w=1)$, axisymmetric models were developed using the ABAQUS software package. A four-node elemental mesh was used. The elements were dense near the particles and the contact surface (Figure 4.2). The bottom boundary of the substrate was fixed for stability during the simulations, while a range of uniform forces $(0\,N - 500\,N)$ was

applied to the top of the stamp (Figure 4.3). The materials used (Table 4.1) were assumed to exhibit isotropic behavior. Also, the height of the particle was varied, while the length of the contact surface was studied as a function of the applied force. This was done for laminating layers of model OPVs and OLEDs.

In the case of interfacial failure (during the separation of PDMS stamps from the laminated layered structures in the lift-off process in lamination), 2D models (with a unit width) were built using the ABAQUS^{TM} software. These were used to study the interfacial cracking between the laminated layer and the stamp (top interface), as well as the interfacial cracking between the laminated layer and the substrate (bottom interface). Again, a four-node elemental mesh was used, while the elements were dense near the crack tips. The finite element simulations were used to determine the interfacial fracture energies corresponding to the lift-off forces that were applied to separate the stamps from the laminated film materials.

In the lamination process, two different interfaces (the top and the bottom) are possible. By assuming respective existing edge cracks of lengths, d_t and d_b , at the top and bottom interfaces, the energy release rate at the tip of the edge crack at the top interface is denoted as G_t, while the energy release rate at the tip of the edge crack at the bottom interface is denoted as G_b. The thicknesses of the layers were maintained constant, while the energy release rates of the crack tips were calculated using J-integral as functions of the crack length. The energy release rates of the interfacial crack tips were computed for a range of applied lift-off forces.

The success of the lamination process can be explained in form of differentials of the driving forces of the propagating cracks along the interfaces that are involved in the process [9]. At a

critical condition, the differential of the interfacial energy release rates (G_t^c and G_b^c) of the edge cracks at the top and bottom interfaces can be expressed as:

$$\frac{G_t}{G_b} = \frac{G_t^c}{G_b^c} \tag{4.4}$$

where G_t^c and G_b^c are the critical interfacial energy release rates at the top and bottom interfaces, respectively. If $G_t/G_b > G_t^c/G_b^c$, the interfacial crack will propagate along the top interface. This will result ultimately in the delamination of the stamp from the transferred layer. In this case, the lamination is successful. However, the lamination will be considered unsuccessful, if $G_t/G_b < G_t^c/G_b^c$; the crack propagates along the bottom interface, causing delamination of the laminated layer from the substrate. In these two scenarios, the lift-up force for successful lamination of materials in OPVs and OLEDs can be predicted.

4.3 Experimental Methods

4.3.1 Pre-lamination of Layers of OPV Cells and OLEDs

First, the PDMS substrate was prepared by mixing a Sylgard 184 silicone elastomer curing agent with a Sylgard 184 silicone elastomer base (Dow Corning Corporation, Midland MI) with a 1:10 weight ratio. Then the mixture was then processed under a vacuum pressure of 6 kPa for 30 minutes. This was done to eliminate all of the possible bubbles. The processed PDMS was then poured into a flat aluminum mold with dimensions of $15\ mm \times 10\ mm \times 2\ mm$. This was

followed by annealing in an oven at 80°C for 2 hours, resulting in the formation of a ~2 mm thick PDMS stamp. The PEDOT:PSS solution (Hareous, Clevios, Hanau, Germany) was spin-coated onto a clean glass slide at 3000 rpm for 1 min to obtain a film with thickness of 100 nm.

In the case of the OLED, the poly [2-methoxy-5-(2-ethyl-hexyloxy)-1,4-phenylene vinylene] (MEH-PPV) solute (Sigma Aldrich, St. Louis, MO) was mixed with chloroform (at a 5 g/l solute –solvent ratio) to form a solution. The mixture was stirred continuously for 6 hours at room-temperature before passing it through a 0.45 μm teflon filter. The cured PDMS was attached to a flat stub using a double-sided tape. This was done before dip coating the PDMS stamp with MEH-PPV solution. The stub was then attached to the head of an Instron machine (Instron 5848, Canton, MA, USA) along with the PEDOT:PSS-coated glass plate that was fixed under the dip-coated PDMS stamp. The MEH-PPV was laminated onto PEDOT:PSS by applying loads in the ranges from 100 N to 500 N for 2 minutes before lift-off. The stamp was lifted 3 mm apart from the laminated MEH-PPV with the head of the Instron testing machine moving up at a displacement rate of 0.01mm/s.

For the lamination of the OPV cells, the poly (3-ethylthiophene) (P3HT) (Sigma Aldrich, St. Louis, MO): phenyl-C61-butyric acid methyl ester (PCBM) (Sigma Aldrich, St. Louis, MO) layer was first prepared by mixing P3HT and PCBM in chlorobenzene. This was mixed in ratio of 1:0.8 by weight. The mixture was then stirred continuously for 5 hours at room temperature, before spin coating it onto the PDMS stamp at 750 rpm for 30 seconds. The P3HT:PCBM was laminated from the P3HT:PCBM-coated stamp to the PEDOT:PSS layer with the same protocol that was used for the lamination of the MEH-PPV layer in the OLED structure. The surfaces of

the stamp and the substrate were analyzed (before and after lamination) using atomic force microscopy (AFM) and scanning electron microscopy (SEM).

4.3.2 Pull-off of the Laminated and Spin-coated Active Layers

First, a sticky foam pad with a cross sectional area 25 mm x 8 mm was cut and attached to a stub using a double-sided tape. The stub was then attached to the head of an Instron testing machine, while the bottom of the substrate (P3HT:PCBM/PEDOT:PSS/glass) was attached to the bottom stub. Note that the double-sided tape covered the sectional area that was used to pull-off the laminated active layer. The sticky foam pad was brought into contact with the P3HT:PCBM layer with a near zero force. This was done before scratching off the active layer on the border of the foam pad to maintain the same stress state in each sample. A schematic of the experimental set-up is presented in Figure 4.4.

A load of 100 N was applied to the pad for 60 seconds. This load was then maintained for another 60 seconds, before lifting up the head at a rate of 0.01 mm/s. The same protocol was applied for the pull-off of the laminated MEH-PPV, as well as the spin-coated MEH-PPV and P3HT:PCBM. In each case, the force-displacement curves were obtained. The surface of substrate (PEDOT:PSS/glass) were also observed using AFM.

4.4 Results and Discussion

4.4.1 Modeling of Contact during Pre-lamination

The effects of the compressive force (on the contacts between the active layers and PEDOT:PSS-coated substrates of the organic light emitting devices and organic solar cells) are presented in Figure 4.5. The results obtained from the analytical (Equation 2.39) and computational modeling show that the contact lengths between pre-lamination of P3HT:PCBM (Figure 4.5a) or MEH-PPV (Figure 4.5b) onto the substrates. These increase with increasing applied force.

The pre-laminated active layers sink more into the substrate as the applied force increases. The sink-in is more significant in the case of flexible PDMS substrates. These results suggest that, in the case of rigid and flexible substrates, the desired good interfacial contact between the active layers and substrates can be damaged due to excessive applied force. The results show that at an applied force of ~250 N, the predicted the contact length is ~95 % (by FEM) and ~100% (by analytical model).

4.4.2 Pre-lamination of Active Layers

In this section, the force needed to separate the stamp from the pre-laminated active layers is determined. It is important to note here that the stamp can be separated from pre-laminated layers if the interfacial contact between the active layers and the substrate is maintained with the applied pre-laminated compressive force. The force-displacement curves for successful pre-

lamination of P3HT:PCBM and MEH-PPV onto PEDOT:PSS-coated glass are presented in Figure 4.6. First, the force increases with increasing displacement, before returning to zero force. At an applied compressive force of ~200 N, the force-displacement curves have a peak ~0.0 6 N for pre-lamination of P3HT:PCBM and ~1.10 N for pre-lamination of MEH-PPV. The peaks of the curves represent the interfacial work of adhesion in the top interfaces (stamp/P3HT:PCBM and stamp/MEH-PPV) of the active layers.

4.4.3 Pull-off Experiments

The results of the pull-off tests (on the laminated and spin-coated active layers) are presented in Figures 4.7. The peaks of the force-displacement curves represent the interfacial adhesion force between the active layers and the PEDOT:PSS-coated substrates. In Figure 4.7, the adhesion force in laminated MEH:PPV/PEDOT:PSS (Figure 4.7b) is comparable to the adhesion force, when the P3HT:PCBM is spin-coated onto the substrate. In the case of P3HT:PCBM/PEDOT:PSS-coated glass, shown in Figure 4.7c and 4.7d, the adhesion forces obtained from the lamination and spin-coating techniques are also comparable.

From the results, the adhesion forces at the interfaces of P3HT:PCBM/PEDOT:PSS- coated glass substrate and MEH:PPV/PEDOT:PSS-glass (Figures 4.7a-4.7d) are more than the measured adhesion forces at the interfaces of Stamp/P3HT:PCBM (Figure 4.6a) and Stamp/MEH:PPV (Figure 4.6b), respectively. This suggests that the lamination of organic active layers of OPV cells and OLEDs can be improved in the case where the active layers are deposited on PEDOT:PPS-coated substrates. Since the adhesion forces between the active layers

and the substrates are more than the adhesion forces between stamps and the active layers, the stamps can be removed easily from the laminated active layers, without damaging the interfaces between the active layers and PEDOT:PSS-coated glass.

Typical AFM images of the substrates (after the pull-off of MEH-PPV and P3HT:PCBM) are presented in Figure 4.8. In the case of successful lamination, no remnant of the pulled-off MEH-PPV and P3HT:PCBM were observed on the substrates after pull-off (Figures 4.8a and 4.8b). The patches of the laminated MEH-PPV and P3HT:PCBM layers are evident in the case where the layers are not fully pulled off from the substrate (Figures 4.8c and 4.8d).

4.4.4 Interfacial Fracture During Lift-off

It is crucial to understand the fracture along the interfaces that are involved in the lift-off stage of the lamination process. For successful lamination of any layer onto a substrate, the stamp must be lifted up successfully without damaging the interface of interest (laminated active layers/substrates). The different categories of the possible laminations that can be achieved, based on the properties of the interfaces, have been described previously in section 4.2.2.

First, the bottom interface was maintained intact with zero edge crack length. This was done to calculate the interfacial energy release rate as a function of edge crack length at the top interface. This was done for both the lamination of P3HT:PCBM and MEH:PPV onto PEDOT:PSS-coated glass substrates. The interfacial energy release rates of the crack tips at the bottom interfaces (P3HT:PCBM/PEDOT:PSS-coated glass and MEH:PPV/ PEDOT:PSS-coated glass) were also calculated for different lengths of the bottom edge cracks, keeping the top

(stamp/P3HT:PCBM and stamp/MEH:PPV) edge crack length at zero. In both cases, the top and bottom energy release rates increased with increasing crack length.

The difference between the energy release rates at the top and bottom interfaces can be observed clearly at short crack lengths (Figure 4.9). However, at longer crack lengths, there were no significant differences between the energy release rates of the top and bottom interfaces. Similar results have been reported by Tucker et al. [9]. The significant difference in the energy release rates at short crack lengths is attributed to the fact that the cracks propagate along the top and bottom interfaces as the stamp is being lifted off from the laminated layer. As such, the PDMS stamp absorbs the deformation due to lift-off.

The delamination of the stamp from the laminated layer, and the laminated layer from the substrate, during the lift-off process, becomes more interesting at the micron-scale, considering the voids that are produced as a results of the wrapping of the thin films around the nano- and micro-particles that are trapped between the substrates and laminated layers. Figure 4.10 presents the results of the interfacial fracture that occurs during the lift-off process.

For the lamination of both P3HT:PCBM and MEH:PPV layers, the initial energy release rate at the top interface was the maximum value. This decreased to zero, while the energy release rate at the bottom interface (that was initially at zero) increased, as the energy release rate at the top interface decreased. Meanwhile, the energy release rates of the top and bottom cracks decreased, as the length of the crack (void) created by particle increased.

Furthermore, Figure 4.10 shows the energy release rates (G_{void}) at the tips of the cracks, which were created by the trapped particles, increased with increasing size of the particle and the

length of the bottom interface edge crack. However, G_{void} is very small for small particle size even as the bottom crack length increases. This is an indication that the particles can weaken the adhesion of the interface of interest during lamination. It is, therefore, important to ensure surface cleaning using laser or ozone/UV surface cleaner prior to lamination, for improving interfacial contact and adhesion between the active layer and the substrate.

The success of lamination of the active layers, P3HT:PCBM and MEH:PPV, of the electronics can be predicted in form of the differential of the interfacial energy release rates of the edge cracks at the top and bottom interfaces. This is shown in Figures 4.11a and 4.11b, in which computed energy release rates are presented as a function of the normalized bottom crack length. In both cases (of the active layers), the differential energy release rates decreases with increasing normalized bottom crack length, while the increasing particle size increases the energy difference. For a critical measured value of the interfacial energy difference, we can predict the success of the lamination (as described in Section 4.2.3).

It is of interest to compare the computed crack driving forces with the adhesion energies [5, 10, 12] and interfacial fracture energies [13] reported previously for interfaces that are relevant to OLEDs and OPVs. These are summarized in Table 4.2. The results obtained by computations are comparable to those previously reported. In the case of the OLED, in which P3HT:PCBM film is laminated onto PEDOT:PSS-coated substrates using PDMS stamp, the measured interfacial energy along the bottom interface (PEDOT:PSS/MEH-PPV) is greater than the energy along the top interface (MEH-PPV/Stamp). The small value of the interfacial energy at the top interface is attributed to the hydrophobic nature of the PDMS stamp, which seems to be promising for successful lamination. The tendency of the cracks paths to remain at the interface

or deviate away from the interface can influence the magnitude of the computed interfacial energy, as well as the measured interfacial adhesion and fracture energies.

Similarly, in the case of OPV, the interfacial energy at the bottom interface (PEDOT:PSS/P3HT:PCBM) is more than the energy at the top interface (P3HT:PCBM/Stamp). The crack paths being remained at the interface or deviated can also be attributed to the variation in the magnitude of the computed energies and the measured interfacial adhesion and fracture energies. Hence, interfacial fracture should occur when the interfacial fracture toughness values and the adhesion energies are lower than the substrate critical energy release rates. However, the criteria for interfacial cracking versus substrate cracking also depend on mode mixity, as shown in the earlier work by Evans and co-workers [14-17] and Rahbar et al. [18]

Finally, it should be noted that interfacial cracks can kink in and out of interfaces, giving rise to patches of partial interfacial separation during material pull-off. This can occur when the mechanisms of micro-void nucleation around inclusions and interfacial impurities link with dominant interfacial cracks in ways that promote the extension of interfacial cracks into adjacent layers. In such cases, the crack can kink in-and-out of interfaces depending on the distribution of the inclusion/impurities that include the formation of voids that link up with the propagating cracks. This has been shown in earlier work by Rahbar et al. [18] using a combination of finite element simulations and experiments.

The kinking of cracks (in-and-out of interfaces) has also been discussed in prior work by Evans et al. [14, 16]. Their work suggests that the criteria for interfacial cracking depend on the crack driving forces, as well as the mode mixity. However, it did not consider the nano-scale

mechanisms of micro-void nucleation and growth, as observed in the experiments and models of Rahbar and co-worker [18]. Further work is clearly needed to include the effects of inclusion distributions microstructure-based models for the prediction of interfacial/substrate cracking and the kinking of cracks during layer pull-off processes.

4.4.5 Implication

The results presented above are very significant in the fabrication of cheap organic solar cells and organic light emitting devices. The results can be used as guidelines for fabrication design, which can help improve performance. The fabrication of OLEDs and OPV cells by lamination seems to overcome the rigorous procedures encounter using other methods. Furthermore, in multilayered OLEDs and OPV cells, the layers work function alignment is very important to improve transport of charges. Lamination is, therefore, a good candidate for improving contact in the multilayered structures of OLEDs and OPV cells. The application of pressure during lamination tends to improve interfacial contact but too much of the pressure may cause sink in and device damage. Finally, the results above provide guidelines for successful lamination of thin film structures for OLEDs and OPV cells. These guidelines are summarized in Table 4.3.

4.5 Conclusions

This chapter presents the results of a combined experimental and theoretical/computational study of the contact and interfacial processes associated with the lamination of organic electronic structures.

1. A combination of analytical and computational models is used to study the effects of pressure on the contacts around dust particles that are trapped between adjacent layers in model OLED and OPV structures. The studies show that the contact length ratios increase with increasing pressure. However, the application of pressure may also result in excessive sink-in of trapped particles, which may damage the devices.
2. The subsequent pull-off stage of lamination was considered as an interfacial fracture process. This was studied using computational models of interfacial crack driving forces. The models suggest that the onset of interfacial crack growth or fracture occurred when the crack driving forces were equal to the measured adhesion energies for the relevant interfaces.
3. The effects of pre-existing defects need to be considered in greater detail, if we are to predict the critical conditions for the kinking in-and-out of cracks from different interfaces. Such kinking in-and-out is thought to contribute to the partial interfacial separation that is observed during the pull-off stage of the lamination of selected OPV and OLED structures.

Table 4.1: Properties of the materials used in the modeling

Material	**Young's Modulus (GPa)**	**Poisson's Ratio**	**References**
Particle	70	0.3	[7]
P3HT:PCBM	6.02	0.35	[11]
MEH:PPV	11.5	0.3	[11]
PEDOT:PSS	1.56	0.3	[19]
Glass	69	0.3	[20]
PDMS	0.003	0.3	[17, 20]

Table 4.2: Interfacial Adhesion and Fracture Energies in OLEDs and OPV Cells

(a) Measured and Computed interfacial Energies

Interface	Measured Adhesion Energy (γ) (J/m^2)	Measured Fracture Energy (J/m^2)	Computed Energy (G) (J/m^2)
P3HT:PCBM/PEDOT:PSS (bottom)	2.6 [5]	1.6 [13]	1.57 (in this study)
MEH-PPV/PEDOT:PSS (bottom)	15 [10, 12]	-	2.42 (in this study)
P3HT:PCBM/PDMS (top)	-	-	0.75 (in this study)
MEH-PPV/PDMS (top)	0.028 [22]	-	0.36 (in this study)

(b) Interfacial Energy Ratios

Laminated Layer	Computed (G_{top}/G_{bottom})
P3HT:PCBM	0.478
MEH:PPV	0.149

Table 4.3: Summary of the guidelines for successful lamination of thin film structures of OLEDs and OPV cells

Void Length (µm)	**P3HT:PCBM**	**MEH-PPV**	**Result of Lamination**
2.0	$d_b/t_f \geq 20.0$	$d_b/t_f \geq 25.0$	Successful (unsuccessful otherwise)
5.0	$d_b/t_f \geq 24.5$	$d_b/t_f \geq 31.0$	Successful (unsuccessful otherwise)
9.0	$d_b/t_f \geq 25.0$	$d_b/t_f \geq 33.0$	Successful (unsuccessful otherwise)
12.0	$d_b/t_f \geq 32.0$	$d_b/t_f \geq 34.0$	Successful (unsuccessful otherwise)

4.5 References

[1] J-Y Lee, S. T. Connor, Y. Cui and P. Peumans, "Semitransparent Organic Photovoltaic Cells with Laminated Top Electrode", *Nano Letter* 10, 1276-1279 (2010).

[2] J. Huang, G. Li and Y. Yang, "A Semi-transparent Plastic Solar Cell Fabricated by a Lamination Process", *Adv. Mater*. 10, 415-419 (2008).

[3] T-F. Guo, S. Pyo, S-C Chang and Y. Yang, "High Performance Polymer Light-Emitting Diode Fabricated by a Low Temperature Lamination Process", *Adv. Funct. Mater.* 11, 339-343 (2001).

[4] T. Zyung, S. H. Kim, S-C. Lim, J. H. Lee, H. Y. Chu, J-K. Oh, "Novel Method for Combining Flexible Organic Light-Emitting Diodes with Organic Thin-Film Transistors", *Journal of the Korean Physical Society* 48, S111-S114 (2005).

[5] T. M. Tong, "Adhesion and interfacial fracture: From organic light emitting devices and photovoltaic cells to solar lanterns for developing regions," Ph.D. Thesis (Princeton University, 2012).

[6] R. F. M. Lange, Y. Luo, R. Polo and J. Zahnd, "The Lamination of (Multi) Crystalline and Thin Film Based Photovoltaic Modules," *Prog. Photovolt: Res. Appl.* (201), DOI:1-:1002/pip.993.

[7] W. O. Akande, Y. Cao, N. Yao and W. Soboyejo, "Adhesion and the Cold Welding of Gold-Silver Thin Films", *J. Appl. Phys.* 107, 043519 (2010).

[8] Y. Cao, C. Kim, S-R. Forrest and W. Soboyejo, "Effects of Dust Particles and Layers Properties on Organic Electronic Devices Fabricated by Stamping", *J. Appl. Phys*. 98, 033713 (2005).

[9] M. B. Tucker, D. R. Hines and T. Li, "A Quality Map of Transfer Printing", *J. Appl. Phys.* 106, 103504 (2009).

[10] D. Yu, O. K. Oyewole, D. Kwabi, T. Tong, V. C. Anye, J. Asare, E. Rwenyagila, A. Fashina, O. Akogwu, J. Du, and W. O. Soboyejo, "Adhesion in flexible organic and hybrid organic/inorganic light emitting device and solar cells," *J. Appl. Phys.* 116, 074506 (2014).

[11] J. Du, T. Tong, W. Akande, A. Tsakiridou, and W. Soboyejo, "Pressure Effects on the Lamination of Organic Light Emitting Devices," *J. Disp. Technol.* 9, 601–606 (2013).

[12] T. Tong, B. Babatope, S. Admassie, J. Meng, O. Akwogu, W. Akande and W. O. Soboyejo, "Adhesion in Organic Structures," *J. Appl. Phys*., **106**, 083708 (2009).

[13] S. R. Dupont, M. Oliver, F. C. Krebs and R. H. Dauskardt, "Interlayer adhesion in roll-to-roll processed flexible inverted polymer solar cells," *Solar Energy and Solar Cells* 97, 171 (2012).

[14] A.G. Evans, J.W. Hutchinson, "Effects of non-planarity on the mixed mode fracture of bimaterial interfaces," *Acta Metallurgica Et Materialia* 37 (3), 909–916 (1989).

[15] M.Y He, H. Cao, A.G. Evans, "Mixed-mode fracture: the four-point shear specimen," *Acta Metallurgica Et Materialia* 38 (5), 839–846 (1990).

[16] A. G. Evans, B. J. Dalgleish, M. He and J. W. Hutchinson, "On Crack Path Selection and Interface Fracture Energy in Bimaterial Systems," *Acta metal.* 37 (12), 3249-3254 (1989).

[17] N. Bowden, S. Brittain, A. G. Evans, J. W. Hutchinson and G. M. Whitesides, "Spontaneous Formation of Ordered Structures in Thin Films of Metals Supported on an Elastomeric Polymer," *Nature* 393, 146-149 (1998).

[18] N. Rahbar, Y. Yang and W. O. Soboyejo, "Mixed Mode Fracture of Dental Interfaces," *Materials Science and Engineering A* **488**, 381 (2008).

[19] D. Tahk, H. H. Lee, and D.-Y. Khang, Macromolecules **42**, 7079–7083 (2009).

[20] W. Soboyejo, "Mechanical Properties of Engineered Materials," (CRC, New York, 2003).

[21] A. Bietsch and B. Michel, "Conformal contact and pattern stability of stamps used for soft lithography," *J. Appl. Phys.* 88, 4310-4318 (2000).

[22] S.-H. Hur, D.-Y. Khang, C. Kocabas and John A. Rogers, "Nanotransfer printing by use of noncovalent surface forces: Applications to thin-film transistors that use single-walled carbon nanotube networks and semiconducting polymers," *Appl. Phys. Lett.* 85, 5730-5732 (2004).

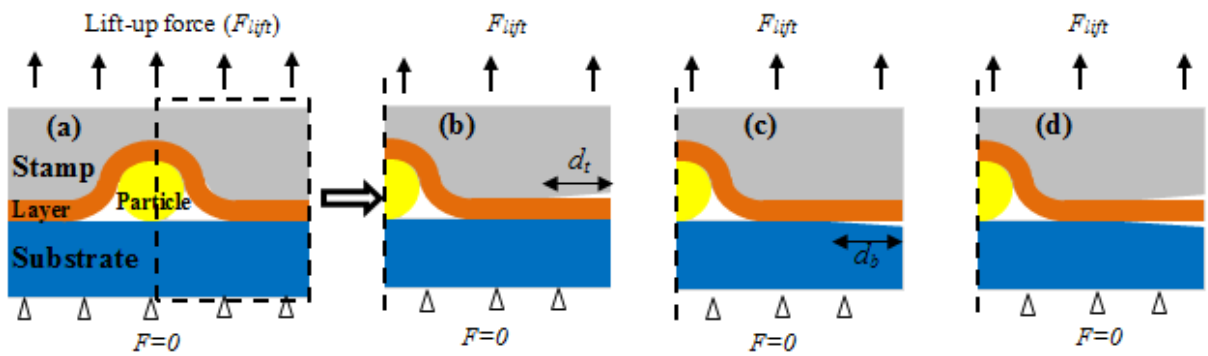

Figure 4.1: Schematics of micro scale models of interfacial fracture during the lift-off process of the lamination (a) model of the lift-off process after the press down of the layer on the substrate, (b) axisymmetric model of successful lift-off, (c) axisymmetric model of unsuccessful lift-off and (d) axisymmetric model of partial interfacial fracture.

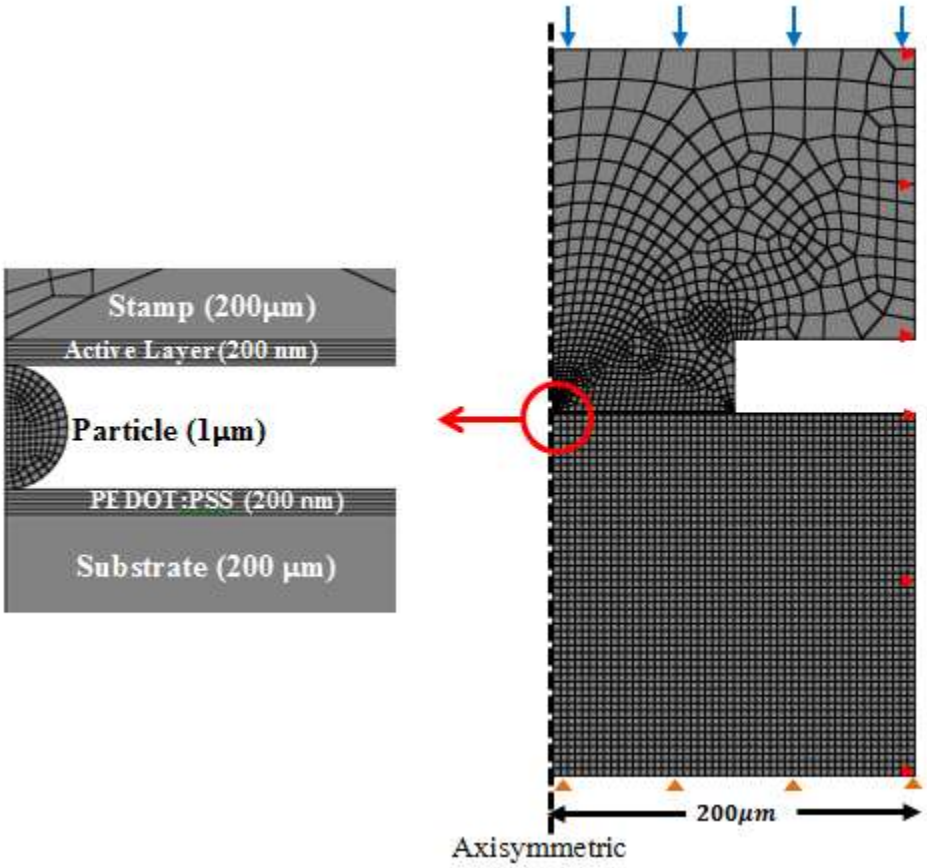

Figure 4.2: Geometry and mesh of finite element model of surface contact during pre-lamination of active layers of organic solar cells and light emitting devices

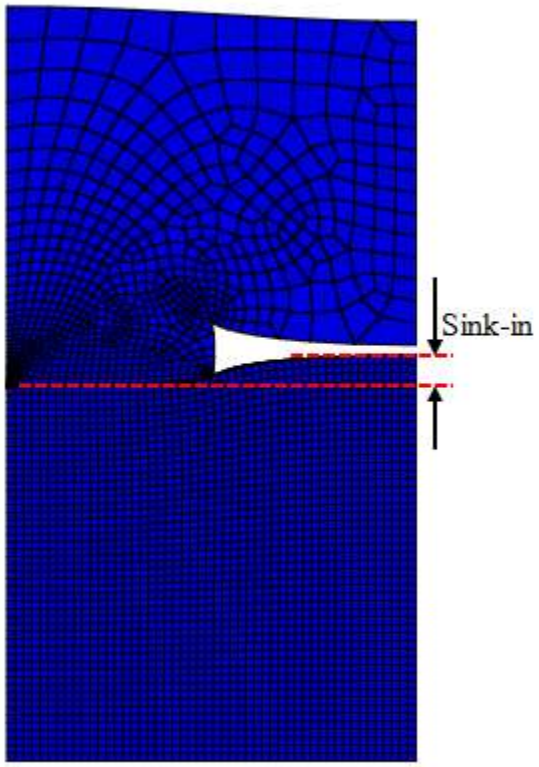

Figure 4.3: FEM of surface contact model after applying a range of forces (0 N – 500 N)

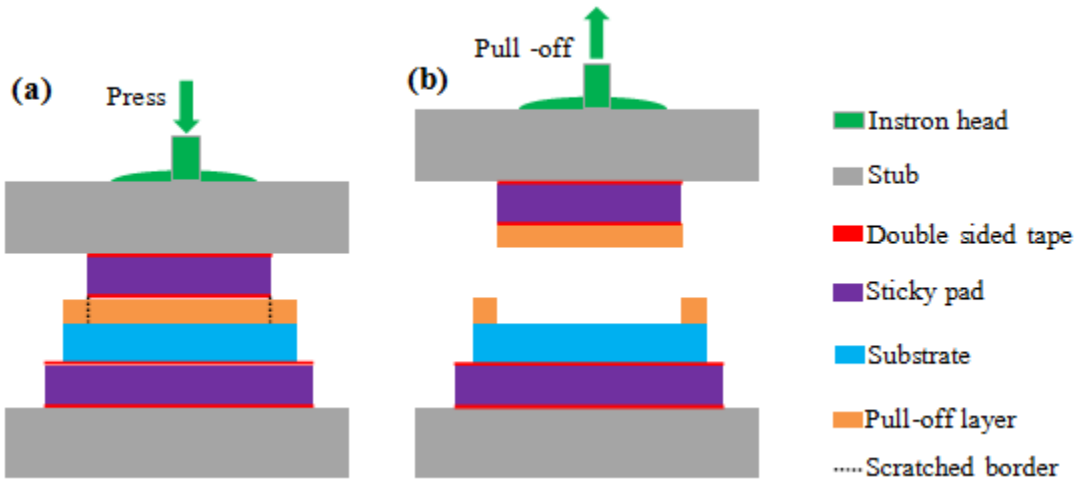

Figure 4.4: Schematic of experimental pull-off of spin-coated and laminated layer, showing the (a) press down process and (b) pull-off process

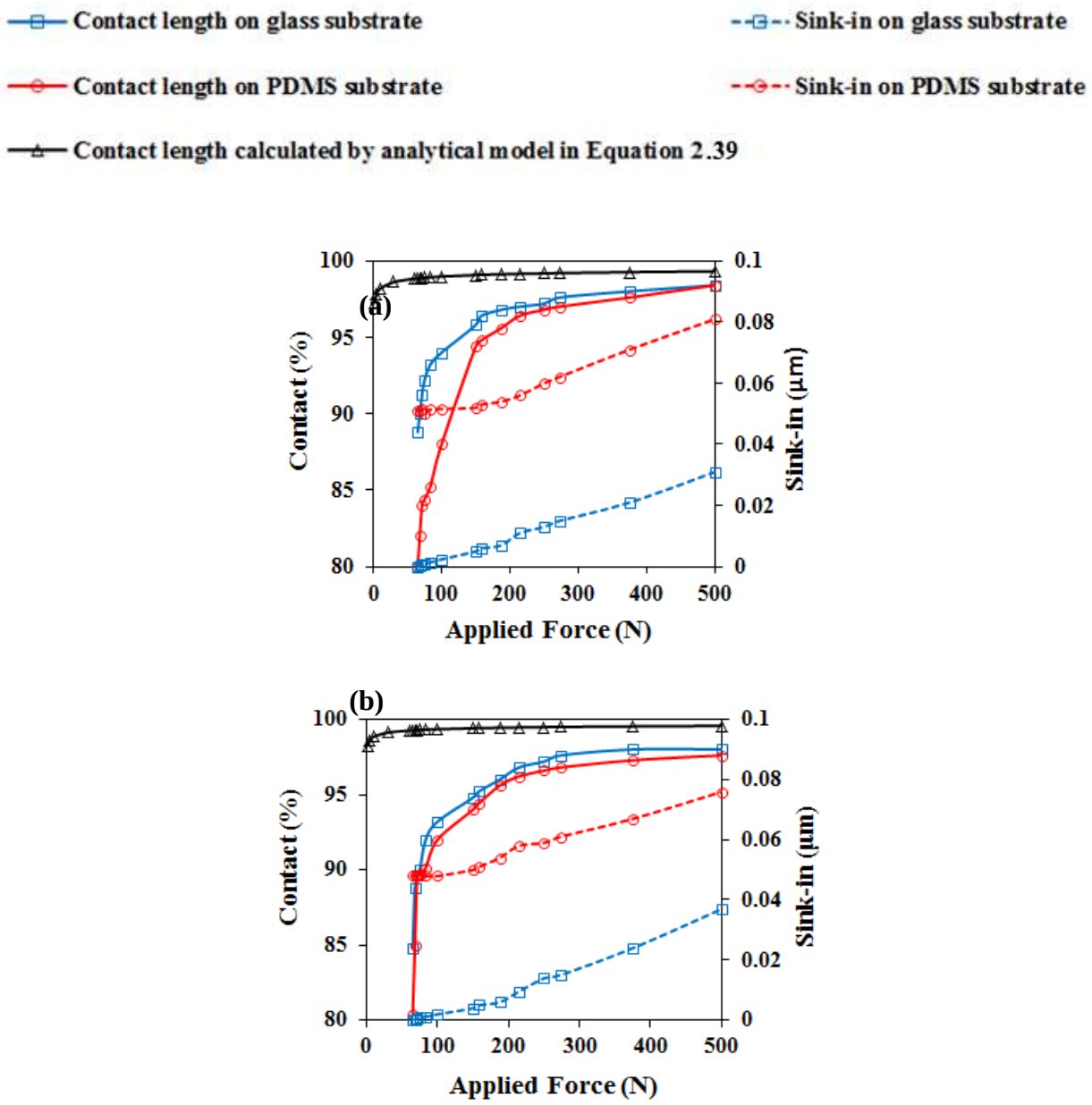

Figure 4.5: Effects of force on contact profiles of (a) P3HT:PCBM on PEDOT:PSS-coated substrate and (b) MEH-PPV on PEDOT:PSS-coated substrate.

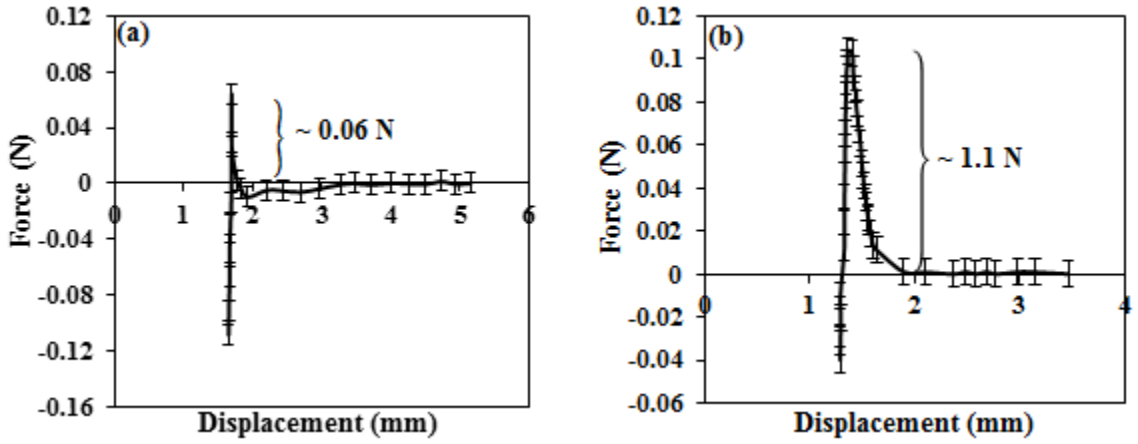

Figure 4.6: Force-displacement curve of pre-lamination of (a) P3HT:PCBM and (b) MEH-PPV on PEDOT:PPS-coated glass. The peaks represent the interfacial adhesion force during lift-off of the stamp from P3HT:PCBM and MEH-PPV

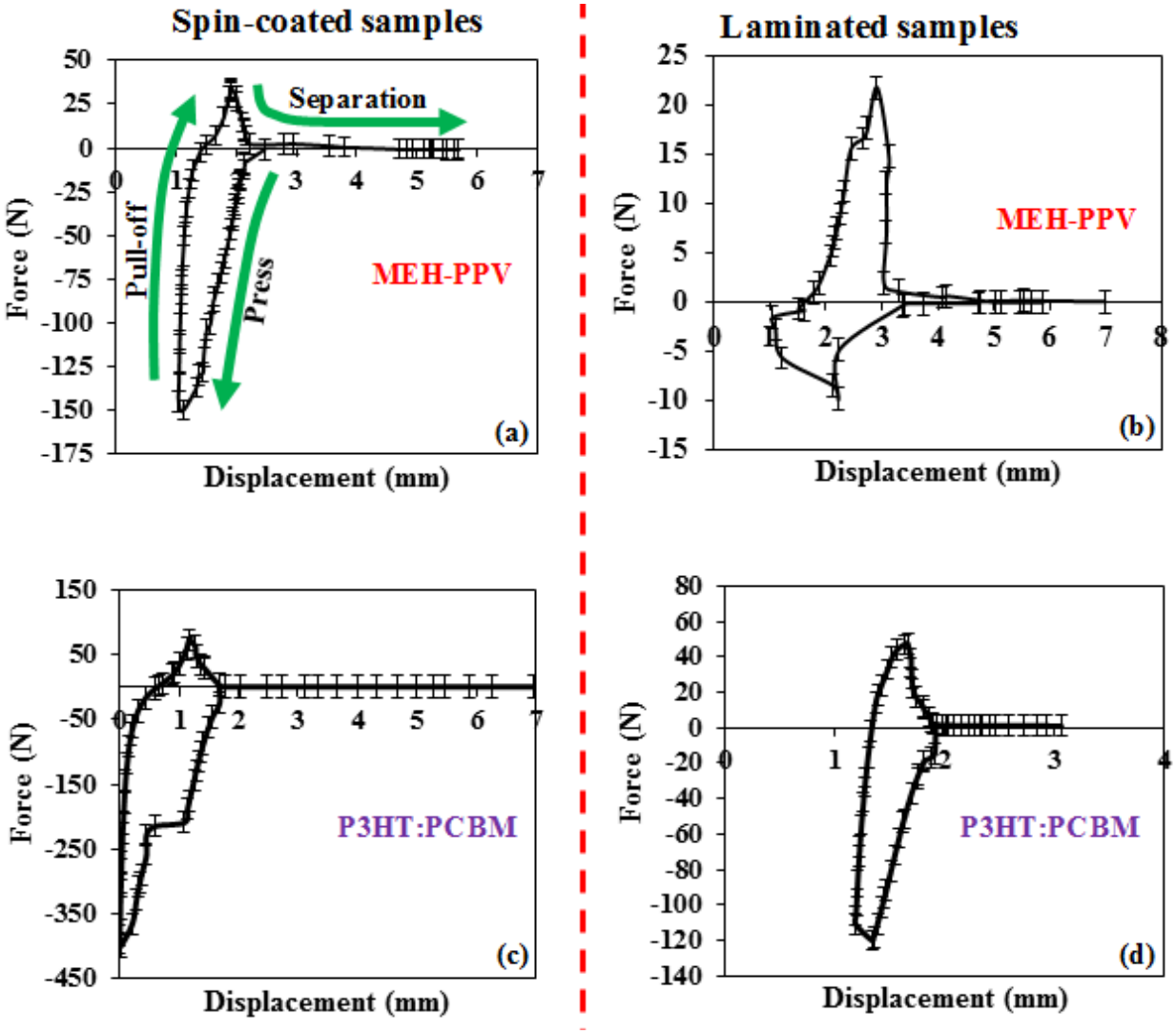

Figure 4.7: Force-displacement curves of pull-off of: (a) spin-coated MEH-PPV (b) spin-coated P3HT:PCBM (c) laminated MEH-PPV and (d) laminated P3HT:PCBM.

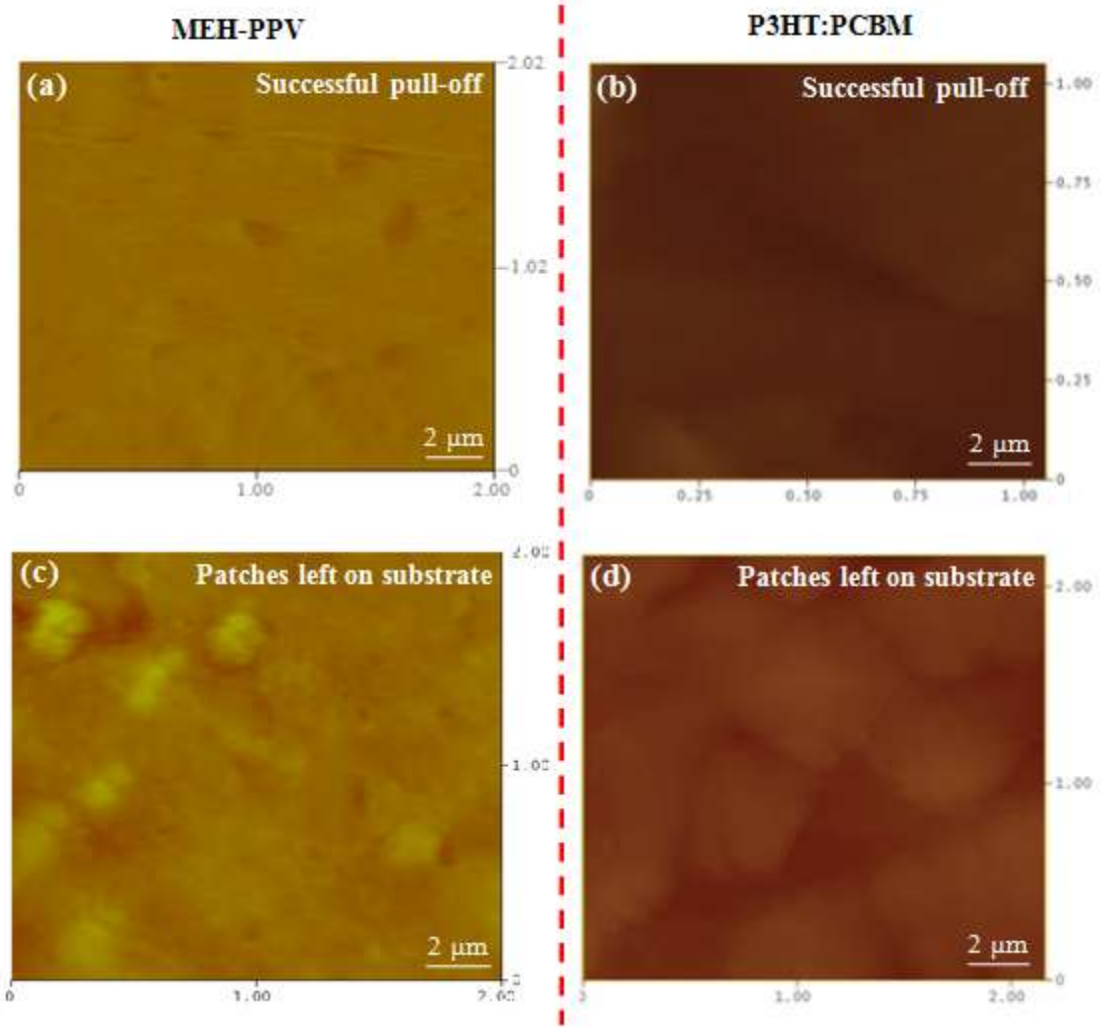

Figure 4.8: Samples of the AFM images of substrates after pull-off of active layers, MEH-PPV and P3HT:PCBM, for: (a and b) successful pull-off, (c and d) pull-off with remnants left on the substrates

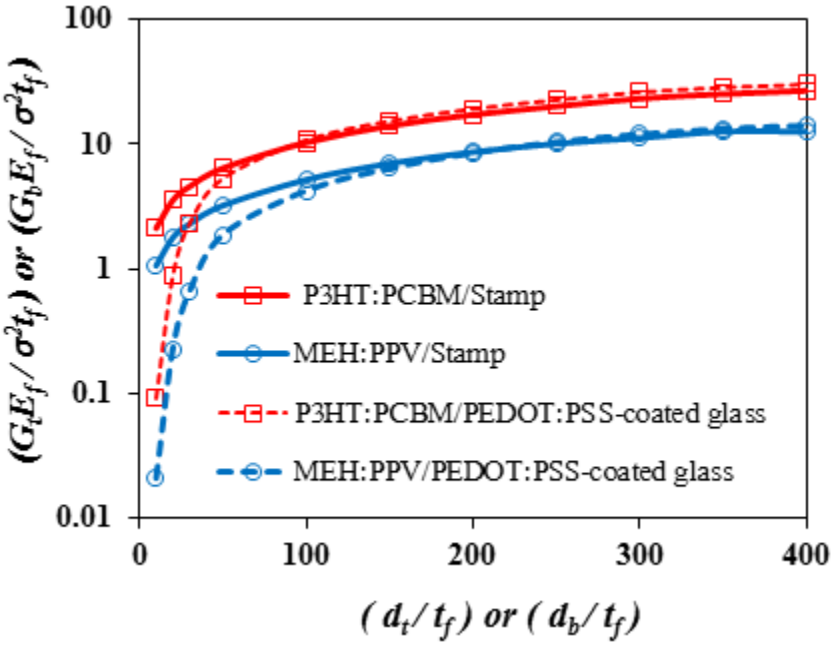

Figure 4.9: (Color online) The normalized top/bottom energy release rate as a function of the normalized top/bottom crack length, respectively. The energy release rates of the edge cracks at the top interfaces (P3HT:PCBM/Stamp and MEH:PPV/Stamp) were calculated with no edge crack at bottom interfaces (P3HT:PCBM/PEDOT:PSS-coated glass and MEH:PPV/PEDOT:PSS-coated glass). The energy release rates of the edge cracks at the bottom interfaces were also calculated with no edge crack at the top interfaces.

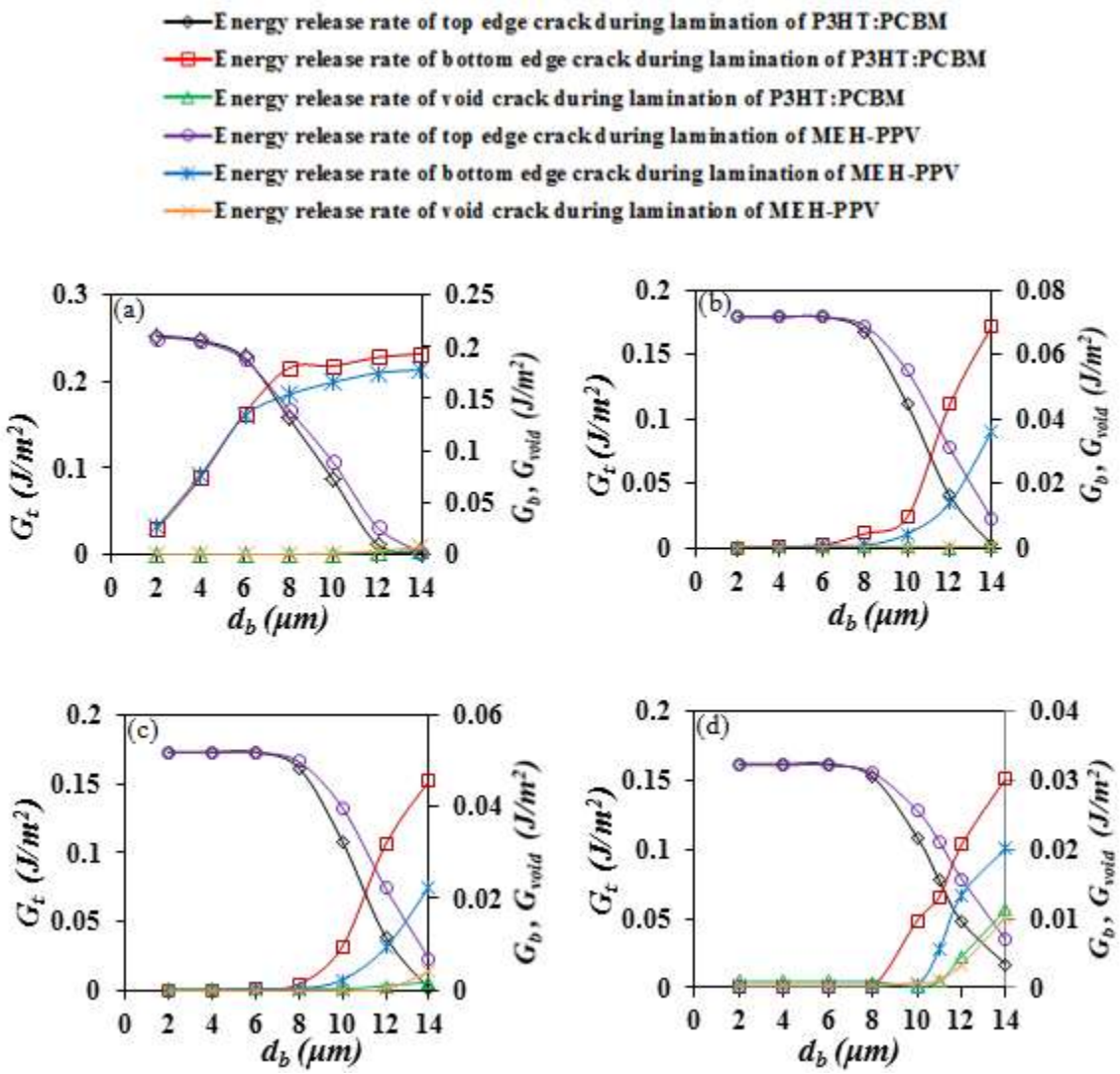

Figure 4.10: Interfacial fracture during lift-up of stamp from laminated of P3HT:PCBM and MEH:PPV on PEDOT:PSS-coated substrates for different particle diameters. (a)2 μm , (b) 6 μm, (c) 9 μm and (d) 12 μm. The concomitant energy release rates of the tips of the edge cracks at the top and bottom interfaces as functions of bottom crack length. Here, the length of the top edge crack is 6 μm, while the thickness of the active layers is maintained at 200 nm.

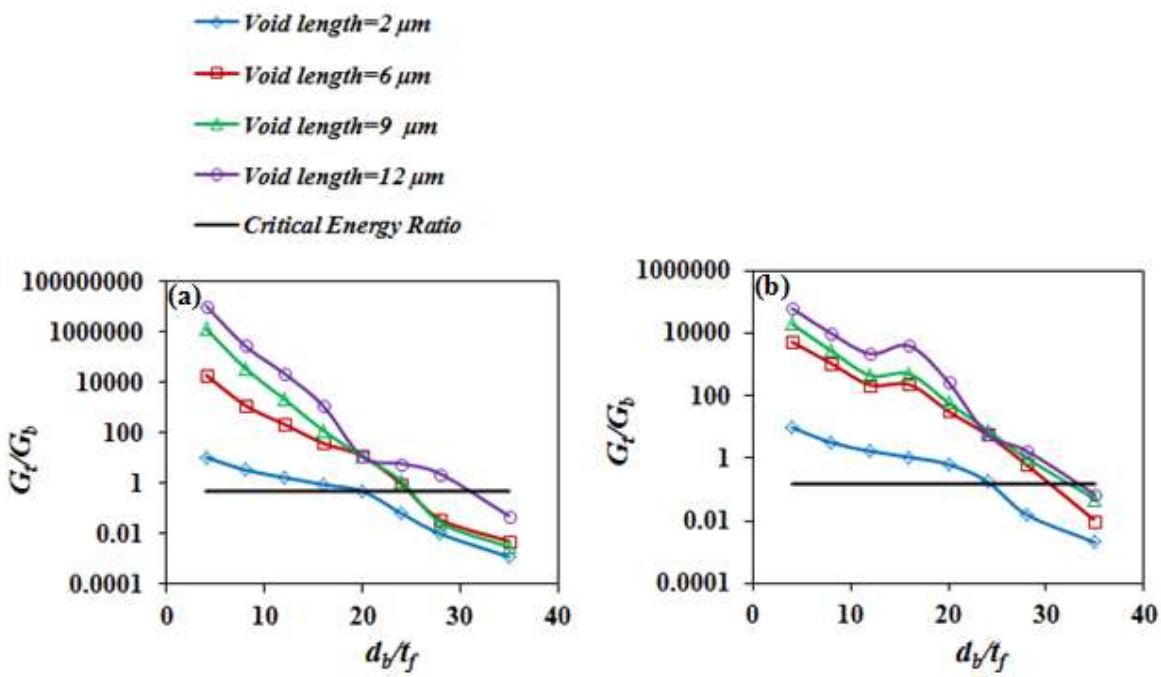

Figure 4.11: The ratio of the interfacial energy release rates (G_t/G_b) as a function of the normalized bottom crack length (d_b/t_f) for: (a) lamination of P3HT:PCBM and (b) lamination of MEH:PPV, showing the influence of the particle size. Here, the thickness of the active layers is $200\ nm$.

CHAPTER 5

MICRO-WRINKLING AND DELAMINATION-INDUCED BUCKLING OF STRETCHABLE ELECTRONIC STRUCTURES

5.1 Introduction

The occurrence of wrinkling and delamination-induced buckling in the combined measurement of film elastic properties and interfacial fracture toughness between thin metal films and elastomeric substrates is presented in this chapter. Analytical models are used to determine the critical stresses required for wrinkling and delamination-induced buckling in the structures. Interfacial fracture mechanics concepts are also used to determine the interfacial fracture toughness between the Au films and the PDMS substrates. The implications of the results are discussed for the design of stretchable electronics and biomedical devices.

The wrinkling and buckling deformations are used to create wavy, out of plane structures that can accommodate strain. This is done by pre-stretching the substrates [1-3] before the deposition of the films. The wrinkled and delamination-induced buckled structures of the films are formed due to thermal compressive residual [4,5-7] and pre-stretch [1-3] stresses.

The formation and deformation of wrinkling of thin films can initiate failure, which can lead to delamination [8] in layered structures of stretchable electronics.

The chapter is divided into 5 sections. Following the introduction in section 5.1, the theory and models are presented in section 5.2 before describing the experimental and computational methods in section 5.3. The results and discussion are then presented in section 5.4, before summarizing the salient conclusions in section 5.5.

5.2 Theory

This section presents the models that were used in this work. They include: (i) analytical models of the wrinkling and buckling of thin films on stretchable substrates, and (ii) interfacial fracture mechanics models of crack growth between layers. The theory of interfacial adhesion between two dissimilar materials has been described in chapter 2.

5.2.1 Residual and Applied Stresses

The controlled formation of wrinkles and buckles for applications in stretchable electronics involves the deposition of thin films onto pre-stretched substrates [1, 2, 9-12]. The film is subjected to stresses due to two factors. One is from the thermal expansion mismatch between the film and the substrate, while the other is from the pre-stretch of the substrate. These stresses are responsible for the induced wrinkling and buckling. The residual stress, σ_{th}, due to the thermal expansion coefficient mismatch is given by [13]:

$$\sigma_{th} = \left[E_f(\alpha_f - \alpha_s)(T_d - T)\right] / \left(1 - \nu_f\right) \tag{5.1}$$

where E_f and ν_f are Young's modulus and Poisson's ratio of the film; α_f and α_s are the respective thermal expansion coefficients of the film and the substrate; T_d is the deposition temperature, and T corresponds to the room temperature. The stress, σ_{app}, due to the release of the applied pre-stretched substrate can be approximated as:

$$\sigma_{app} = E_f \varepsilon_{pre} \tag{5.2}$$

where ε_{pre} corresponds to the pre-strain. By applying the principle of linear superposition, the total stress in the film can be obtained from the summation of Equations (5.1) and (5.2). This is given by:

$$\sigma_R = \sigma_{th} + \sigma_{app} = \left[E_f(\alpha_f - \alpha_s)(T_d - T)\right] / \left(1 - \nu_f\right) + E_f \varepsilon_{pre} \tag{5.3}$$

Equation (5.3) is the total stress that is responsible for wrinkling and delamination-induced buckling in the thin film deposited on a pre-stretched polymeric substrate.

5.2.2 Wrinkling and Buckling Models for Stretchable Electronics

As described above in Section. 5.2.1, wrinkled and buckled structures are formed as a result of the total stress on the film. The film starts wrinkling or buckling when the induced stress reaches a critical value. The solutions of the critical stress, σ_c, for the onset wrinkling or buckling of thin films are given by [2,6,7]:

$$\sigma_c = \left[E_f / \left(1 - \nu_f^2\right)\right]^{1/3} \left[3E_s / 8\left(1 - \nu_s^2\right)\right]^{2/3} \tag{5.4}$$

where E_f and E_s are the Young's moduli of the film and the substrate, ν_f and ν_s are the Poisson ratios of the film and the substrate. Also, the buckling of thin metallic films on stretchable elastic substrates has been modeled by Hutchinson and Suo [14]. The critical stress can be expressed as a function of wavelength of the buckling [13, 14]. This is given by:

$$\sigma_c = \pi^2 h^2 E_f / 3\lambda^2 \left(1 - \nu_f^2\right) \tag{5.5}$$

where λ is the wavelength of the buckle, E_f is the film Young's modulus, ν_f is the film Poisson's ratio, and h is the film thickness.

5.2.3 Interfacial Fracture Mechanics

In this section, interfacial failure is modeled at the onset of buckling of thin films on PDMS substrates. The theoretical expressions are presented for the energy release rates and the adhesion energies. It is assumed that films that are deposited on pre-stretched substrates can delaminate due to buckling [14], sandwiched particles and voids [15].

5.2.3.1 Analytical Modeling

The buckling of thin metallic films is often accompanied by the delamination of the films from the substrates. The buckle profiles can be analyzed using interfacial fracture mechanics. The energy release rate, G, of the interfacial crack is given by [14]:

$$G = \left[(1-\nu_f^2)h/(2E_f)\right](\sigma_R - \sigma_c)(\sigma_R + 3\sigma_c) \tag{5.6}$$

where E_f and ν_f are the Young's modulus and the Poisson's ratio of the Au film, h is the thickness of Au film, σ_R is the residual stress in the film and σ_c is the critical buckling stress. Ebata et al. [8] have shown that the residual stress increases with increasing amplitude of the buckling, as delamination proceeds. The thin film starts to delaminate from the substrate when the total stress (σ_R) is more than the critical stress (σ_c) for buckling. Hence, the interfacial energy release rate, G, increases with increasing σ_R and approaches its critical value, G_c, which is given by:

$$G_c = \left[\left(1-\nu_f^2\right)h/2E_f\right]\sigma_R^2 \tag{5.7}$$

However, the interfacial adhesion between two dissimilar materials involves interactions between atoms on the two surfaces to form secondary bonds. The true work of adhesion between the film and the substrate materials is given by [13, 16, 17]:

$$G_{adhesion} = G_{elastic} = \gamma_f + \gamma_s - \gamma_{f-s} \tag{5.8}$$

where γ_f and γ_s are the surface energies of the film and substrate separately, while γ_{f-s} is the surface energy between the film and the substrate in contact. If the bonds were broken mechanically, high interfacial fracture energies can be obtained due to the contributions from plastic deformation. However, if the contributions from plasticity are small, then the adhesion energy can be approximated as the interfacial fracture energy [16] between the two different materials.

From a fracture mechanics perspective, the measured adhesion energy, γ, corresponds to the critical mode I energy release rate [17]. This is possible because the fracture mechanics approach uses the applied strain energy release rate to measure the practical work of adhesion [16]. Hence, $G_c \approx \gamma$. The critical interfacial energy release rates can also be computed using commercial software packages such as ABAQUS^{TM}, which was used in this study (ABAQUS 6.12, Dassault Systèmes Incorporation, Rhoda Island). This involves introducing the geometry, materials properties and the boundary conditions of the bi-layered system into the software. In this case, the rate of the energy released at tip of the onset interfacial crack is denoted by G_{comp}.

5.3 Materials and Methods

5.3.1 Experimental Methods

5.3.1.1 Formation of Wrinkled and Micro-Buckled Au on PDMS Substrates

First, the PDMS substrate was prepared by mixing a Sylgard 184 silicone elastomer curing agent with a Sylgard 184 silicone elastomer base (Dow Corning Corporation, Midland MI) in a 1:10 weight ratio. Then, the mixture was processed under a vacuum pressure of 6 kPa for 30 minutes to remove all possible bubbles. The processed PDMS was poured into an aluminum mold with a dog-bone shape. This was followed by annealing in an oven at $80°C$ for 2 hours to form a 1mm thick PDMS substrate.

The PDMS was fixed with clamps at both ends and pre-strained to different levels (18%, 36% and 70%) on a hard steel substrate. A 5 nm thick of chromium (Cr) adhesive layer was then deposited onto the PDMS substrate using Denton evaporator (Denton DV 502A, Denton Vacuum, Moorestown, NJ). Chromium layer was used to improve the interfacial adhesion between the Au-film and the substrate. A gold thin film layer with a thickness of 100 nm was then deposited on top of the chromium layer. After deposition, the two ends of the PDMS substrate were released, and the wrinkle/buckle patterns were formed spontaneously in the gold thin films.

5.3.1.2 Atomic Force Microscopy (AFM) Adhesion Measurements

The interfacial adhesion in the layered Au-Cr-PDMS structure was measured using AFM. First, etched silicon contact mode AFM tips were purchased from Veeco Instruments

Woodbury, NY. The AFM tips were then coated with Au and Cr separately, while Au was deposited on glass substrates using Denton evaporator (Denton DV 502A, Denton Vacuum, Moorestown, NJ). With these coated tips and substrates, the adhesion forces between Cr/PDMS (Cr-coated tip versus PDMS), Cr/Au (Cr-coated tip versus Au-coated glass) and Au/PDMS (Au-coated tip versus PDMS) interfaces were measured.

AFM measurements were performed in air over a temperature range of 22-25°C and a relative humidity range of 31-46%. The tests were carried out in a Bruker Instruments Dimension 3000 AFM (Bruker Instruments, Plainview, NY). About ten force-displacement curves were obtained for each interaction. The tip deflections were obtained from the curves. The spring constants of each of the tips were measured using the thermal tune method [18]. This was done using a Bruker Instruments Nanoscope IIIa AFM (Bruker Instruments, Plainview, NY). With the measurements of the tip deflections and the spring constants, the adhesion forces were finally obtained from Hooke's law (Equation 2.1).

Due to the high sensitivity of AFM measurements to surface roughness, the substrate roughnesses and the tip radii were measured for each interaction pair. The surface roughnesses were obtained by AFM in the tapping mode. About 10 height and phase images of each substrate were obtained. These were used to measure the root mean squared roughnesses. The tip radii were calculated (before and after measurement) from images obtained using a scanning electron microscope (Philips FEI XL30 FEG-SEM, Hillsboro, OR). The measurements of the surface roughness and the tip radii were used to calculate the adhesion energies from Equations (2.5) and (2.27).

5.3.2 Computational Methods

Computational methods were used to study the failure mechanisms in the thin films of Au on PDMS substrates due to wrinkling and buckling. These were used to provide insights into the experimental results. First, the stress distributions in the wrinkled Au-films were simulated using the ABAQUS^{TM} software package (ABAQUS 6.12, Dassault Systèmes Incoporation, Rhoda Island). The two ends of the Au-PDMS model were displaced (pre-strained) by 18%, 36% and 70% of the length of the structure. The modulus and Poisson ratio of the Au films were maintained at 61 GPa and 0.35 [19], respectively. However, the Young's modulus of the PDMS substrate depends on the fabrication curing conditions and the mixing ratio of base and curing agent of the Sylgard silicone elastomer [20]. Hence, in the finite element simulation, the modulus of the substrate was varied from 1 MPa to 100 MPa [19], with Poisson ratio of 0.3. This was done to provide insights into the effects of substrate Young's modulus on the wrinkling profile.

In the case of delamination-induced buckling, it was assumed that there were pre- existing interfacial cracks between the Au-film and PDMS substrates. These cracks can be attributed to imperfections, such as voids, bubbles or impurities that are present at the interfaces. The energy release rates at the tips of the cracks were computed in form of the path independent J-integral. These were determined as functions of crack length using the ABAQUS^{TM} software package for the three levels of pre-strains. Furthermore, for different interfacial crack lengths, the interfacial energy release rates were calculated as functions of the pre-strain.

Since the film thickness is very small compared to the thickness of the substrate, and the fact that the Young's modulus of the film is far greater than that of the substrate, fine mesh

were used to model the Au/PDMS interface (as shown in Figure 5.1). Four-node plane strain quadrilateral elements were used. All the materials properties that were used were assumed to exhibit isotropic behavior, while the active contact Au/PDMS interface was maintained at zero rotation.

5.4. Results and Discussion

5.4.1 Wrinkling Profile as a Function of Pre-Strain and Substrate Elastic Modulus

SEM images of the wrinkled profiles induced after the release of the pre-strained Au/PDMS samples are presented in Figures 5.2a-5.2c. The images show that the wavelengths of the wrinkled structure reduced from 9.7 μm, for a pre-strain of 18%, to 6.6 μm, for a pre-strain of 36%, and 3.0 μm, for a pre-strain of 70%. This is presented clearly in Figure 5.3. The wavelengths are, therefore, inversely related to the pre-strain values. Furthermore, some transverse cracking was observed in the Au films, especially after pre-straining to a level of 70% (Figure 5.3c). The reduction in the wavelengths is attributed to the effects of the propagating transverse cracks, due to increasing pre-strain.

The von Mises stress distributions in the Au/PDMS structure are presented in Figures 5.4a-5.4d. These show the dependence of substrate elastic modulus on stress distributions and profile amplitude. The increase in the elastic modulus of the substrate increases the concentration of stress in the wrinkled structure. Hence, the processing of stiffer PDMS substrates will increase the overall Mises stresses, as shown in Figures 5.4a-5.4d. Furthermore, the wrinkling profile became more well defined with increasing substrate

Young's modulus (Figures 5.4a-5.4d). However, there is a high possibility that failure would be induced by the higher Von Mises stresses in the Au/PDMS structures that have higher moduli. A balanced approach is, therefore, needed to obtain well defined wrinkled profiles without inducing failure.

5.4.2 Stress Analysis

5.4.2.1 Residual Stress

For the Au film deposited on a pre-stretched PDMS substrate, residual stresses were induced in the Au films due to the thermal expansion coefficient mismatch between the Au films and the PDMS substrate. The total stress in the Au films was also assumed to be the sum of the thermal mismatch stress and the stress due to pre-strained PDMS substrate. The average textured Young's modulus for the Au film has been obtained to be ~61 GPa (Ref. 19). The measured Young's modulus of the Au film was then incorporated into Equation (5.1), along with the temperature difference ($\Delta T = T_d - T = 292K$), the Poison ratio ($\nu_f = 0.35$) and thermal expansion coefficients of the Au-film ($\alpha_f = 1.4 \times 10^{-5} / K$) and substrate ($\alpha_s = 3.14 \times 10^{-4} / K$). These were used to estimate the residual stress due to thermal expansion mismatch to be ~ 0.583 GPa. The stress due to the pre-strained PDMS substrate (Table 5.1) was calculated using Equation (5.2). Hence, the sum of the two residual stresses (σ_R) was obtained using Equation (5.3) for different thicknesses of the Au film. These results are presented in Table 5.1. These show that the calculated total stress increase with increasing pre-strain of the PDMS substrate.

5.4.2.2 Critical Stresses

The calculated critical stresses obtained for different wavelengths are presented in Figure 5.5a. The critical stresses for the onset of wrinkling/buckling were estimated from the measured profiles (Figure 5.2) and Equation 5.5. The critical stress decreases with increasing wavelength and vice-versa. Therefore, the critical stress is inversely related to the wavelength of the buckling/wrinkling profile. The decrease in the critical stress is attributed to the increase in pre-strain, which increases transverse cracks observed in Figure 5.2. It is important to note that the transverse cracks can be attributed to the possible formation of a brittle silica-like layer in the near-surface region of the PDMS with the deposited Cr. However, in Figure 5.5b, the critical stress increases with increasing substrate Young's modulus. Figure 5.5b was obtained from Equation 5.4, for possible ranges (1-100 MPa) of PDMS Young's moduli. The limiting critical stress for the Au thin film on a specific stretchable substrate (of known modulus) can be predicted from Figure 5.5b. For example, in Figure 5.5b inset, the critical stresses of Au film on PDMS substrates with Young's moduli of 1 MPa and 4 MPa are approximately 0.024 GPa and 0.06 GPa, respectively.

5.4.3 Surface Roughness/Profile

The root-mean-squared (rms) roughnesses of the different layers in the Au-coated PDMS structures are presented in Table 5.2. The PDMS had an rms roughness of 0.7±0.1 nm, while the Cr-coated surface had an rms roughness of 9.9±2.2 nm. The Au film has an intermediate rms roughness of 3.4±0.5 nm. The AFM tip radii measured from the SEM tip images averaged ~ 250 *nm* (Figure 5.6). Both the surface roughnesses and the AFM tips radii were used for computation of adhesion energies. In the SEM images, there were no significant

changes observed in the AFM tips. The highest magnification SEM images did not reveal any evidence of cohesive failure in the adhesion force measurement. Therefore, we conclude that the measured AFM pull-off forces correspond to adhesive failure.

5.4.4 Interfacial Adhesion and Fracture Energies

5.4.4.1 Measured Adhesion Forces and Energies

Adhesion forces between different layers in the Au-coated PDMS structure (Figure 5.7a) are presented in Figure 5.7b. The highest adhesion force was obtained between the Cr (adhesion promoter layer) and PDMS. This had an average pull-off/adhesion force of 77±29.3 *nN*. The high adhesion in Cr/PDMS interface could be due to highly electropositive nature of Cr. It is easy for electrons to be donated from Cr to methyl groups in the side chains of PDMS and form the surface dipoles that increase the attraction. An intermediate adhesion force of 30±5.7 nN was obtained for the Cr-Au interaction, while the lowest adhesion was obtained for the PDMS-Au interaction.

In an effort to use the models described in Section 2 of Chapter 2, a non-dimensional parameter for the calculation of the adhesion energy was first found to be ~10^{-6} (which is <<0.1) [21-23]. The DMT model was then used to determine the adhesion energies. The measured rms roughness value of surface 1 and the radius value of the AFM tip (surface 2) were incorporated into Equation (2.5) to calculate the effective radius. The measured adhesion forces and the corresponding effective radii were then incorporated into Equation (2.27) to calculate the adhesion energies. The results of these calculations are presented in Figure 5.7c. Once again, the Cr interlayer exhibits the highest adhesion energy with the

PDMS substrate. However, due to the roughness of the Cr layer, the adhesion energies of the Cr-Au couples are now comparable to those between PDMS and Au.

5.4.4.2 Interfacial Fracture Energies

The calculated interfacial energies obtained for different pre-strain values are summarized in Table 5.3. The ratios of the energy release rates, G, and the critical energy release rates, G_c, obtained from Equations (5.6) and (5.7), are plotted along with the analytical solutions in Figure 5.8. The ratios increase to a peak before decreasing to a steady-state value of about 1.0. This is comparable to results from earlier work by Hutchinson and Suo [14].

The energy release rates were also computed using ABAQUS^{TM}. Figures 5.9a-5.9d show plots of energy release rate as a function of interfacial crack length. These are presented for buckled Au films of different thicknesses. The interfacial energy release rates decrease continuously with increasing crack length in the case of the 100 nm Au films (Figure 5.9a). However, turning points were observed for thinner 50 and 75 nm Au films (Figures 5.9b – 5.9d). In any case, steady state fracture toughness values were approached with increasing interfacial crack length. Also, the turning points corresponded to the onset of buckling, while the differences between the steady state energy release rate and the turning point energy release rate correspond to the interfacial energy for delamination due to buckling.

For example, the computed interfacial energy for delamination of a Au/PDMS structure with a typical thickness (50 nm) of the Au film is ~ 3 J/m^2 under pre-strain value of 36 % (Figure 5.9d). The von Mises stress distributions in the buckled Au films on PDMS substrates are presented in Figures 5.10a -5.10e. The amplitude of the buckled film increases with increasing interfacial crack length. It also suggests that interfacial crack growth can be used

to control the waviness of the buckled films prior to applications in stretchable electronics structures.

5.4.4.3 Comparison of Adhesion Energies and Energy Release Rates

The measured adhesion energies are comparable to the interfacial energy release rates obtained for PDMS-Au interfaces using both computational and analytical techniques. A comparison of the data is presented in Figure 5.11. Note that the measured adhesion energy of the PDMS-Cr interface was significantly greater than the corresponding calculated interfacial energies. This suggests that the interfaces with the lower interfacial fracture toughnesses dominated the delamination processes that occurred during the buckling of the films on the PDMS substrates.

5.4.4.4 Dependence of Interfacial Energy on Pre-Strain and Film Thickness

For different ratios of interfacial crack lengths to film thicknesses $(2a/h)$, the computed interfacial energy release rates are plotted as a function of pre-strain in Figure 5.12. In obtaining the ratios, the crack length was maintained constant, while the thickness of the film was varied. The energy release rates increase with increasing pre-strain. However, increasing pre-strain could also result in multiple interfacial cracks, which can cause reduction in the wavelength of the Au-PDMS surface profile. This explains the reduction in the wavelength of the wrinkled Au film observed in Figure 5.2 for increasing the pre-strain of the PDMS substrate. According to Figure 5.12, for a thick film ($2a/h = 5$), a small pre-strain (~ 20%)

will cause delamination due to buckling for a critical adhesion energy, $\gamma = 2.42\, J/m^2$. However, the interfacial energy release rate between a relatively thin film ($2a/h = 90$) and the PDMS substrate is maintained below the critical value at a pre-strain of ~ 70%.

5.4.5 Implications

The implications of the above results are quite significant. First, they suggest that a basic understanding of micro-wrinkle and buckle formation is useful in the design and fabrication of micro-scale features in opto-electronic and biomedical structures. In the case of opto-electronic structures, these may include diffraction gratings and electronic textiles, while potential biomedical applications may include implantable biomedical devices for sensing and drug delivery.

The ability to control the surface textures by micro-wrinkling and buckling may also provide biomedical electronic systems with the ability to integrate well with biological tissue. For example, prior work [24] has shown that micro-grooves with depths and spacings of ~10-20 μm can promote the contact guidance/alignment of biological cells in ways that can lead to reduced scar tissue formation and increased cell/surface integration [25]. There is, therefore, the potential to tailor future wrinkled and buckled structures that can facilitate cell/surface interactions and integration with biological tissue.

There are interests in the potential stretchable electronics which include solar cells and light emitting devices that require the design of robust systems that are stretchable without significant interfacial failure [2]. There is, therefore, a need to extend the strain-induced micro-wrinkling and buckling testing technique to a more general framework for the

measurement of thin film interfacial fracture toughness. These are clearly some of the challenges and opportunities for future work.

5.5. Summary and Concluding Remarks

This chapter presents evidence of micro-wrinkle and delamination-induced buckle formation in thin film structures consisting of nano-scale Au films coated onto the surfaces of stretchable PDMS substrates. The wavelengths of the micro-wrinkled and buckled profiles decrease with increasing pre-strain. The critical buckling stress also decreased with increasing wavelength of the profile. The pre-strain technique was used for the measurement of the interfacial fracture toughness between hard and soft materials. The measurements of interfacial fracture toughness obtained for Au films on PDMS substrates are comparable to AFM measurements of adhesion energy. The results suggest that pre-strain-controlled profiles can be considered for potential biomedical and optoelectronic applications.

Table 5.1: Residual stresses due to effects of thermal expansion coefficient mismatch and pre-strained PDMS substrate.

Pre-strain (%)	**Applied Stress σ_{app} (GPa)**	**Residual Stress σ_R (GPa)**
18	10.98	11.56
36	21.96	22.54
70	42.70	43.28

Table 5.2: Average surface roughness values

Surface	**Roughness (*nm*)**
PDMS on glass	0.7±0.1
Cr	9.9±2.2
Au	3.4±0.5

Table 5.3: Interfacial energy release rates obtained from analytical expressions for different pre-strains for cracks between Au films and PDMS substrates

Pre-strain $\boldsymbol{\varepsilon}$ (%)	G_c (J/m^2)	G (J/m^2)	σ_R/σ_c	G/G_c
18	2.64	2.71	75.7	1.02
36	2.64	2.79	34.6	1.06
70	1.92	2.20	12.2	1.14

5.6 References

[1] D-H. Kim, and J. A. Rogers, "Stretchable electronics: Materials strategies and devices," *Adv. Mater.* 20, 4887-4892 (2008).

[2] D-H. Kim, J. Xiao, J. Song, Y. Huang and J. A. Rogers, "Stretchable, Curvilinear Electronics Based on Inorganic Materials," *Adv. Mater.* 22, 2108-2124 (2010).

[3] C. M. Stafford, B. D. Vogt, C. Harrison, D. Julthongpiput and R. Huang, "Elastic moduli of ultrathin amorphous polymer films," *Macromolecules*, 39, 5095-5099 (2006).

[4] M. Watanabe, H. Shirai and T. Hirai, "Wrinkled polypyrrole electrode for electroactive polymer actuators," *J. Appl. Phys.* 92, 4631-4637 (2002).

[5] J. W. Hutchinson, "The role of nonlinear substrate elasticity in the wrinkling of thin films," *Phil. Trans. R. Soc. A* 371, 20120422 (2013).

[6] H. Mei and R. Huang, 13th International Conference on Fracture, Beijing, China, 1-9 (2013).

[7] M. Watanabe, "Wrinkles with a well-ordered checkerboard pattern, created using dip-coating," *Soft Matter* 8, 1563-1569 (2012).

[8] Y. Ebata, A. B. Croll and A. J. Crosby, "Wrinkles and Strain Localizations in Polymer Thin Films," *Soft Matter* 8, 9086-9091 (2012).

[9] S. P. Lacour, J. Jones, S. Wagner, T. Li and Z. Suo, "Electronic skin: architecture and component," *Proc. IEEE* 93, 1459-1467 (2005).

[10] T. Li, Z. G. Suo, S. P. Lacour and S. Wagner, " Compliant thin film patterns of stiff materials as platforms for stretchable electronics," *J. Mater. Res.* 20, 3274-3277 (2005).

[11] S. P. Lacour, J. Jones, Z. Suo and S. Wagner, "Design and performance of thin metal film interconnects for skin-like electronic circuits," *IEEE Electron Device Lett.* 25, 179-181 (2004).

[12] D. J. Lipomi, B. C. Tee, M. Vosgueritchian and Z. Bao, "Stretchable Organic Solar Cells," *Adv. Mater*. 23, 1771-1775 (2011).

[13] O. Akogwu, D. Kwabi, A. Munhutu, T. Tong, and W. O. Soboyejo, "Adhesion and cyclic stretching of Au thin film on poly(dimethyl-siloxane) for stretchable electronics," *J. Appl. Phys.* 108, 123509 (2010).

[14] J. Hutchinson and Z. Suo, "Mixed-mode cracking in layered materials," *Adv. Appl. Mech*. 29, 63-191 (1991).

[15] D. Y. Momodu, T. Tong, M. G. Zebaze Kana, A. V. Chioh and W. O. Soboyejo, "Adhesion and degradation of organic and hybrid organic-inorganic light-emitting devices," *J. Appl. Phys.* **115**, 084504 (2014).

[16] W. W. Gerberich and M. J. Cordill, "Physics of Adhesion," *Rep. Prog. Phys.* **69**, 2157-2203 (2006).

[17] T. Tong, B Babatope, S. Admassie, J. Meng, O. Akwogu, W. Akande and W. O. Soboyejo, "Adhesion in Organic Structures," *J. Appl. Phys.* 106, 083708 (2009).

[18] Veeco Instruments Inc., Improving the Accuracy of AFM Measurements, the Thermal Tune Solution, Bruker Corporation, Billerica, MA, (2005).

[19] O. Akogwu, D. Kwabi, S. Midturi, M. Eleruja, B. Babatope and W. O. Soboyejo, "Large strain deformation and cracking of nano0scale gold films on PDMS substrates," *Mater. Sci. Eng. B* 170, 32-40 (2010).

[20] I. D. Johnston, D. K. McCluskey, C. K. L. Tan and M. C. Tracey, "Mechanical characterization of bulk Sylgard 184 for microfluidics and microengineering," J. *Micromech. Microeng.* **24**, 035017 (2014).

[21] Y. Mao, W. L. Wang, D. Wei, E. Kaxiras and J. G. Sodroski, "Graphene structures at an extreme degree of buckling," *ACS Nano*. **5**, 1395-1400 (2011).

[22] H. Fei, H. Jiang and D-Y. Khang, "Nonsinusoidal Buckling of Thin Gold ... Substrates," *J. Vac. Sci. Technol. A* **27**, L9-L12 (2009).

[23] H. Jiang, D-Y. Khang, H. Fei, H. Kim, Y. Huang, J. Xiao and John A. Rogers, "Finite width effect of thin-films buckling on compliant substrate: experimental and theoretical studies," *J. Mech. Phys. Solids* **56**, 2585-2598 (2008).

[24] J. Chen, S. Mwenifumbo, C. Langhammer, J-P. McGovern, M. Li, A. Beye, W. O. Soboyejo, "Cell/surface interactions and adhesion on Ti-6Al-4V: effects of surface texture," *J Biomed Mater. Res. B Appl. Biomater*. 82, 360-373 (2007).

[25] A. Gottschalk and W. R. Schafer, "Visualization of integral and peripheral cell surface proteins in live *Caenorhabditis* elegans," *J. Neurosci. Meth.* 154, 68-79 (2006).

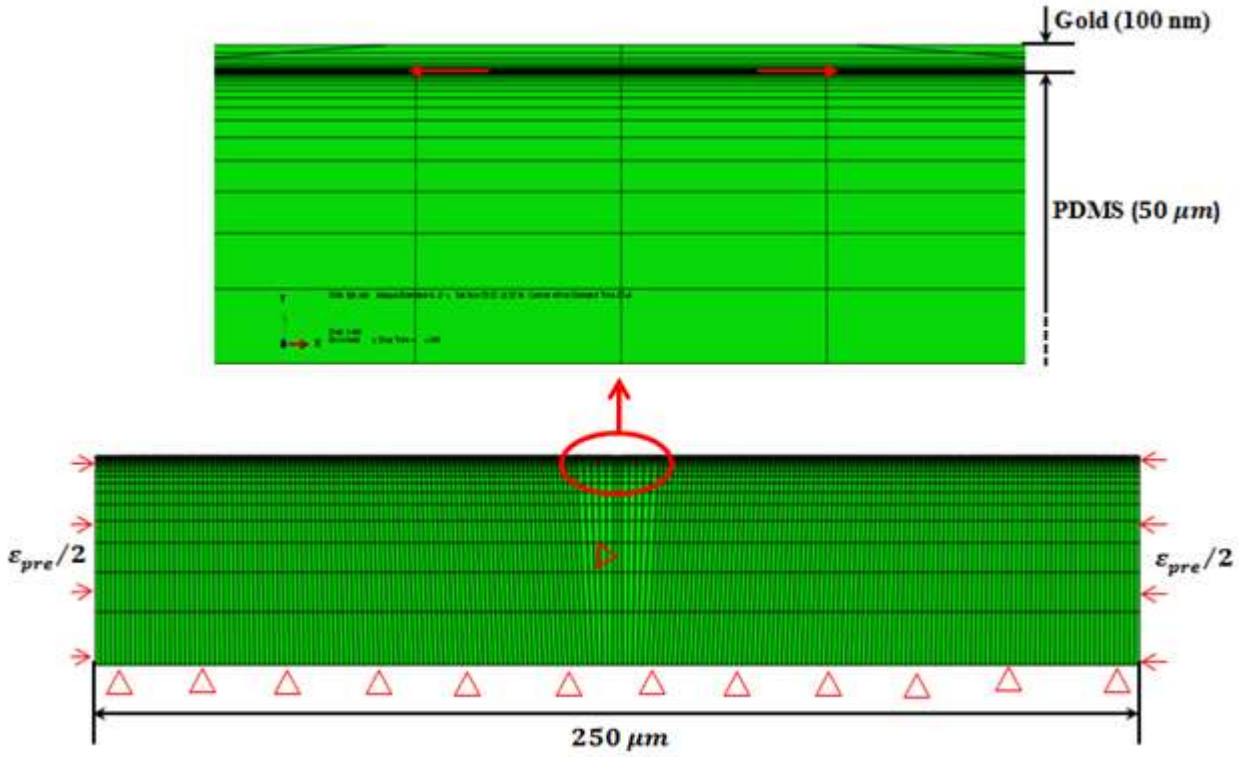

Figure 5.1: Finite element model of buckling of thin gold film on PDMS substrate

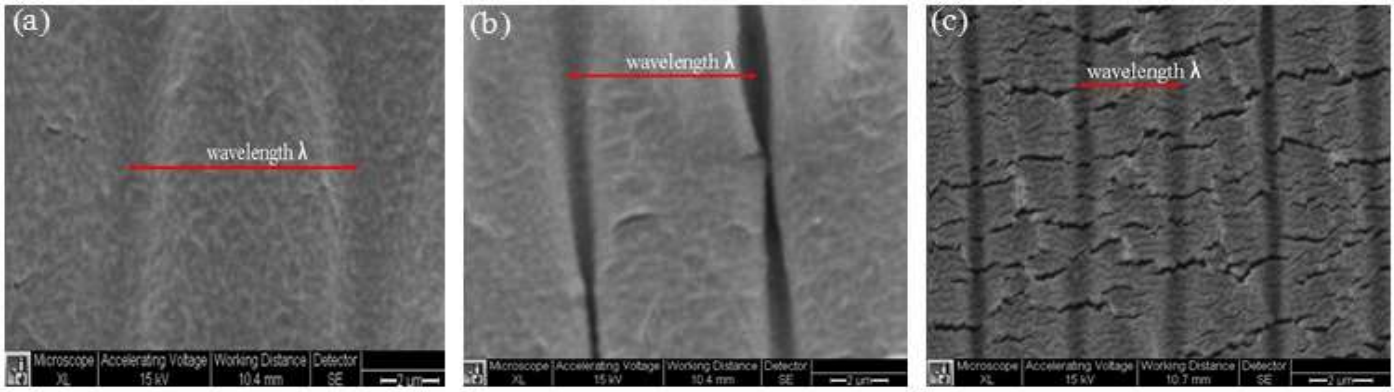

Figure 5.2: Micro-wrinkle profiles for different pre-strain value of: (a) 18%, (b) 36%, and (c) 70%.

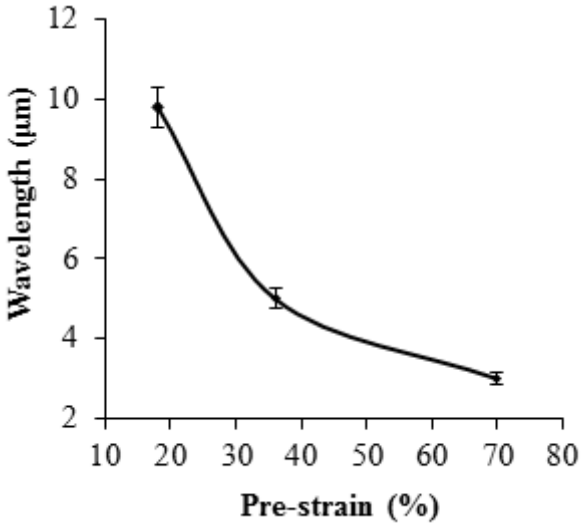

Figure 5.3: The wavelength of the profile versus pre-strain value of the PDMS substrate.

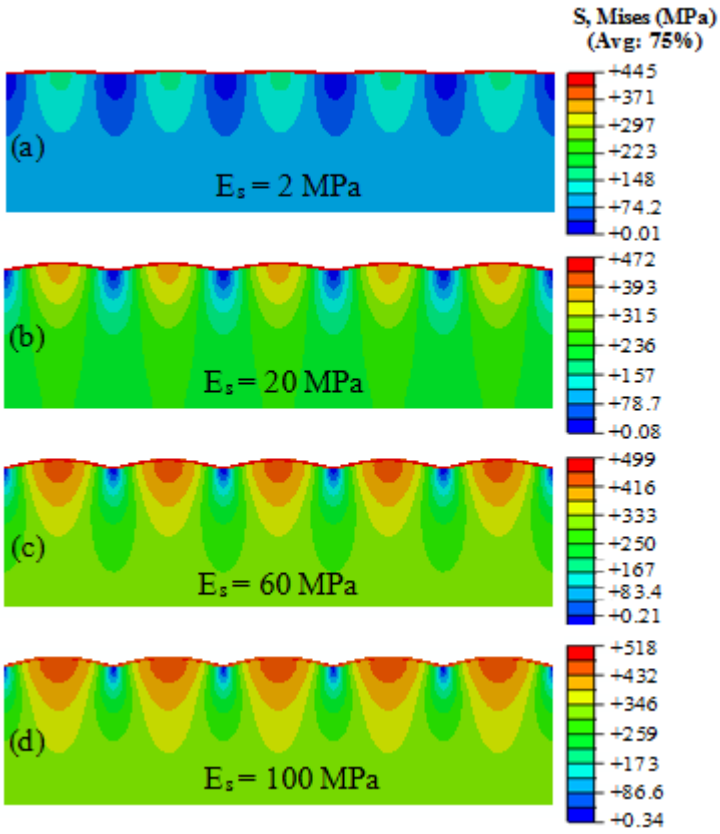

Figure 5.4: (Color online) Von Mises showing the dependence of elastic modulus of the substrate on wrinkle profile of Au film on PDMS substrate at 36 % pre-strain

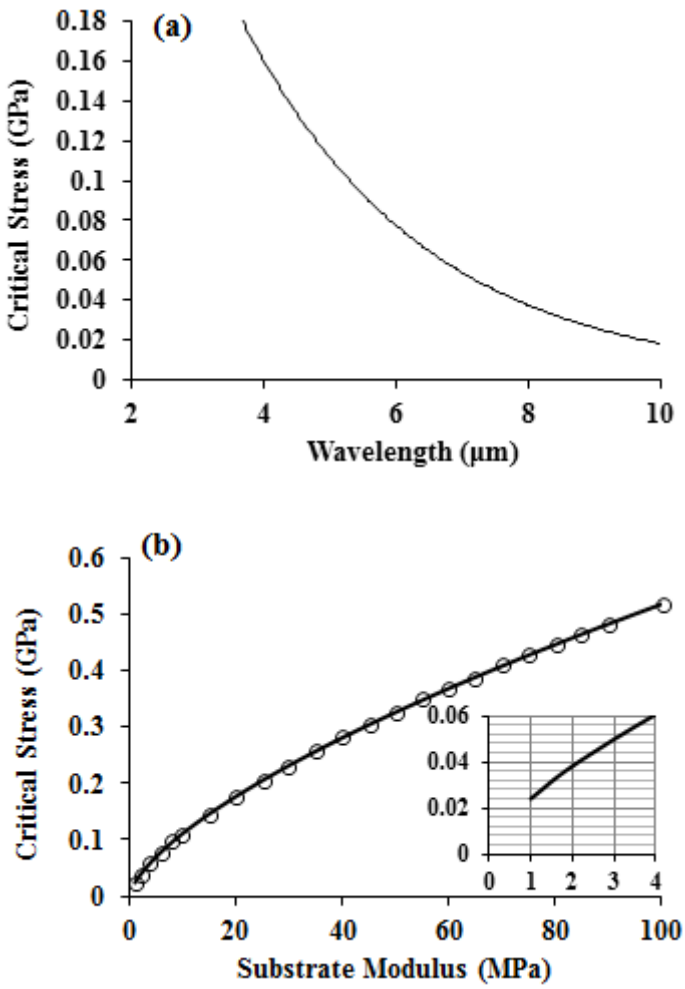

Figure 5.5: Dependence of (a) profile wavelength on critical stress (b) substrate modulus on critical stress.

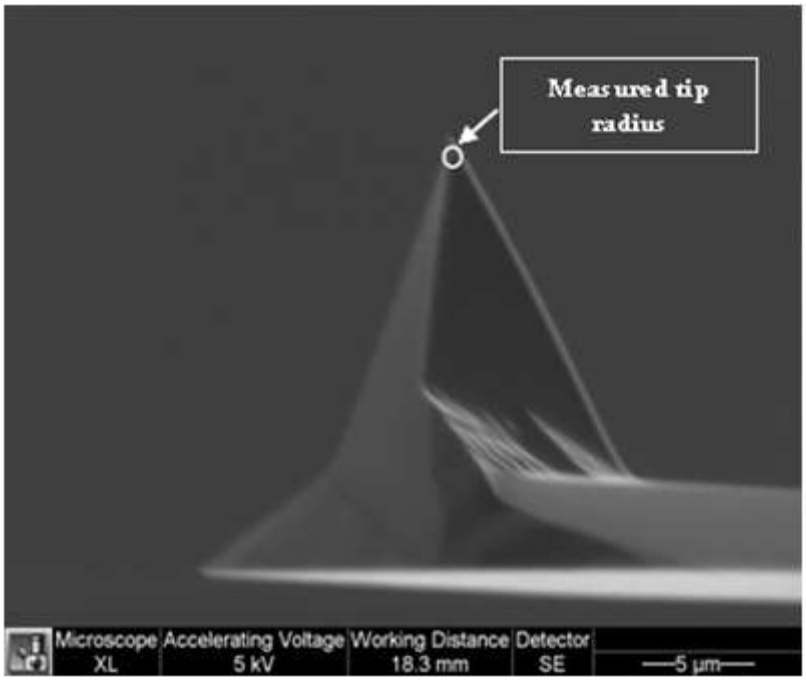

Figure 5.6: SEM image of AFM tip profile.

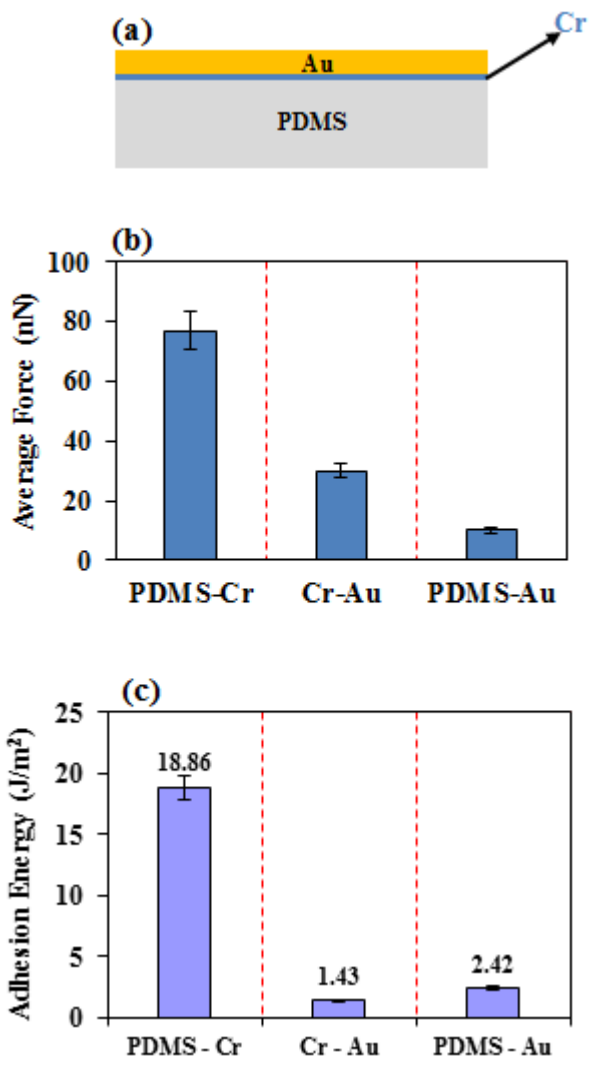

Figure 5.7: Interfacial adhesion in Au-coated PDMS structure (a) schematic of Au-coated PDMS structure with Cr interlayer (b) average of the measured AFM adhesion forces (c) measured AFM adhesion energies.

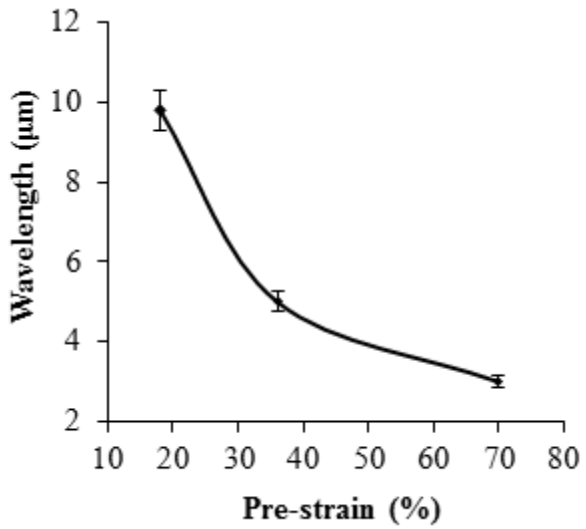

Figure 5.8: Plot of G/G_c versus σ_R/σ_c .

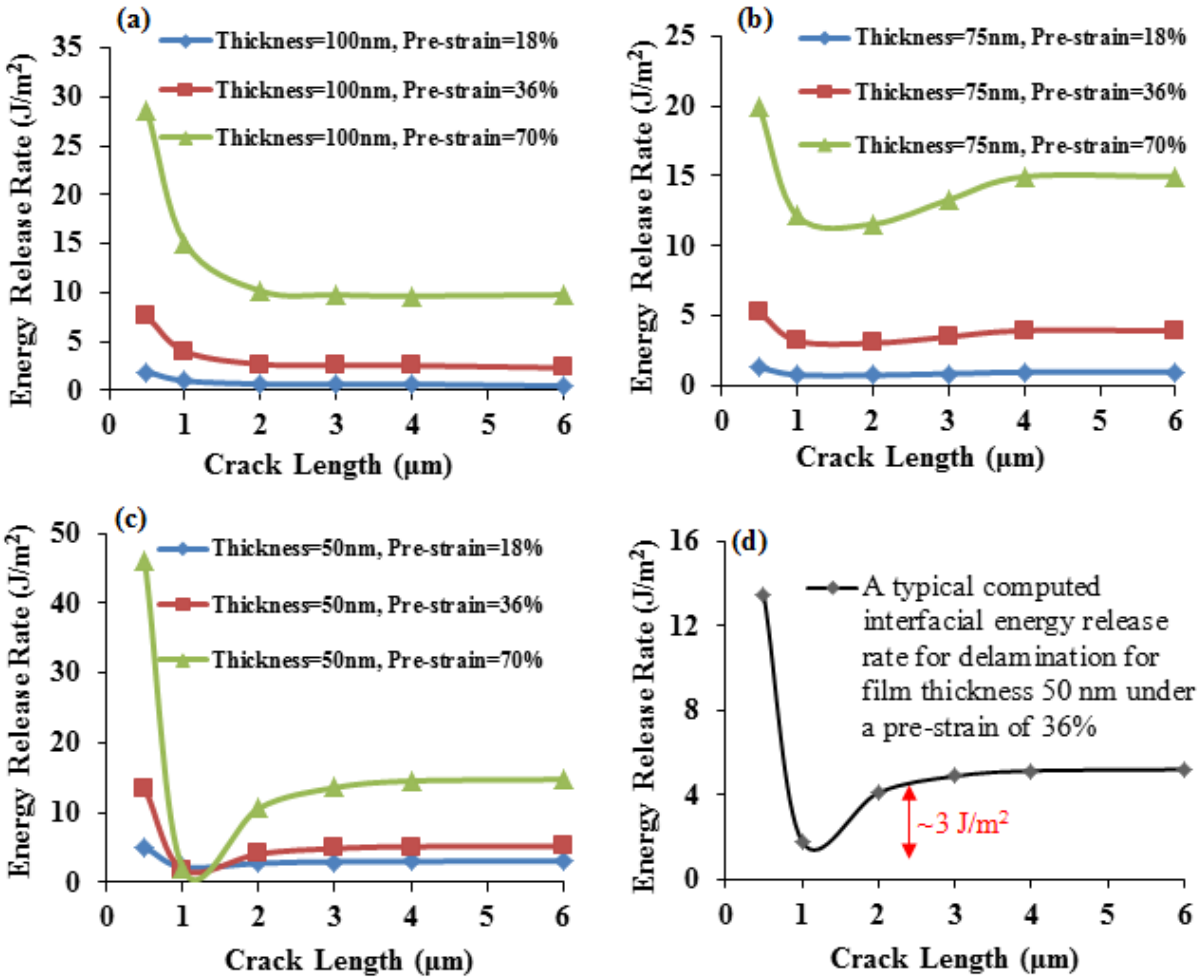

Figure 5.9: Interfacial energy release rate (G_{comp}) versus interfacial crack length. (a) 100 nm thick Au films on PDMS substrates; (b) 75 nm thick Au films on PDMS substrates; (c) 50 nesm thick films on PDMS substrates, and (d) 50 nm thick film with 36 % pre-strain and delamination

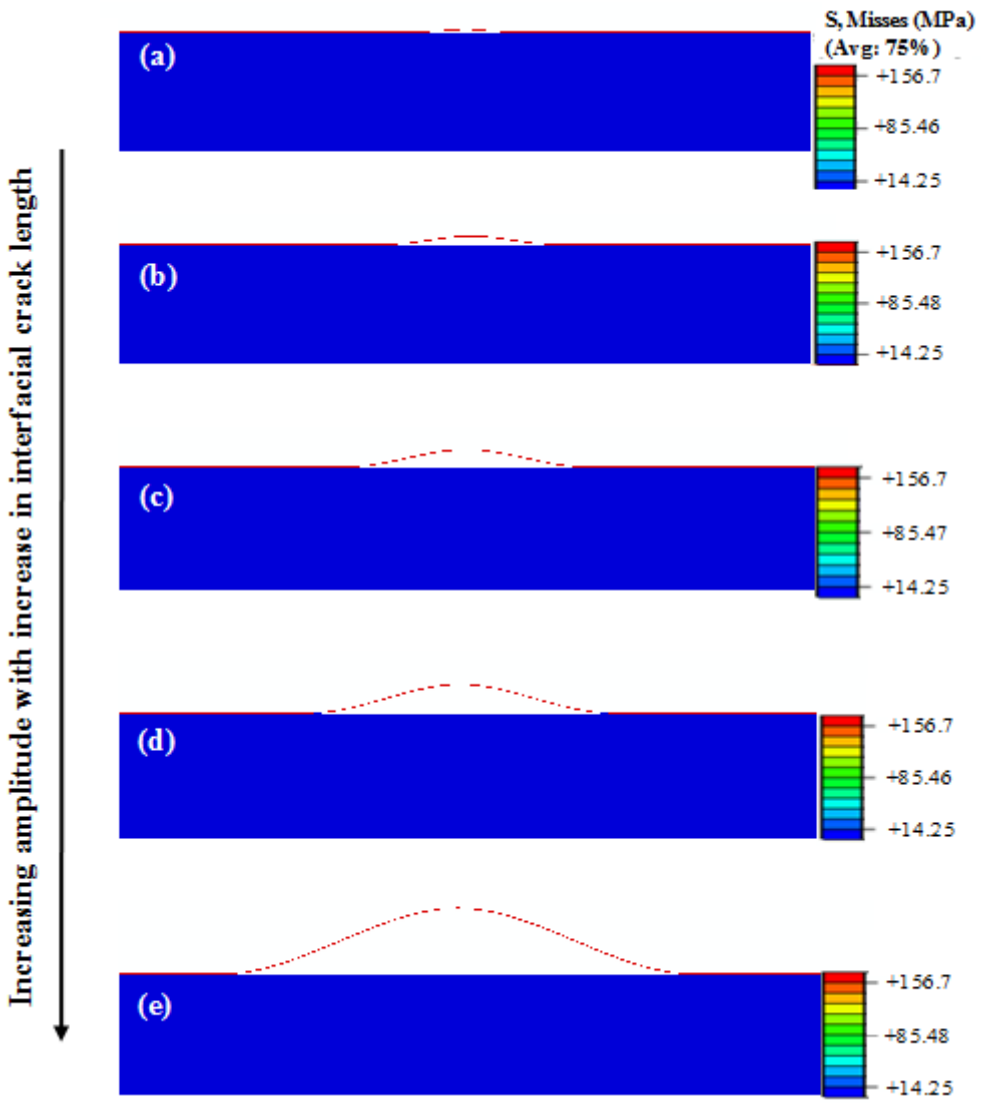

Figure 5.10: (Color online) Von Mises of delamination-induced buckled Au film. (a-e) the amplitude increases with increasing interfacial crack length.

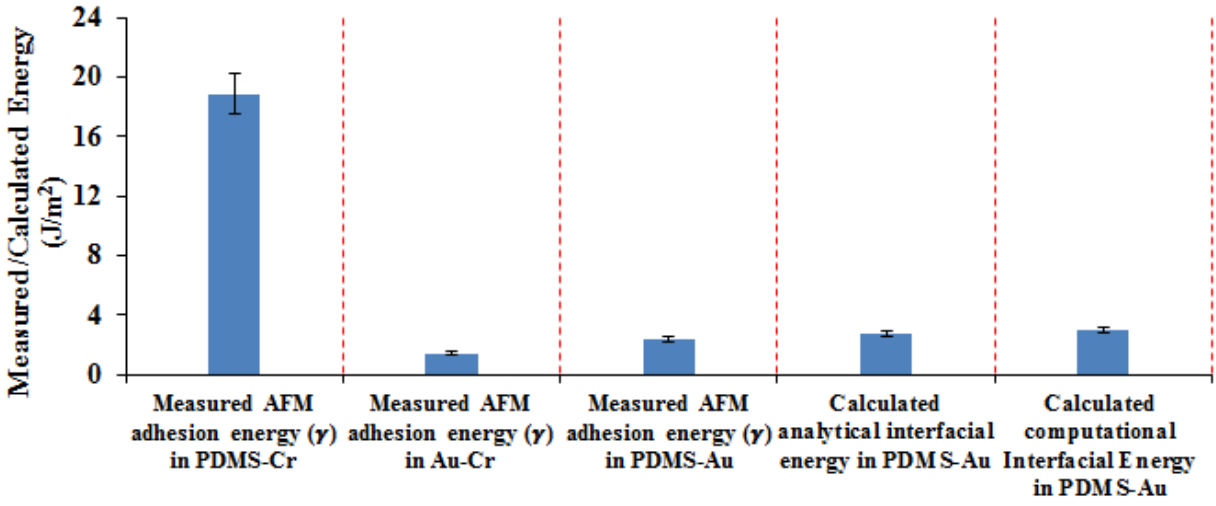

Figure 5.11: Comparison of measured AFM adhesion energies and calculated interfacial energy release rates

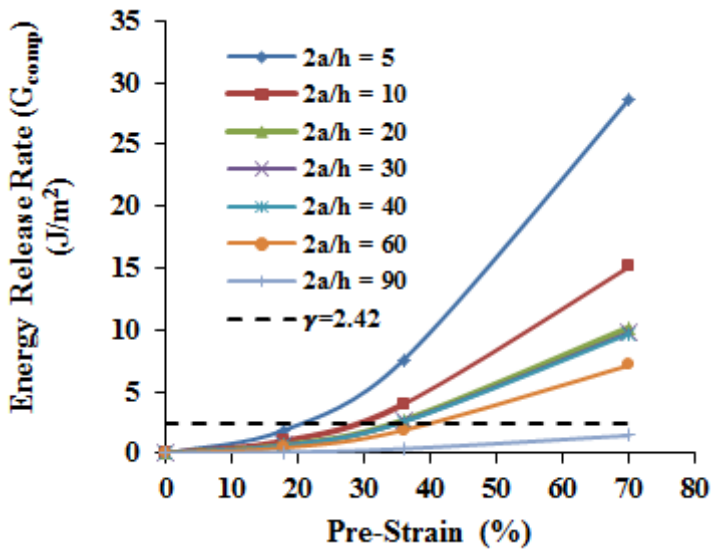

Figure 5.12: (Color online) Interfacial energy release rate (G_{comp}) versus pre-strain

CHAPTER 6

DEFORMATION AND FAILURE OF WRINKLED AND MICRO-BUCKLED STRETCHABLE ORGANIC SOLAR CELLS

6.1 Introduction

The degradation of stretchable organic solar cells can be understood when the mechanisms of the failure are studied. The guidelines for fabrication of stretchable organic solar cells can, therefore, improve the overall performance of the frontier stretchable organic solar cells. Considering the layers of organic solar cells deposited on a pre-stretched substrate (Figure 6.1a), wrinkling (Figure 6.1b) and buckle-driven delamination (Figures 6.1c and 6.1d) can occur when the pre-stretched substrate is released. If these structures (Figure 6.1a-6.1c) undergo repeated strain beyond the pre-strain, cracking can also occur [1, 2, 3-9]. The failure mechanisms may vary in layers and interfaces due to the interfacial energy differences, pre-strain level and thermal mismatch.

In this chapter, a combined experimental, analytical and computational technique is used to study the effects of stretching on failure mechanisms of layered structures of stretchable organic solar cells. First, the interfacial fracture energies of the layered stretchable organic solar cells are elucidated using finite element simulations. The failure are then observed using *in-situ/ex-situ* imaging with electron microscopy.

The chapter is divided into five sections. The introduction is presented section 6.1, while the theory of the interfacial fracture mechanics is presented in section 6.2. This is followed by materials and methods in section 6.3. The results and discussion are then presented in section 6.4 before summarizing the salient conclusions in section 6.5.

6.2 Theory

6.2.1 Wrinkling and Buckling Models for Stretchable Organic Solar Cells

The wrinkled and buckled layers of stretchable solar cells are formed due to the compressive stress that arises when the pre-strained polymeric substrate is released. The structure starts wrinkling or buckling when the induced strain reaches a critical value. The solutions of the critical strain, ε_c, for the onset wrinkling or buckling of thin layers of the solar cells are given by [10-12]:

$$\varepsilon_c = \left[3E_s\left(1-\nu_f^2\right)/8E_f\left(1-\nu_s^2\right)\right]^{2/3} \tag{6.1}$$

where E_f and E_s are the Young's moduli of each the layers of solar cells and the substrates, ν_f and ν_s are the Poisson ratios of the layers and the substrates.

The amplitudes of the buckled/wrinkled solar cells can also be influenced by the substrate pre-strain levels. The amplitudes of wrinkled and buckled thin films have been shown to increase with increasing pre-strain [13-22]. The relationship between the pre-strain, $\varepsilon_{pre-strain}$, the critical strain and the amplitude of the layered thin films is given by:

$$\varepsilon_{pre-strain} = \varepsilon_c \left[1 + \left(\frac{A}{t_f} \right)^2 \right] \tag{6.2}$$

where A is the amplitude and t_f is the thickness of the film. The ratio of the amplitude to the film thickness $\left(A/t_f\right)$ can be referred to as normalized amplitude.

6.2.2 Delamination-Induced Buckling and Cracking of Thin Films

In the case of the buckling of the films due to pre-strained substrates, the layers of the device are buckled at the critical pre-strain (as described in section 6.2.1). The total strain experienced by the films can be greater than the critical strain condition for buckling, which can lead to delamination. The length of the crack created due to delamination of the films is the same as the length of the buckled films. The schematic of the buckled film is shown in Figure 6.2.

The interfacial energy release rates of the tips of the cracks due to delamination-induced buckling of the films can be calculated using Finite Element Modeling (FEM). The energy release rate, G_d, due to delamination of the film is a function of residual strains, ε, the thicknesses, t_f and t_s, of the films and substrates, the Young's moduli, E_f and E_s, of the films and substrates, respectively. This is given by:

$$G_d = f\left(d, \overline{E}_f, \overline{E}_s, t_f, t_s, \varepsilon\right) \tag{6.3}$$

where $\overline{E}_s = E/\left(1-\nu_s^2\right)$, $\overline{E}_f = E/\left(1-\nu_f^2\right)$ and d is the half of the length of the buckled film (as shown in Figure 6.2b).

Equation (6.3) can be written (as shown in Appendix A) as:

$$G_d = f\left(\frac{\overline{E}_s}{\overline{E}_f}, \frac{t_s}{t_f}, \frac{d}{t_f}\right)\overline{E}_f \varepsilon^2 t_f \tag{6.4}$$

The amplitude of the buckled films and the residual strain/stress can affect the magnitude of the interfacial energy release rate of the crack tip.

It is also important to understand the fracture mechanics of wrinkled/buckled thin films on elastomeric substrates subjected to tensile stretching (Figure 6.3). When the films are deposited on pre-strained substrates, they wrinkle (Figure 6.3a) or buckle (Figure 6.3b) after the release of the substrates. The wrinkling or buckling increases the stretchability of the films, since they must flattened by subsequent deformation, before the films undergo the normal deformation that is typically observed in flat unwrinkled/unbuckled films. However, as the stretching is increased,

there is a possibility of inducing interfacial failure at the weakest interfaces, when the energy release rate exceeds the interfacial fracture toughness

6.3. Materials and Methods

6.3.1 Experimental Procedures

6.3.1.1 Processing of Stretchable Organic Solar Cells

First, poly-di-methyl-siloxane (PDMS) was fabricated by mixing a Sylgard 184 silicone elastomer base with a Sylgard 184 silicone elastomer curing agent in a 10:1 weight ratio. The mixture was degassed in a vacuum oven of pressure 50 kPa for 60 minutes to remove the trapped bubbles. The degassed PDMS was poured into a glass mold with dimensions of $25mm \times 50mm \times 1mm$ and was then cured at 70°C temperature for 2 hours. These dimensions of the PDMS were chosen so that the substrate can sit on the stub of spin coating system.

The PDMS was pre-strained at 30 % strain and was clipped at both ends to a glass slides. The surface of the PDMS was cleaned for 25 minutes using UV/Ozone cleaner to reduce the presence of micro scale particles on the substrates. A mixture of PEDOT:PSS (PEDOT:PSS, H. C. Starck, Newton, MA, USA), Zonyl FS-300 fluorosurfactant (Zonyl, H. C. Starck, Newton, MA, USA) and dimethylsulfoxide (H. C. Starck, Newton, MA, USA) was prepared in ratio 94: 5: 1 by volume. The essence of Zonyl FS-300 fluoro-surfactant and dimethylsulfoxide is to increase the wettability of PEDOS:PSS on PDMS. The mixture was then spin coated onto the pre-strained

substrate at 1000 revolutions per minutes (rpm) for 60 seconds, making ~90 nm thickness. The spin-coated PEDOT:PSS film was then baked at 80°C for 5 minutes. A 100 nm-thick P3HT:PCBM thin film was deposited by spin coating at a speed of 1500 rpm for 60 seconds. The spin-coated P3HT:PCBM layer was baked at the same condition used for baking the spin-coated PEDOT:PSS. Finally, a 150 nm-thick layer of Al (99.99% pure) was thermally evaporated onto the P3HT:PCBM/PEDOT:PSS-coated PDMS substrates before releasing the layered structure from the clips. In another configuration, a 100 nm-thick ITO layer was sputtered onto the pre-strained PDMS using an Edwards Auto 306 Sputtering system (Edwards, Sussex, UK). Subsequently, PEDOT:PSS and P3HT:PCBM layers were deposited onto the ITO-coated PDMS using the same protocol before thermally deposited the thin film of aluminum.

6.3.1.2 Optical Transmittance Measurements

The optical transmittance of the layers was measured using an Avantes UV-VIS-NIR spectrophotometer (Avantes, BV, USA). First, the samples were clamped between the jaws of Vernier callipers in such a way that the samples can be stretched and their lengths can be measured on the scale of the Vernier callipers. Then, air was used as a control to ensure 100% transmittance before placing the clamped samples on the sample holder between a light source and a light detector. The light was focused on the samples through a quartz optical fiber sensor (AVASPEC, Avantes, BV, USA). The optical transmittance was taken as the layers were being stretched to different applied strains (ranging from 0 % to 70 %). All of the measurements were obtained at room-temperature (~27 – 32 ^{o}C).

6.3.2 Computational Modeling

In an effort to understand interfacial fracture in the layered stretchable solar cells, computational methods were used to study the interfacial fracture and effects of stretching on the interfacial energies. Axisymmetric models were developed using ABAQUS™ software package (ABAQUS 6.12, Dassault Systèmes Incoporation, Rhoda Island). First, pre-existing interfacial cracks of different lengths were idealized at the interfaces of different configurations of stretchable organic solar cells. The energy release rates at the tips of interfacial cracks were computed in form of the path independent J-integral as a function of the crack length.

The crack length was varied from $d = 0$ to $d = 200t_f$, while the corresponding energies at the tips of the were computed by keeping the compressive strain constant at 20%. All the materials properties used (Table 6.1) were assumed to exhibit isotropic behavior, while the active contact interfaces were maintained at zero rotation. Throughout the simulations, a four-node elemental mesh was used, while the elements were dense near the tips of the cracks. The energy-crack length curves were then used to compute the interfacial fracture energies using the steady-state condition, as described by Li and co-workers [23]. The length of the interfacial crack (the length of the crack at which the steady-state condition is satisfied) was then fixed to compute the interfacial energy release rates as a function of the applied strain (as shown in Figure 6.3). The applied strain was varied from 0 % to 20 %.

6.4 Results and Discussion

6.4.1 Effects of Stretching on Profiles of Layers

The SEM images (Figures 6.4-6.6) of the layers of stretchable solar cells show that both films of PEDOT:SS on PDMS substrate (Figure 6.4a) and P3HT:PCBM on PEDOT:PSS-coated PDMS (Figure 6.5a) wrinkled after the release of the pre-strained substrates. However, the layers of ITO films on PDMS substrates (Figure 6.6a) show evidence of wrinkling with significant cracking. The results suggest that ITO cannot be used for anodic layer of stretchable organic solar cells.

At this point, we shall refer to the wrinkled layers formed after the release of the pre-strained PDMS substrates as unstretched, while those that were deformed thereafter will be described as stretched layers. When the unstretched PEDOT:PSS was strained up to 25 % and released (Figure 6.4b), there was evidence of micro-cracking and delamination. Cracking becomes more evident when the films were stretched to 70 % strain (Figure 6.4c).

The SEM images of P3HT:PCBM layer on PEDOT:PSS-coated PDMS show cracking and delamination when stretched up to 25 % (Figure 6.5b) with spontaneous delamination and cracking when strained to 70 % (Figure 6.5c). In the case when the strain is applied to unstretched ITO/PDMS structure (Figure 6.7a), several transverse cracks were observed, leading to damage of the film profile (Figures 6.6b and 6.6c).

The amplitude of the wrinkled and buckled films of stretchable solar cells was also found to depend on the level of pre-strain. Figure 6.7 presents the amplitude of the films as a function of

pre-strain for devices without ITO (Figure 6.7a) and those with ITO (Figure 6.7b). In all the wrinkled/buckled films, the amplitude increases with increasing pre-strain. Radius of curvature of the films also reduces with increasing pre-strain. Furthermore, layers with higher elastic moduli, e.g. ITO layers, tend to crack at lower strain levels, due to the limited strains for failure (Figure 6.6).

6.4.2 Failure Mechanics

Figure 6.8 presents the computed interfacial energy release rates. These are plotted against crack length. The energy release rates decrease with increasing crack length, but remain steady as the length of the crack increases into the steady-state regime. Similar results have been reported by Li and co-workers [23] for layers of organic–inorganic multilayer permeation barriers in flexible electronic structures.

The steady-state interfacial energy release rate obtained for the interface between PDMS and PEDOT:PSS was about 0.25 J/m^2 (Figure 6.8a). This increased to about 20 J/m^2 for the interface between PDMS and ITO (Figure 6.8b), while the steady-state interfacial fracture energy between PEDOT:PSS and P3HT:PCBM was about 4.4 J/m^2 (Figure 6.8c).

It is of interest to compare the computed interfacial fracture energies with the measured adhesion energies presented in the earlier experimental work by Tong et al. [24]. The results show that the computed energy release rates are most likely to occur between the PDMS substrate and the PEDOT:PSS layer, which can be used both as an anode and a hole transmission

layer. Hence, stretchable organic solar cell structures can be designed by replacing brittle and stiff ITO layers with more compliant PEDOT:PSS layers with weak adhesion to the PDMS substrate. This has been shown clearly in prior work by other research groups [1, 2, 9]. The low interfacial fracture energy between PDMS and PEDOT:PSS is attributed to the hydrophobic nature of PEDOT:PSS.

Finally, the strain to the onset of interfacial damage can be predicted using the plots of energy release rate versus strain presented in Figure 6.9. Note that the interfacial energy release rate (due to the delamination of the films that occurs during stretchable) increases with increasing applied strain. Also, the critical interfacial fracture energies (dash lines) can be determined from the intersection of the computed energy release rates with the measured values of adhesion energy obtained from prior work [24, 25]. These intersections were used to predict the strain limits for the onset of interfacial fracture between the films and the substrates.

6.4.3 Effects of Stretching on Optical Properties PEDOT:PSS Anodic Layer

Since the performance of stretchable organic solar cells is partly dependent on the amount of light energy that is absorbed by the active layer through the transparent anodic electrode, it is of interest to study the changes in the optical transmittance of the layers (in stretchable organic solar cells with increasing strain that can give rise to interfacial failure). The measured optical transmittance spectra obtained for anodic PEDOT:PSS layer (before and during stretching) are presented in Figure 6.10. These show that the transmittance decreases with increasing applied

strain. The degradation of the transmittance is associated with the failure mechanisms (layer and interfacial cracking) presented earlier (Figures 6.4a - 6.4c). This suggests that the transmission of light, through the layers and interfaces, is hindered by formation of microcracks and interfacial cracks that form during film stretching. Since such cracks can scatter light, the formation and growth of cracks can reduce the transmittance of light across layers and interfaces in the bulk heterojunction solar cell structures.

6.4.4 Failure Mechanisms of Stretchable Organic Solar Cells

It is important to relate the results obtained from the computational models (in this study) to prior reports of the current-voltage characteristics of deformed stretchable organic solar cells in the literature [2, 9, 25]. Current-voltage (I-V) curves obtained by Bao and co-workers have been presented in Ref.2 for stretchable organic solar cells without ITO anode layers. These are plotted in Figure 6.11 along with results obtained from the current study.

Figure 6.11 showed the degradation of a typical I-V curve of unstretched and stretched stretchable organic solar cells. The maximum power and the Fill Factor of the solar cells depend on the ability of the active layer to absorb light energy to generate hole-electron pairs that can be separated and collected at the electrodes. It is clear from Figure 6.11 that the unstretched solar cell is capable of performing better that when small and large strains are applied. However, at intermediate strains, the stretched pre-buckled/pre-wrinkled solar cells can perform better, presumably as a result of the flattening of the pre-buckles or pre-wrinkles during deformation.

The failure mechanisms observed in the layers of stretchable organic solar cells can, therefore, be used to improve performance and flexibility of devices. However, the reduction (Figure 6.10) in the transparency of the conducting PEDOT:PSS and/or ITO layers may ultimately limit the service lives of stretchable stretchable organic solar cells.

6.4.5 Implications

The implications of the current work are quite significant. First, they suggest that the deformation of stretchable solar cells may be enhanced by the controlled introduction of pre-buckles or pre-wrinkles that increase the stretchability of the solar cells during subsequent applications under tensile loading conditions. Such enhancement in stretchability may facilitate future applications in electronic textiles and solar roofing tiles, under a wide range of tensile stress states.

However, further work is needed to explore the long term performance of such structures. There is also a need to explore the sub-critical growth of interfacial and layer cracks under static, monotonic and cyclic loading conditions that can occur over a wide range of environmental conditions in service. The physics of such growth, which may occur under condition that give rise to creep, fatigue and/or environmentally-assisted crack growth, must be better understood for us to develop physics-based models for the life prediction of stretchable organic solar cells. These are clearly some of the challenges for future work.

Finally, it is important to note that the current work provides a framework for the modelling of the potential effects of pre-buckling or pre-wrinkling of layers that are relevant to organic solar cells. This includes: an analytical framework that can be used for the modelling of idealized bi-material pairs; a computational framework that can be used for the modelling of multilayers, and an experimental framework that can be used for model validation. In any case, the potential improvements in stretchability can be estimated from the additional strain to flattening of the pre-wrinkles or the pre-buckles. The conditions for device failure may also be determined from the simulated conditions for interfacial or layer failure.

Hence, the processing conditions should be controlled to limit the interfacial defects that can occur at the interfaces within stretchable organic solar cells. This is especially true for the weakest interfaces, such as those between PEDOT:PSS and PDMS in stretchable organic solar cells. Conversely, some interfacial failure is also needed to promote buckling-induced wrinkling, which may increase the stretchability of stretchable organic solar cells. This suggests a need for a balanced approach that involves the control of interfaces in the development of the next generation of stretchable organic solar cells.

6.5 Summary and Concluding Remarks

This paper presents the results of a combined analytical, computational and experimental study of the deformation of pre-wrinkled and pre-buckled organic solar cells. The deformation and cracking mechanisms were elucidated along with the effects of stretching on optical transmittance and current voltage characteristics.

The onset of interfacial cracking was shown to correspond to the condition at which the computed energy release rates were equal to prior measurements of adhesion energies of the weakest bi-material pairs within the multilayers in model organic solar cells. This suggests that the least adherent interfaces have a strong effect on the onset of micro-buckling in stretchable organic solar cells.

Since the micro-wrinkles and micro-buckles are flattened during the initial stages of deformation, micro-wrinkling and micro-buckling can be used to increase the effective deformability/stretchability of organic solar cells. However, excessive pre-micro-wrinkling and/or pre-micro-buckling may lead to the damage of stretchable organic solar cells. Similarly, excessive stretching, following the onset of micro-buckling and/or micro-winkling, may also result in the degradation of optical transmittance and device current-voltage characteristics.

Since the onset of interfacial cracking can affect the pe-wrinkling/buckling and the subsequent conditions for the degradation of stretchable organic solar cells, a significant effort is needed to control the processing environments and cleaning processes that may give rise to interfacial impurities at the interfaces between the multiple layers in stretchable organic solar

cells. This is particularly true for the least adherent layers, such as those between PDMS and PEDOT;PSS.

A balanced approach is needed for the design of stretchable organic solar cells. This involves: the use of pre-buckled/pre-stretched organic solar cells on stretchable substrates; the control of interfacial impurities and adhesion energies; an understanding of the possible failure modes that can occur due to the applications of stresses and deformations to pre-buckled or pre-wrinkled structures, and a knowledge of how the induced failure modes affect the optical and electrical current-voltage characteristics of organic solar cells.

Table 6.1: Properties of the materials used in the modeling

Material	**Young's Modulus (GPa)**	**Poisson Ratio**	**References**
P3HT:PCBM	6.02	0.35	[27]
PEDOT:PSS	1.56	0.3	[28]
ITO	116	0.35	[29]
PDMS	0.003	0.3	[29]

6.6 References

[1] D. J. Lipomi, J. A. Lee, M. Vosgueritchian, B. C.-K. Tee, J. A. Bolander, and Z. Bao, "Electronic properties of transparent conductive films of PEDOT: PSS on stretchable substrates," *Chem. Mater*. 24, 373-382 (2012).

[2] D. J. Lipomi, B. C. Tee, M. Vosgueritchian and Z. Bao, "Stretchable Organic Solar Cells," *Adv. Mater*. 23, 1771-1775 (2011).

[3] Y. H. Zhang, S. Xu, H. Fu, J. Lee, J. Su, K.-C. Hwang, J. A. Rogers and Y. Huang, "Buckling in serpentine microstructures and applications in ultra-stretcgable electronics with high areal coverage," Soft Matter. 9, 8062-8070 (2013).

[4] J. Weiss, P. Kukuri, J. Chiguma, J. Gendon, B. Arfaei, P. Borgesen, and W. Jones, Fabrication of low cost flexible solar using solution-based coating techniques, Global Solar Technology 10-15 (2011).

[5] G. Dennler, C. Lungenschimied, H. Neugebauer, and N. S. Sariciftci, "Flexible, conjugated polymer-fullerene-based bulk-heterojunction solar cells: Basics, encapsulation, and integration," J. Matter. Res., 20, 3224-3233 (2005).

[15] J. Lee, M. Shi, J. Yoon, S-I. Park, M. Li, Z. Liu and Y. Rogers, "Stretchable GaAs Photovoltaic with Design that Enable High Areal Coverage," *Adv. Mater*. 23, 986-991, (2011)

[6] Y. Sun and J. Rogers, "Inorganic semiconductors for flexible electronics," Adv. Mater.19, 1897-1916 (2007).

[7] Y. Su, Z. Liu, S. Kim, J. Wu, Y. Huang, J. A. Rogers, "Mechanics of stretchable

electronics with high Fill Factor," International Journal of Solids and Structures 49, 3416-3421 (2012).

[8] T. Sekitani, Y. Noguchi, K. Hata, T. Fukushima, T. Aida, T. Someya, Science 321, 1468-1472 (2008).

[9] D-H. Kim, J. Xiao, J. Song, Y. Huang and J. A. Rogers, "Stretchable, Curvilinear Electronics Based on Inorganic Materials," *Adv. Mater.* 22, 2108-2124 (2010).

[10] H. Mei and R. Huang, Proceedings of the 13th International Conference on Fracture, Beijing, China, 1-9 (2013).

[11] M. Watanabe, "Wrinkles with a well-ordered checkerboard pattern, created using dip-coating," *Soft Matter* 8, 1563-1569 (2012).

[12] D.-Y. Khang, J. A. Rogers, and H. H. Lee, "Mechanical buckling: mechanics, metrology, and stretchable electronics," Adv. Funct. Mater. 18, 1-11 (2008).

[13] T. Li, Z. Suo, S. P. Lacour and S. Wagner, "Compliant Thin Film Patterns of Stiff Materials as Platforms for Stretchable Electronics," *J. Meter. Res.* 20(12), 3274-3277 (2005).

[14] D-H. Kim, and J. A. Rogers, "Stretchable Electronics: Materials Strategies and Devices," *Adv. Mater.* 20, 4887-4892 (2008).

[15] S. P. Lacour, J. Jones, Z, Suo and S. Wagner, "Design and Performance of Thin Metal Film Interconnects for Skin-Like Electronic Circuits," *IEEE Electron Device Lett.* 25, 179-181 (2004).

[16] C. Yu, K. O'Brien, Y.-H. Zhang, H. Yu and H. Jiang, "Tunable Optical Grating Based on Buckled Nano-Scale Thin Films on Transparent Elastomeric Substrates," *Appl. Phys.*

Lett. 96, 041111 (2010).

[17] N. Bowden, W. T. S. Huck, K. E. Paul and G. M. Whitesides, **"**The Controlled formation of ordered, sinusoidal structures by plasma oxidation of an elastomeric polymer," *Appl. Phys. Lett.* 75, 2557-2559 (1999).

[18] C. M. Stafford, C. Harrison, K. L. Beers, A. Karim, E. J. Amis, M. R. VanLandingham, H.-C. Kim, W. Volksen, R. D. Miller, E. E. Simonyi, "A buckling-based metrology for measuring the elastic moduli of polymeric thin films," *Nat. Mater*. **3**, 545-550 (2004).

[19] C. M. Stafford, B. D. Vogt, C. Harrison, D. Julthongpiput and R. Huang, "Elastic moduli of ultrathin amorphous polymer films," *Macromolecules*, 39, 5095-5099 (2006).

[20] P. J. Yoo, K. Y. Suh, S. Y. Park and H. H. Lee, "Physical self-assembly of microstructures by anisotropic buckling," Adv. Mater. **14**, 1383 (2002).

[21] Watanabe, H. Shirai and T. Hirai, "Wrinkled polypyrrole electrode for electroactive polymer actuators," *J. Appl. Phys.* 92, 4631-4637 (2002).

[22] Z. Jia, M. B. Tukker, T. Hi, "Failure mechanics of organic–inorganic multilayer permeation barriers in flexible electronics," Composites Science and Technology **71,** 365-372 (2011).

[23] T. Tong, B. Babatope, S. Admassie, J. Meng, O. Akwogu, W. Akande and W. O. Soboyejo, "Adhesion in organic structures," *J. Appl. Phys.* **106**, 083708 (2009).

[24] D. Yu, O. K. Oyewole, D. Kwabi, T. Tong, V. C. Anye, J. Asare, E. Rwenyagila, A. Fashina, O. Akogwu, J. Du, and W. O. Soboyejo, "Adhesion in flexible organic and hybrid organic/inorganic light emitting device and solar cells" *J. Appl. Phys.* 116, 074506 (2014).

[25] T. Sekitani, H. Nakajima, H. Maeda, T. Fukushima, T. Aida, K. Hata and T. Someya, "Stretchable active-matrix organic light-emitting diode display using printable elastic conductors," *Nature materials 8*, 494-499 (2009).

[26] J. A. Rogers, T. Someya, Y. Huang, "Materials and mechanics for stretchable electronics," Science 327, 1603-1607 (2010).

[27] J. Du, T. Tong, W. Akande, A. Tsakiridou, and W. Soboyejo, "Pressure Effects on the Lamination of Organic Light Emitting Devices," *J. Disp. Technol.* 9, 601–606 (2013).

[28] O. Akogwu, D. Kwabi, S. Midturi, M. Eleruja, B. Babatope and W. O. Soboyejo, "Large strain deformation and cracking of nano-scale gold films on PDMS substrates," *Mater. Sci. Eng. B* 170, 32-40 (2010).

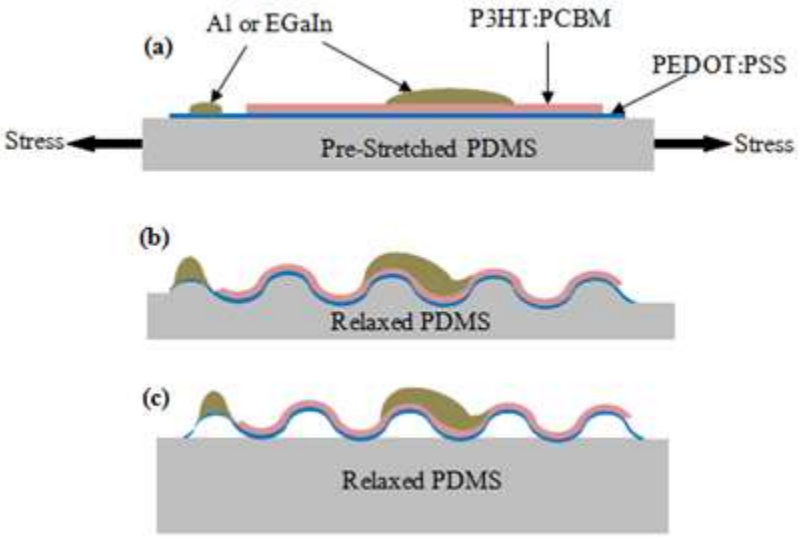

Figure 6.1: Schematics of buckling and wrinkling in stretchable organic solar cells

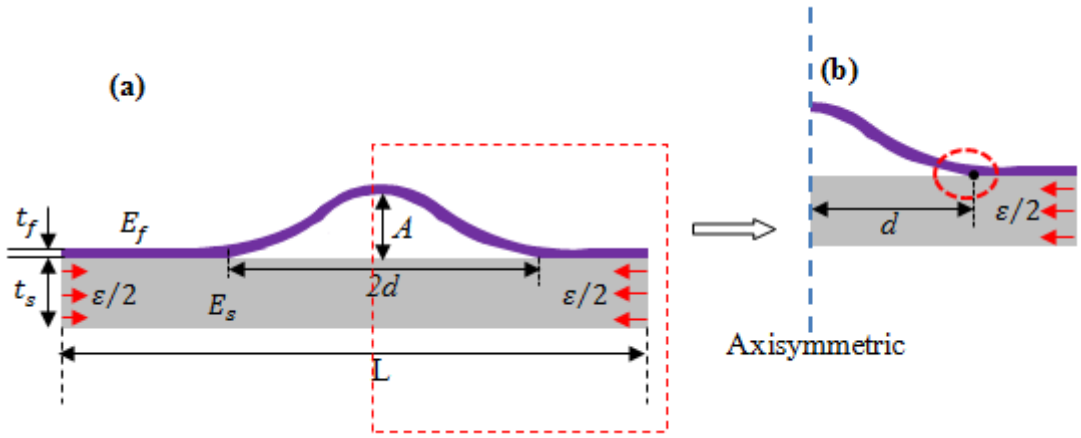

Figure 6.2: Schematic model of buckled thin films

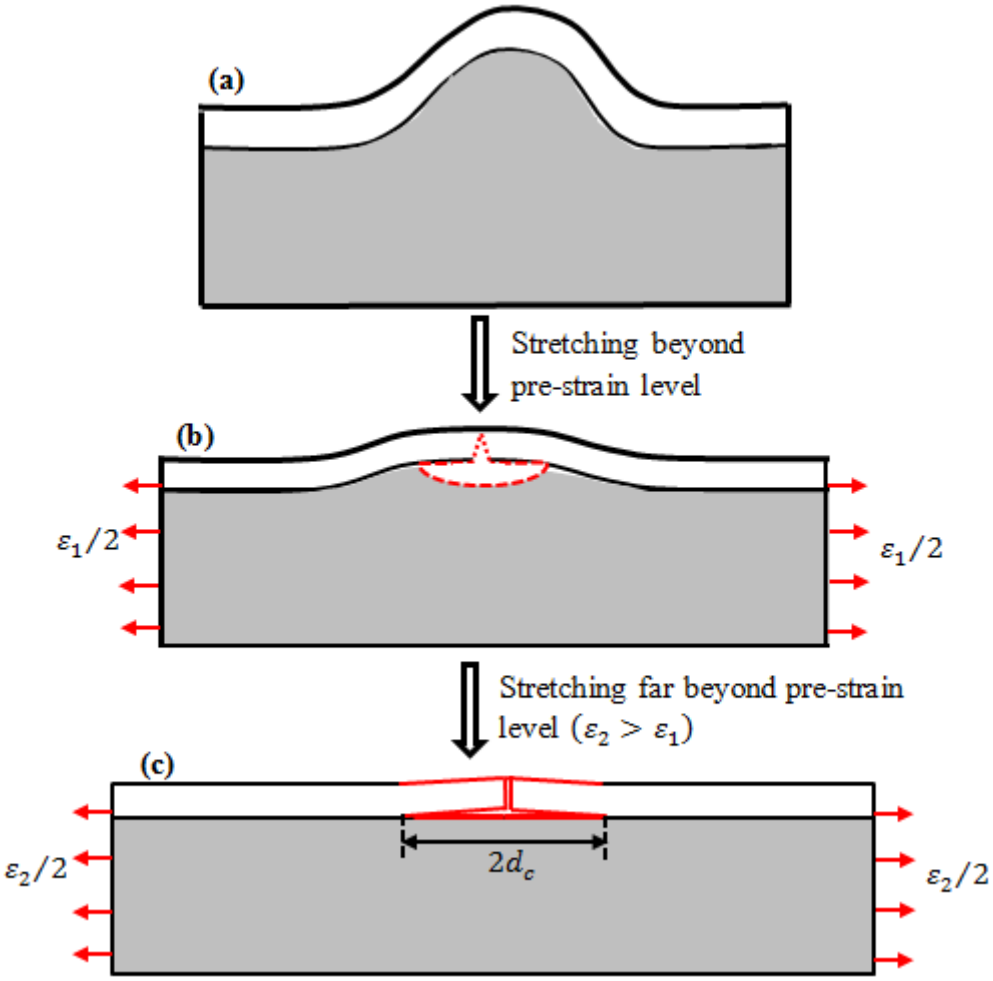

Figure 6.3: Schematic of failure mechanisms in wrinkled thin films: (a) unstretched wrinkled film (b) nucleation of interfacial cracking of thin films when stretched beyond pre-strain level (c) crack-induced delamination of the film from substrate when stretched far beyond pre-strain level.

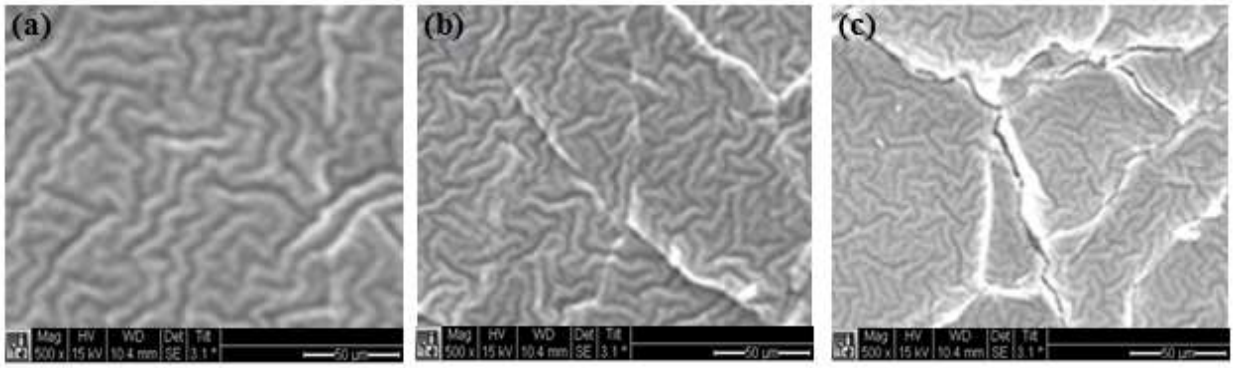

Figure 6.4: SEM images of failures mechanisms in PEDOT:PSS/PDMS structure (a) unstretched (b) stretched up to 25 % strain (c) stretched up to 70 % strain

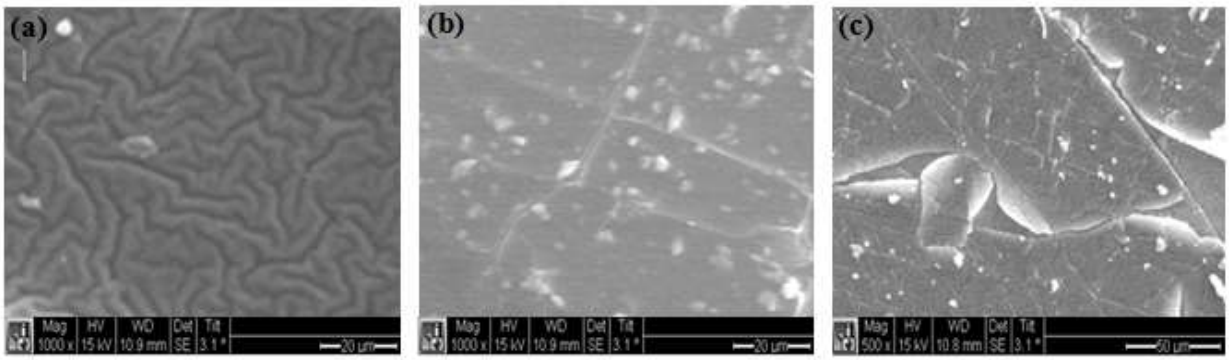

Figure 6.5: SEM images of failures mechanisms in P3HT:PCBM on PEDOT:PSS-coated PDMS (a) unstretched (b) stretched up to 25 % strain (c) stretched up to 70 % strain

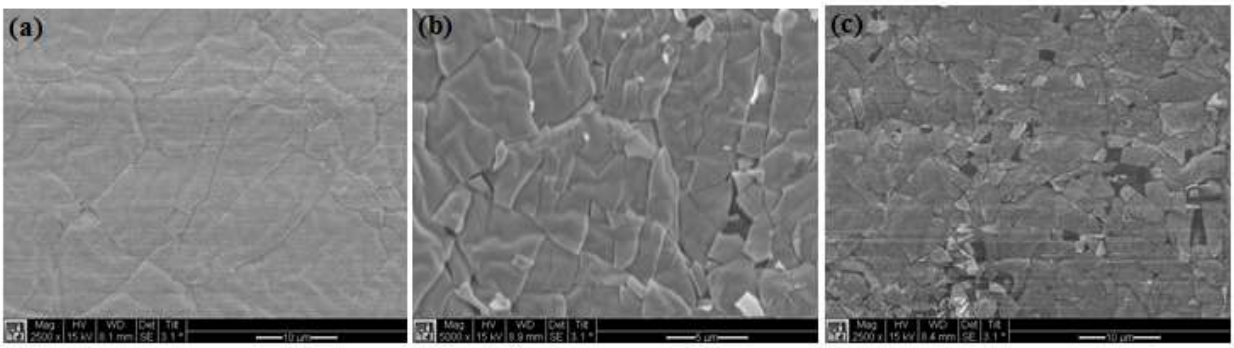

Figure 6.6: SEM images of failures mechanisms in ITO/PDMS structure (a) unstretched (b) stretched up to 10 % strain (c) stretched up to 30 % strain

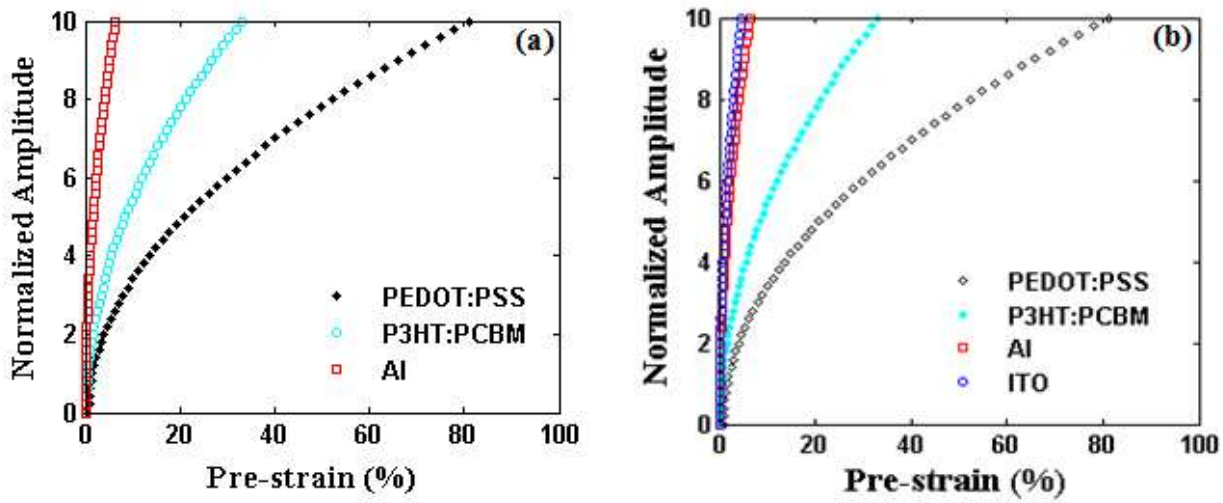

Figure 6.7: Amplitude of wrinkled films versus pre-strain for solar cell (a) without ITO layer (b) with ITO layer

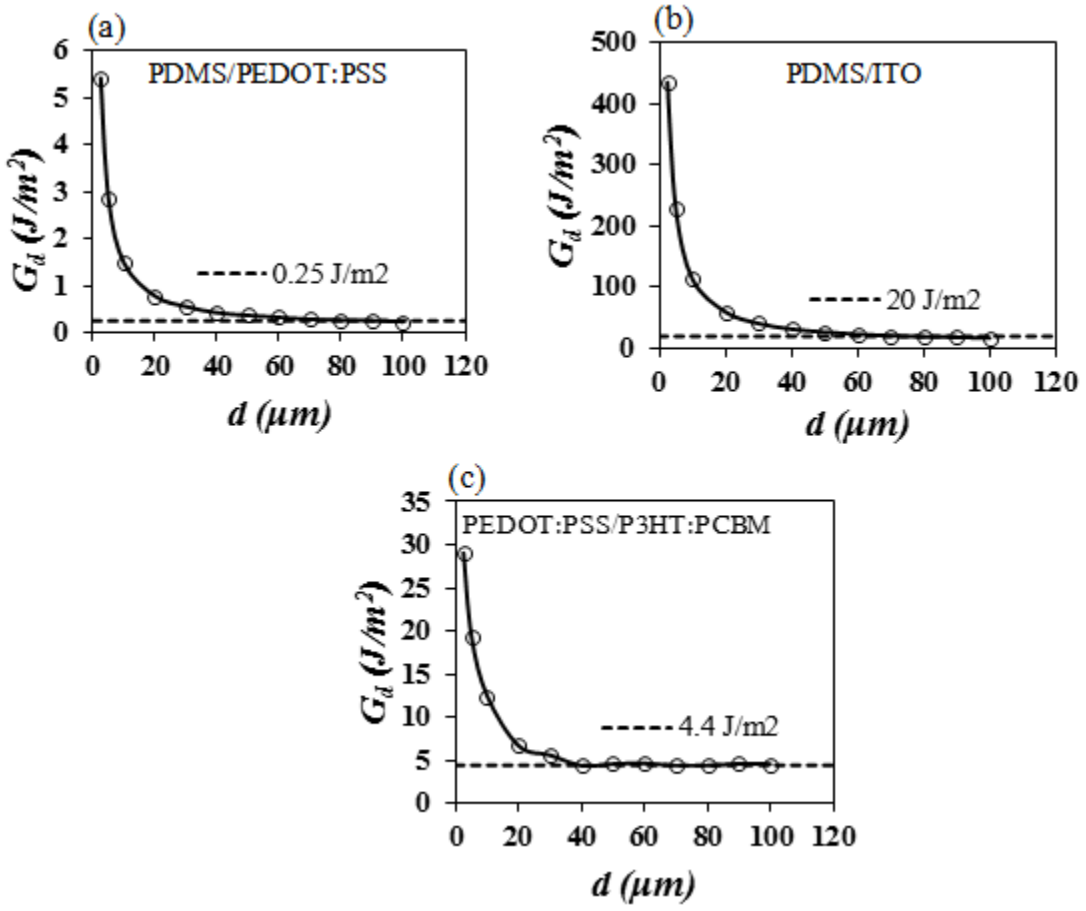

Figure 6.8: Interfacial energy rate versus interfacial crack length along (a) PDMS and PEDOT:PSS interface (b) PDMS and ITO interface (c) PEDOT:PSS and P3HT:PCBM interface. The dash lines indicate the steady-state energy levels for calculating interfacial fracture energies.

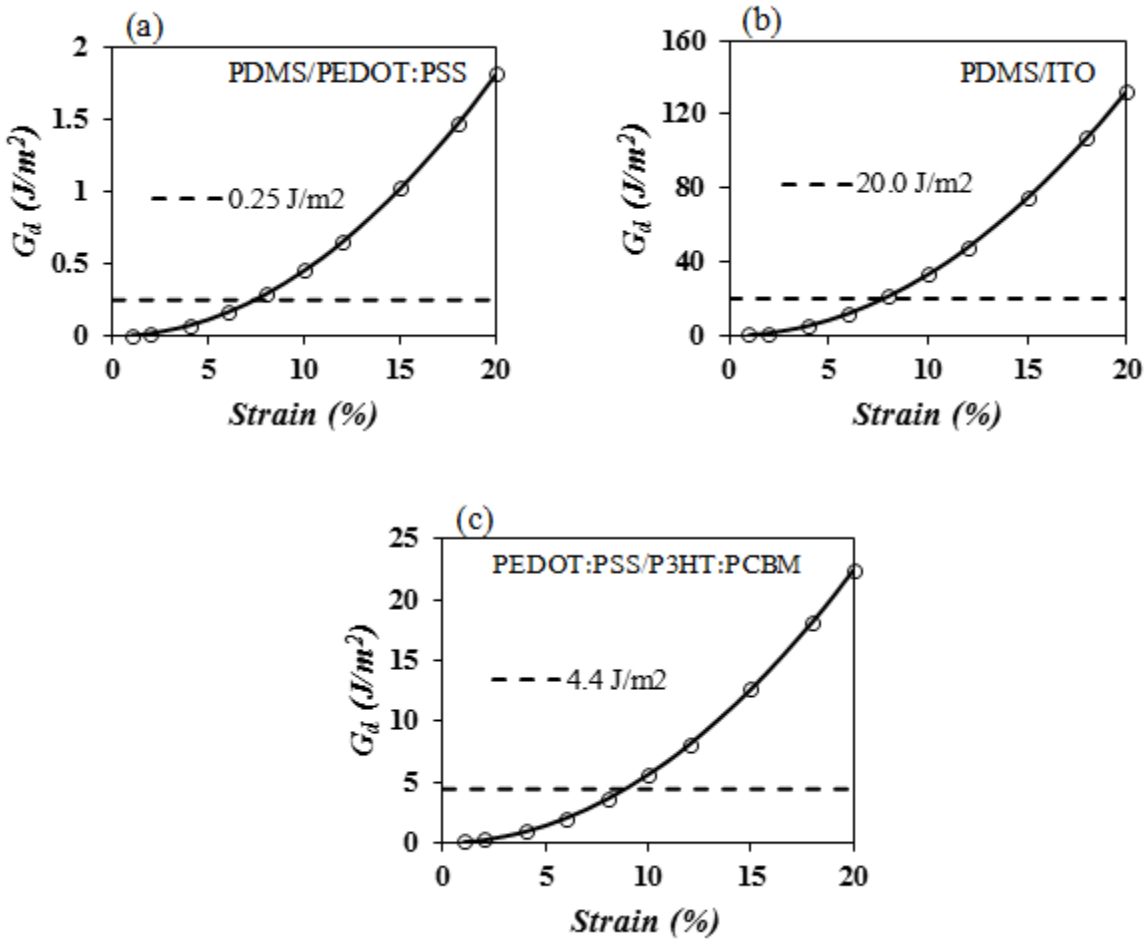

Figure 6.9: Energy release rate versus applied strain for interface between (a) PDMS and PEDOT:PSS; (b) PDMS and ITO, and PEDOT:PSS and P3HT:PCBM. The dash lines are the critical compute interfacial fracture energies

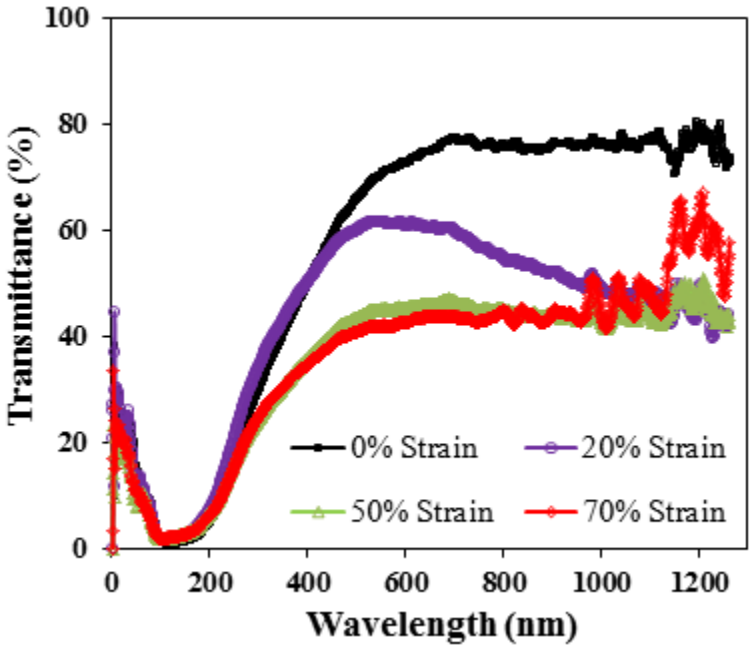

Figure 6.10: Degradation of optical transmittance spectra of anodic PEDOT:PSS on PDMS substrate

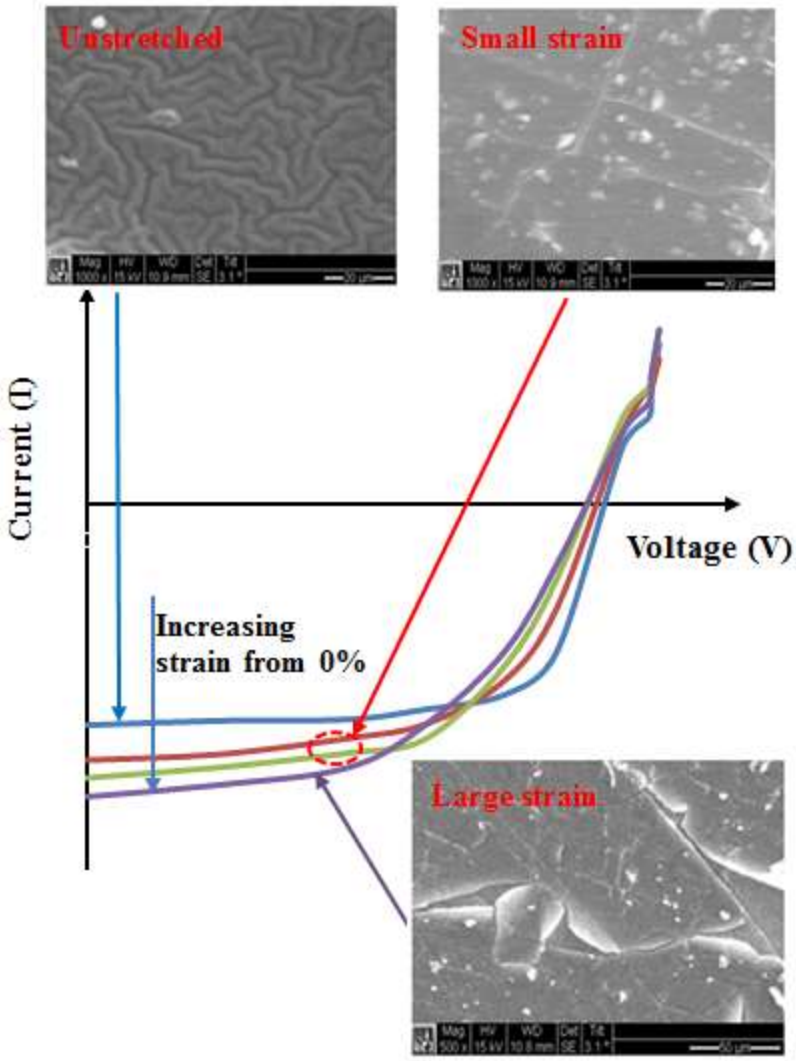

Figure 6.11: Illustration of effects of failure mechanisms on typical I-V curves of a stretchable organic solar cell for different applied strain level.

CHAPTER 7

CONCLUSIONS AND SUGGESTIONS FOR FUTURE WORK

7.1 Conclusions

This Thesis has presented a combined experimental, computational and analytical approach to study adhesion and deformation in multilayered stretchable electronic structures. The key issues discussed in this Thesis include: adhesion in organic, inorganic and hybrid organic-inorganic stretchable/flexible light emitting diodes and solar cells; micro-wrinkling and delamination-induced buckling of stretchable organic structures; effects of stretching on failure mechanisms of stretchable organic solar cells, and lamination of organic solar cells and organic light emitting devices. The results and salient conclusions of each of the key issues are summarized below:

1. The adhesion in organic, inorganic and hybrid organic/inorganic stretchable/flexible solar cells and light emitting devices were measured using atomic force microcopy. In the case of hybrid organic/inorganic light emitting devices, MEH-PPV was replaced by MEH-PPV:TiO_2 mixtures. The MEH-PPV:TiO_2 active layers had higher adhesion energies with

adjacent layers (PEDOT:PSS and Al) compared to MEH:PPV. For hybrid organic/inorganic solar cells, P3HT:PCBM layer was replaced with P3HT:PCBM:TiO_2 mixture. The P3HT:PCBM layer adhered better to adjacent PEDOT:PSS and Al layers when compared with the P3HT:PCBM:TiO_2. The reduction in the adhesion of P3HT:PCBM:TiO_2 with adjacent layers is due to potential effects of electrochemical reactions that are associated with the introduction of TiO_2. Therefore, the improvements in the charge transport facilitated by TiO_2 must be balanced against potential reductions in the adhesion.

2. The failure mechanisms associated with inorganic electronic structures were also explored. Micro-wrinkling and delamination-induced buckled formation in thin films of nano-scaled gold coated onto the surface of stretchable polymeric PDMS substrates. The measurements of interfacial fracture toughness obtained for Au films on PDMS substrates are comparable to the AFM measured adhesion energy. The pre-strain limits were predicted using the critical measured adhesion energies.
3. The deposition of organic electronic structures was explored using a simple and cheap lamination technique. The technique was elucidated at macro and micro scale using a combination of experimental and computational method. The effects of pressure on the contacts of layered OLED and OPV cell structures were studied, showing an increase contact ratios with increasing pressure. However, the application of pressure can result to excessive sink-in of trapped particles, which can damage the devices. The interfacial fracture process was studied using computational models of interfacial crack driving forces. The models suggest that fracture occurred when the crack driving forces were

equal to the measured interfacial adhesion energies of relevant interfaces of OLED and OPV cell structures.

4. Finally, the effects of deformation on failure mechanisms and optical property of stretchable organic solar cells were then explored. The optical transmittance spectra of anodic layer of stretchable organic solar cells were measured as function of strain. The transmittance reduces with increasing strain. The energy release rates associated with stretching of relevant layers of the devices were also elucidated using finite element/computational models. The failure modes (interfacial cracking and wrinkling) associated to stretching were observed using SEM. The failure modes were shown to be responsible for changes in the transmittance of the anodic electrode, which spontaneously degrade the stretchable organic solar cells.

7.2 Suggestions for Future Work

7.2.1 Adhesion in Stretchable/Flexible Organic and Hybrid Organic/Inorganic Light Emitting Devices and Solar Cells

The work on adhesion in stretchable/flexible organic and hybrid organic/inorganic light emitting devices and solar cells can be extended by creating a balance between interfacial adhesion and charge transport in TiO_2 based stretchable organic solar cells. The performance of the future stretchable organic electronic devices can be enhanced by dispersing other nanoparticles existing active layer (P3HT:PCBM) for improved charge transport and adhesion between the adjacent layers.

7.2.2 Micro-Wrinkling and Delamination-Induced Buckling of Stretchable Electronic Structures

Further work is suggested for different inorganic electronic devices for biomedical applications. These devices (such as implantable devices) undergo deformation in the domain where they are being applied. Therefore, the evidence of wrinkling and buckling failure modes due to temperature effects and cyclic loading should be characterized for different configurations of the devices. The temperature effects on failure mechanisms of integrated circuit systems should be fully characterized.

7.2.3 Lamination of Organic Solar Cells and Organic Light Emitting Devices

The lamination of stretchable organic solar cells and light emitting devices can be fine-tuned further by studying the kinking in-and-out of cracks from different interfaces. The kinking in and out can contribute to partial separation that is observed during pull-off. Therefore, clear understanding of the mechanisms involved in the kinking of interfacial crack will help to predict the conditions for successful lamination low-cost organic solar cells and organic light emitting devices.

7.2.4 Effects of Stretching on Failure Mechanisms of Stretchable Organic Solar Cells

It is suggested that the fabrication and characterization of stretchable organic solar cells carried out in greater detail for different failure mechanisms in a clean environment. The effects of stretching should also be considered for the devices fabricated at different pre-strained

substrates. By doing so, the critical pre-strain can be ascertained, which can be compared to the predictions obtained from computational modeling.

APPENDIX

A Interfacial Energy Release Rate Due to Lamination of Thin Films

$G = f(\overline{E}_s, \overline{E}_f, t_f, t_s, d_b, d_t, \sigma)$

Number of parameters = 8

Number of fundamental dimension = 3

Number of dimensionless quantities = 8-3 = 5

The core variables are:

$\sigma = [ML^{-1}T^{-2}]$, $\overline{E}_f = [ML^{-1}T^{-2}]$ and $t_f = [L]$

$$\sigma^2 t_f^2 = [M^2L^{-2}T^{-4}][L^2] = [M^2T^{-4}] \tag{A.1}$$

$$\overline{E}_f t_f = [ML^{-1}T^{-2}][L] = [MT^{-2}] \tag{A.2}$$

By dividing Equation (B.1) by (B.2)

$$\frac{\sigma^2 t_f^2}{\overline{E}_f t_f} = \frac{\sigma^2 t_f}{\overline{E}_f} = \frac{[M^2T^{-4}]}{[MT^{-2}]} = [MT^{-2}] \tag{A.3}$$

First dimensionless quantity (π_1):

$$G = [MT^{-2}] = \frac{\sigma^2 t_f}{\overline{E}_f}$$

$$\pi_1 = \frac{G\overline{E}_f}{\sigma^2 t_f}$$

Second dimensionless quantity (π_2):

$$\overline{E}_f = \left[ML^{-1}T^{-2}\right]$$

$$\pi_2 = \overline{E}_s\left[LT^2M^{-1}\right] = \frac{\overline{E}_s}{\overline{E}_f}$$

Third dimensionless quantity (π_3):

$$t_s = \left[L\right]$$

$$\pi_3 = t_s\left[L^{-1}\right] = \frac{t_s}{t_f}$$

Fourth dimensional quantity (π_4):

$$d_b = \left[L\right]$$

$$\pi_4 = d_b\left[L^{-1}\right] = \frac{d_b}{t_f}$$

Fifth dimensional quantity (π_5)

$$d_t = \left[L\right]$$

$$\pi_5 = d_t\left[L^{-1}\right] = \frac{d_t}{t_f}$$

$$\pi_1 = f\left(\pi_2, \pi_3, \pi_4, \pi_5\right)$$

$$\frac{G\overline{E}_f}{\sigma^2 t_f} = f\left(\frac{\overline{E}_s}{\overline{E}_f}, \frac{t_s}{t_f}, \frac{d_b}{t_f}, \frac{d_t}{t_f}\right)$$

$$G = f\left(\frac{\overline{E}_s}{\overline{E}_f}, \frac{t_s}{t_f}, \frac{d_b}{t_f}, \frac{d_t}{t_f}\right)\frac{\sigma^2 t_f}{\overline{E}_f} \tag{A.4}$$

B Energy Release Rates Due to Delamination of Thin Films

$$G_d = f\left(d, \overline{E}_f, \overline{E}_s, t_f, t_s, \varepsilon\right)$$

Number of parameters = 6

Number of fundamental dimension = 3

Number of dimensionless quantities = 7-3 = 4

The core variables are:

$\overline{E}_f = \left[ML^{-1}T^{-2}\right]$, $\varepsilon = [\ ]$ and $t_f = [L]$

$$\varepsilon^2 t_f^2 = \left[L^2\right] \tag{B.1}$$

$$\overline{E}_f \varepsilon^2 t_f = \left[ML^{-1}T^{-2}\right][L] = \left[MT^{-2}\right] \tag{B.2}$$

First dimensionless quantity (π_1):

$$G_d = \left[MT^{-2}\right] = \overline{E}_f \varepsilon^2 t_f$$

$$\pi_1 = \frac{G_d}{\overline{E}_f \varepsilon^2 t_f}$$

Second dimensionless quantity (π_2):

$$\overline{E}_s = \left[ML^{-1}T^{-2}\right]$$

$$\pi_2 = \overline{E}_s\left[LT^2M^{-1}\right] = \frac{\overline{E}_s}{\overline{E}_f}$$

Third dimensionless quantity (π_3):

$$t_s = \left[L\right]$$

$$\pi_3 = t_s\left[L^{-1}\right] = \frac{t_s}{t_f}$$

Fourth dimensional quantity (π_4):

$$d = \left[L\right]$$

$$\pi_4 = d\left[L^{-1}\right] = \frac{d}{t_f}$$

$$\pi_1 = f\left(\pi_2, \pi_3, \pi_4\right)$$

$$\frac{G_d}{\overline{E}_f \varepsilon^2 t_f} = f\left(\frac{\overline{E}_s}{\overline{E}_f}, \frac{t_s}{t_f}, \frac{d}{t_f}\right)$$

$$G_d = f\left(\frac{\overline{E}_s}{\overline{E}_f}, \frac{t_s}{t_f}, \frac{d}{t_f}\right)\overline{E}_f \varepsilon^2 t_f \qquad \text{(B.4)}$$